NAGOYA UNIVERSITY

DOCTORAL THESIS

Neutral Hydrogen 21-cm Signature Originated from the First Generation of Stars in the Universe

Toshiyuki TANAKA

Division of Particle and Astrophysical Science
Graduate School of Science

A thesis submitted in fulfillment of the requirements
for the degree of Doctor of Philosophy

January 11, 2021

Abstract

At the end of the cosmic dark ages, the first generation of stars (the first stars) form in the Universe, telling the begging of the epoch of reionization (EoR). The population III stars (pop III stars), which means stars formed from pristine metal-free gas and the first stars are included in Pop III stars, play key roles in the thermal history and the history of the structure formation. For example, the ionizing photons emitted from pop III stars ionize the inter-galactic medium (IGM) contributing more or less to the reionization, and the heavy elements ejected at the end of stellar lifetime enhance the formation of subsequent generation of stars. To what extent Pop III stars affect the cosmic history strongly depends on the stellar properties such as star formation rate density (SFRD) and initial mass function (IMF).

Since the clear detection of pop III stars has not reported, the theoretical researches have proceed our understanding of pop III stars' properties. However, the results of theoretical works have not converged yet. Recently neutral hydrogen 21-cm line emission is getting more and more attention because the 21-cm signal carries information on gas at high-z Universe including Pop III stars. Thus, constructing theoretical models which connects the 21-cm observable with the properties of pop III stars is necessary to extract information on Pop III stars from current and future observations.

We investigate the 21-cm signals at the both small and large scales. As for the small scale, we develop spherically-symmetric one-dimensional radiation hydrodynamics (RHD) simulations and study the profile of the 21-cm brightness temperature around individual pop III star. What we find is that the gas dynamics plays an essential role: In early phase, the ionized region is well confined in the halo so that the deep absorption region is seen around the central star, then in late phase, the ionized region expands beyond the halo radius letting the absorption signal weaker. Also we revel the stellar mass, halo mass and redshift dependences of the 21-cm profile.

In regards to the large scale, we develop and conduct the cosmological 21-cm semi-numerical simulations which for the first time incorporate both UV photoheating and time-evolving escape fraction which reflects increasing minimum halo mass for star formation due to the Lyman-Werner (LW) negative feedback. We find that if Pop III stars do not contribute the cosmic reionization, the 21-cm signals do not carry information on Pop III stellar mass although the 21-cm global signal provides us with the information on SFRD. On the other hand, when Pop III stars contribute the reionization, the 21-cm global signal and the power spectrum reflect both the typical stellar mass and SFRD.

Contents

List of Figures

List of Tables

Chapter 1

General Introduction

The Universe was born as high-density fireball with high temperature about 13.8 billion years ago. Since then, the Universe has been expanding so that the temperature and density are decreasing. When the age of the Universe was about 380 thousand years old, the photons decoupled from baryon, so-called recombination, and started propagating straight toward us. The radiation from the last scattering surface is observed as the cosmic microwave background (CMB). The historical observation by the COBE satellite has found the tiny fluctuation on the CMB. This inhomogeneity at the early Universe is indeed the seed of all the structure in the Universe. The gravity has the essential nature for the structure formation which grows the seed: a place in which there are a little bit more matter has stronger gravitational force attracting more surrounding matter, so that the place has even stronger gravity. As a result, the initial tiny fluctuation increases and finally yields the rich variety of structures seen in the Universe as of today. After the COBE observation, the CMB has been observed more precisely by the subsequent satellites of the WMAP and the Planck and we now know the initial temperature fluctuates is in order of $\sim 10^{-5}$ in fraction.

The epoch after recombination is called the dark ages because there are no luminous objects, however, the tiny initial density fluctuation grows in the dark Universe. Resultantly, around when the cosmic age is about 200 million years old, the first generation of stars (the first stars) are born. The first stars are expected to be fairly different from most stars observed today like the Sun. In the star formation process, the gas cooling is necessary for gas cloud to contract until the density becomes high enough to begin the nuclear reaction. The dominant coolant in the case of stars formed in late-time Universe is heavy elements, which is also called metal oftentimes, however on the other hand, the first stars are formed from the primordial gas whose chemical composition is determined by the Big Bang nucleosynthesis, that is, there are no elements heavier than the lithium. The main coolant in this case is the molecular hydrogen whose cooling efficiency is relatively low. Therefore, stars made of the zero-metal primordial gas (so called the population III stars) are expected to be more massive.

The first stars play an important role regarding to the cosmic ionization status.

After the cosmic recombination drastically changes the ionization status of the Universe from being almost fully ionized to being almost neutral, the Universe remains neutral throughout the dark ages. The ionizing photons emitted from the first stars start re-ionizing the Universe for the first time since recombination. The period from when the first stars begins ionizing the Universe (cosmic age of $\sim$ 200 million years) to when the Universe is again completely ionized ($\sim$ 900 million years) is called the epoch of reionization (EoR). The pop III stars must more or less contribute to the reionization.

In additional to the reionization, the pop III stars have other key roles in the history of the Universe. Since the pop III stars are expected to be massive, they would end up their lives as energetic supernova (SN), providing metals created inside stars into the surrounding regions. The metal enhances the formation of the subsequent generation of stars by letting gas cooling efficient. Moreover, the black hole left after SN is one of the candidates for seeds of extremely massive black hole found at the center of galaxies.

The pop III stars have essential roles in the thermal history and the structure formation as described just above. How large impact the pop III stars have strongly depends on the stellar properties such as the star formation rate density (SFRD) and the initial mass function (IMF). For example, the emissivity of ionizing photons from pop III stars depends on SFRD and whether the pop III stars leave back holes is determined by their stellar mass. Therefore, understanding pop III stars is the key to achieve the goal of cosmology and astronomy, which is to reveal the whole history of the Universe and phenomena in the Universe.

Since the clear evidence of pop III stars has not yet obtained by observations, the theoretical researches mainly progress our understanding of pop III stars' properties. Especially in the past decade, our knowledge of SFRD and IMF have been deepened due to the recent developments of the computer technology and the numerical algorithms. However, the results of the researches have not reached consensus yet. Therefore, not only the bottom-up approach by theoretical studies but also the top-down approach by observations are highly demanded in order to further understand the properties of the pop III stars.

As for observations, the 21-cm line emission is recently attracting more and more attention. The 21-cm radiation is emitted from the hyperfine structure of neutral hydrogen. Since there would be abundant HI at the era when pop III star formation is dominant, the 21-cm observations should be advantageous way to investigate the pop III stars. Moreover, we can investigate each redshift tomographically by choosing observation frequency because the 21-cm emission is a line emission. Recent technological developments related with observations are about to enable us to detect 21-cm signals from the high-redshift Universe. Currently, several observations

are running, for instance, the Murchison Widefield Array (MWA) and The Experiment to Detect the Global EoR Signature (EDGES). Also the huge radio telescope, the Square Kilometre Array (SKA), is about to start its observations.

In order to extract fruitful information on the pop III stars from forthcoming observational results, the theoretical models which connect the 21-cm observables with properties of pop III stars are absolutely indispensable. However, models able to distinguish typical stellar mass and SFRD of pop III stars have not established yet. Thus, constructing such theoretical model is the urgent issue.

I, throughout my PhD course, have been addressing the issue by investigating how the SFRD and the typical stellar mass of pop III stars influence the 21-cm signature in both small scale and large scale. As for the small scale, I with collaborators studies the profile of the 21-cm brightness temperature around individual pop III star with the one-dimensional spherically-symmetric radiation hydrodynamics simulations (RHD simulations). We for the first time consider the dense gas in halo and study how the hydrodynamic feedback affects the 21-cm profile around a pop III star. Regarding to the large scale, we develop and conduct the cosmological 21-cm semi-numerical simulation considering the UV photo-heating and time-changing escape fraction of ionizing photons. The UV photo-heating and escape fraction for time first time account for the stellar mass dependence being enabled by results of our RHD simulations. By analyzing the simulation results, we investigate whether we can distinguish the SFRD and the typical stellar mass of pop III stars.

This thesis is organized as follows: In Chapter 2, I describe the standard cosmological model, which is the background environment for structure formation, and the observational status quo. I explain structure formation in Chapter 3; the linear perturbation theory, approximation methods for non-linear regime, and the star formation at high-redshift Universe. The Chapter 4 is dedicated to explain the 21-cm basics and the current status of observations. I describe my studies about the 21-cm signature around pop III stars in Chapter 5, and about the cosmological 21-cm signal in Chapter 6. Finally, I summarize and conclude my works in Chapter 7.

Throughout this thesis, We work on a flat ΛCDM cosmology with the cosmological parameters with the matte density, $\Omega_{\rm m0} = 0.308$, the baryon density, $\Omega_{\rm b0} = 0.0485$, the Hubble constant, $h_0 = 0.678$, the index of initial matter power spectrum, $n_{\rm s} = 0.968$, the rms mass fluctuation on 8 Mpc$/h$ scales at present day, $\sigma_8 = 0.828$, the mass fraction of Helium, $Y_{\rm He} = 0.249$ (Planck Collaboration XIII 2016).

Chapter 2

Standard cosmological model

In this chapter, I briefly introduce the theoretical background of the modern cosmology. The cosmology basically determines the dynamical evolution of the Universe itself, which fundamentally provides the background environment for the structure formation in the Universe.

What I firstly explain is the Friedmann equation which is the basic equation to describe dynamical evolution of the Universe. Then, I introduce the cosmological parameters, which are the parameters needed to solve the Friedmann equation, and some cosmological models. Finally, the observational constraints on the cosmological parameters are briefly introduced.

2.1 Friedmann equation

In this section, I concisely describe the flow to derive the Friedmann equation from the Einstein equation combined with the Friedmann-Lemaître-Robertson-Walker metric (FLRW metric).

The modern cosmology is based on the general theory of relativity in which the time and space is no longer independent variables. The spacetime and the component (matter and energy) of the Universe evolve while interacting each other. The co-evolution of spacetime and component is governed by the Einstein equation:

$$G^{\mu}_{\nu} = \frac{8\pi G}{c^4} T^{\mu}_{\nu}, \tag{2.1}$$

where G^{μ}_{ν} is the Einstein tensor, T^{μ}_{ν} is the stress-energy tensor, c is the speed of light, and G is gravitational constant. Under the cosmological principle, which is the fundamental assumption of the cosmology under which the Universe is uniform and isotropic on large scale, the stress-energy tensor is known to be given as

$$T^0_0 = -\rho,\ T^i_0 = T^0_i = 0,\ T^i_j = p, \tag{2.2}$$

where ρ and p are energy density and pressure.

The Einstein equation is general form in terms of metric, so that we need to give the metric of the Universe. The cosmological principle provides the FLRW metric in the spherical coordinate (r, θ, ϕ):

$$ds^2 = -c^2dt^2 + a^2(t)\left[\frac{dr^2}{1-Kr^2} + r^2(d\theta^2 + \sin^2\theta d\phi^2)\right], \tag{2.3}$$

where a is scale factor, and K is curvature.

Applying the FLRW metric to the Einstein equation gives us the equations below:

$$\left(\frac{\dot{a}}{a}\right)^2 = \frac{8\pi G}{3c^2}\rho - \frac{c^2K}{a^2}, \tag{2.4}$$

$$\frac{\ddot{a}}{a} = -\frac{4\pi G}{3c^2}(\rho + 3p). \tag{2.5}$$

Combining the two equations above and deleting $\ddot{a}$ provides

$$\dot{\rho} + 3\frac{\dot{a}}{a}(\rho + p) = 0. \tag{2.6}$$

Equation (2.6) is obviously not independent, however, the equation has importance in the sense that it corresponds to the energy-momentum conservation. Equation (2.4) is especially called the Friedmann equation which is corresponding to the energy equation.

The general procedure to solve the time-evolution of the scale factor is as follows. As independent equations, we take the two equations (2.4) and (2.6). We can not solve the equations simply because the unknown variables are a, ρ, p which are more than the number of equations. In order to close the equation system, we need the equation of state for each matter and energy component of the Universe. Since the entropy of the whole Universe is conserved, the unknown thermodynamics variable is only one. Thus, the equation of state can be written in $p = p(\rho)$. Substitute the equation of state into the conservation equation (2.6) gives us the relation of energy density and scale factor that is $\rho = \rho(a)$. Then, by substituting the relation to the Friedmann equation (2.4), we finally obtain the time-evolution of the scale factor $a = a(t)$.

Through the procedure we need to solve the first-order time-differential equation twice. Therefore we need two integration constants as which the energy density and scale factor at present day $\rho_0 \equiv \rho(t_0)$ and $a_0 = a(t_0)$ are often assigned. In terms of the scale factor, the current value is normalized as unity by definition. On the other hand, the energy density at present depends on the energy components of the Universe. The ratio of each component is only determined by observations. I describe some parameters which is necessary to determine the ratio of cosmic components.

2.2 Cosmological parameters

We cannot solve the cosmic evolution only with the theoretical framework described in the previous section. We additionally need the cosmological parameters which are determined only by observations. In other words, cosmological parameters are essential to get the solution of the Friedmann equation (2.4). Thus, the curvature and the total energy density at present are the cosmological parameters. Because the total energy density is composed of energy components such as matter and the dark energy, the current value of each energy density is also cosmological parameters. By combining the parameters, we can indeed create any number of new cosmological parameters. But, I here in this section introduce often-used parameters.

Hubble constant

We define the Hubble parameter as,

$$H(t) \equiv \frac{\dot{a}(t)}{a(t)}. \tag{2.7}$$

The parameter describes the expansion rate of the Universe at arbitrary time t. The Hubble constant is defined as the current value of the Hubble parameter:

$$H_0 = \left.\frac{\dot{a}}{a}\right|_{t=t_0}. \tag{2.8}$$

The normalized Hubble constant h is also often used:

$$H_0 = 100h[\mathrm{km/s/Mpc}] = 3.24 \times 10^{-18} h[/\mathrm{s}]. \tag{2.9}$$

Critical energy density

The critical density is defined as the matter density which is enough to stop the expansion of the Universe but not to lead to re-collapse. The expression is given with equation (2.4) substituting $K = 0$,

$$\rho_{c0} = \frac{3c^2 H_0^2}{8\pi G}. \tag{2.10}$$

Apart from multiplied constants, the critical energy density is the paraphrase of the Hubble constant.

Density parameters

When the Universe consists of multiple energy components, the total energy density at present time can be written by,

$$\rho_0 = \sum_A \rho_{A0}, \tag{2.11}$$

where ρ_{A0} is the current energy density of component A. The density parameter is the current energy density normalized by the critical energy density and defined for each cosmic component. For the component A, the density parameter is defined by,

$$\Omega_{A0} \equiv \frac{\rho_{A0}}{\rho_{c0}} = \frac{8\pi G\rho_{A0}}{3c^2H_0^2}. \tag{2.12}$$

The density parameter for the total energy density is,

$$\Omega_0 \equiv \frac{\rho_0}{\rho_{c0}} = \sum_A \Omega_{A0}. \tag{2.13}$$

Under the assumption that the dark energy is given by the cosmological constant, the density parameter of the dark energy is,

$$\Omega_{\Lambda 0} = \frac{c^2\Lambda}{3H_0^2}. \tag{2.14}$$

At present Universe, the most energy consists of matter and dark energy components. Therefore, by neglecting the contribution from radiation components,

$$\Omega_0 \approx \Omega_{m0} + \Omega_{\Lambda 0}, \tag{2.15}$$

where Ω_{m0} is the density parameters of matter.

Curvature parameter

With the density parameters, the Friedmann equation (2.4) can be written as,

$$\Omega_0 - \frac{c^2K}{H_0^2} = 1. \tag{2.16}$$

The curvature itself has the dimension of [length^2]. We call dimensionless curvature the curvature parameter which is the second term in the left-hand side:

$$\Omega_{K0} \equiv -\frac{c^2K}{H_0^2}. \tag{2.17}$$

Then, equation (2.16) can be re-written as,

$$\Omega_0 + \Omega_{K0} = \sum_A \Omega_{A0} + \Omega_{K0} = 1. \tag{2.18}$$

The curvature parameter has a similar role as density parameters. The Universe is currently dominated by the matter and the dark energy components so that we can neglect the radiation component. As a result,

$$\Omega_{m0} + \Omega_{\Lambda 0} + \Omega_{K0} = 1, \tag{2.19}$$

is a good approximation.

2.3 Flat lambda model

There are several cosmological models depending on which component exists in the Universe. For example, the Einstein-de Sitter model assumes that curvature and dark energy are negligible ($\Omega_{K0} = \Omega_{\Lambda 0} = 0$). The Friedmann model includes non-zero curvature on the Einstein-de Sitter model ($\Omega_{K0} \neq 0, \Omega_{\Lambda 0} = 0$) so that it is a little more complicated. However, our Universe is favored to be nearly zero curvature with positive dark energy density parameter ($\Omega_{K0} = 0, \Omega_{\Lambda 0} > 0$) by several observations. Therefore, I in this thesis explain only the flat model.

The Friedmann equation with the cosmological constant Λ is,

$$\left(\frac{\dot{a}}{a}\right)^2 = \frac{8\pi G}{3c^2}\rho - \frac{c^2 K}{a^2} + \frac{c^2 \Lambda}{3}. \tag{2.20}$$

Assuming the flat curvature ($K = 0$) and matter domination ($\rho \sim \rho_m = \rho_{m0}/a^3$), equation (2.20) is,

$$\left(\frac{\dot{a}}{a}\right)^2 = H_0^2 \left(\frac{\Omega_{m0}}{a^3} + \Omega_{\Lambda 0}\right). \tag{2.21}$$

Then, we can get the time differential equation:

$$\frac{\mathrm{d}a}{\mathrm{d}t} = H_0 \left[\frac{\Omega_{m0}}{a} + (1 - \Omega_{m0})a^2\right]^{1/2}, \tag{2.22}$$

where I utilize equation (2.19) to convert the curvature parameter to the density parameter of matter ($\Omega_{\Lambda 0} = 1 - \Omega_{m0}$). The integral form of equation (2.22) is,

$$H_0 t = \int_0^a \frac{\sqrt{a}\,\mathrm{d}a}{\sqrt{\Omega_{m0} + (1 - \Omega_{m0})a^3}}. \tag{2.23}$$

The integration can be conducted analytically. The solution form depends on the sign of the cosmological constant. For comparison, I show the negative and zero

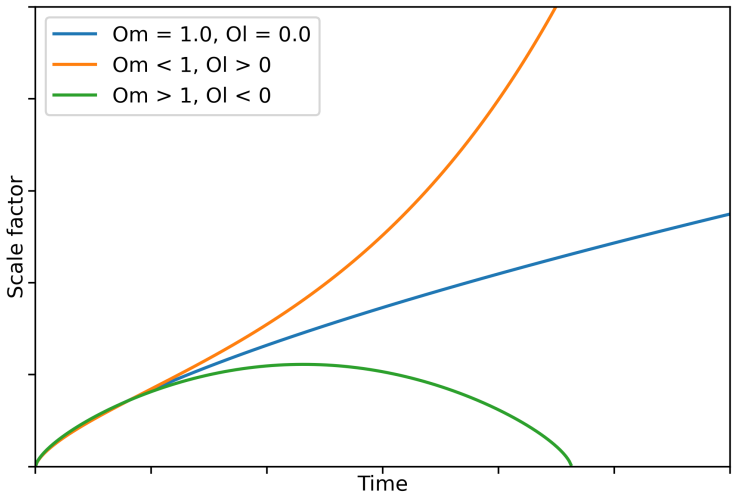

FIGURE 2.1: The time evolution of the scale factor in the flat lambda model. The green, orange, and blue lines are the cases of $\Omega_\Lambda < 0$, $\Omega_\Lambda > 0$, and $\Omega_\Lambda = 0$, respectively. The blue line corresponds to the Einstein-de Sitter model. The absolute vales of both axes are determined by the cosmological parameters, however, the shape of evolution is similar for different values of cosmological parameters.

lambda cases. When the cosmological constant is zero, the solution is identical with the solution of the Einstein-de Sitter model.

When $\Lambda > 0$ ($\Omega_{m0} < 1$):

$$a = \left(\frac{\Omega_{m0}}{1-\Omega_{m0}}\right)^{1/3} \sinh^{2/3}\left(\frac{3}{2}\sqrt{1-\Omega_{m0}}\, H_0 t\right). \tag{2.24}$$

When $\Lambda < 0$ ($\Omega_{m0} > 1$):

$$a = \left(\frac{\Omega_{m0}}{\Omega_{m0}-1}\right)^{1/3} \sinh^{2/3}\left(\frac{3}{2}\sqrt{\Omega_{m0}-1}\, H_0 t\right). \tag{2.25}$$

When $\Lambda = 0$ ($\Omega_{m0} = 1$)

$$a = \left(\frac{3}{2} H_0 t\right)^{2/3}, \tag{2.26}$$

which is the same as the Einstein-de Sitter universe.

The time-evolution of the scale factor in each case is shown in Figure 2.1. If the matter density is low and the cosmological constant has a positive value, the universe first expands and the speed of expansion decelerates. However, at the time,

$$t_{\rm acc} = \frac{\ln(2+\sqrt{3})}{3H_0\sqrt{1-\Omega_{m0}}}, \tag{2.27}$$

the expansion of the universe starts to accelerate because the dark energy density is constant while the matter density is decreasing with a^{-3}. The size of the universe

expands exponentially up to infinite. On the other hand, if a universe has a high matter density and a negative cosmological constant, the expansion stops at,

$$t_{\text{stop}} = \frac{\pi}{3H_0\sqrt{\Omega_{m0} - 1}}. \tag{2.28}$$

Then the size of the universe begins shrinking. Finally, at the time of,

$$t_{\text{crunch}} = 2t_{\text{turn}} = \frac{2\pi}{3H_0\sqrt{\Omega_{m0} - 1}}, \tag{2.29}$$

the big crunch at which $a = 0$ happens. From observations, our Universe is found to be the case of positive cosmological constant. To understand the cosmic evolution in more detail, we need to measure the values of cosmological parameters including Ω_Λ, which is described in Section 2.5.

2.4 Indicator of cosmological distance

Cosmological redshift

The wavelength of the light emitted in the Universe is extended due to the Hubble expansion. When the light is emitted in distant place, the extension can be non-negligible. Letting λ_0 being the wavelength at observer and λ_1 being that at emitter, the cosmological redshift z is defined as:

$$z \equiv \frac{\lambda_0 - \lambda_1}{\lambda_1}. \tag{2.30}$$

The relation with the scale factor is

$$a = \frac{1}{1+z}. \tag{2.31}$$

Cosmic age and distance

Using equation (2.7) and (2.31), the age of the Universe at redshift z is calculated with

$$t_{\cos} = \int \mathrm{d}t = \int \frac{\mathrm{d}t}{\mathrm{d}a}\frac{\mathrm{d}a}{\mathrm{d}z}\mathrm{d}z = -\int_\infty^z \frac{\mathrm{d}z}{H(1+z)}. \tag{2.32}$$

With the cosmological parameters of $\Omega_{\mathrm{m}} = 0.3$ and $\Omega_\Lambda = 0.7$, the cosmic age as o today is about 13 billion years old. At the redshift 20 around when the first generation of stars are believed to form, the cosmic age is about 200 million years old.

The cosmological distance, which is the distance a photon run from redshift z_1 to z_2, can be calculated in similar manner as the cosmic age,

$$l_{\cos} = a\int \frac{c\mathrm{d}t}{a} = \frac{1}{1+z}\int_{z_2}^{z_1} \frac{c\mathrm{d}z}{H}. \tag{2.33}$$

Note that $l_{\rm cos}$ is physical distance.

2.5 Observational constraint

Owing to the recent precise measurements such as the cosmic microwave background (CMB) and the type Ia supernova, tight constraints are successfully imposed on the cosmological parameters. I here introduce some examples.

The Figure 2.2 shows the observational constrains on the matter density parameter and dark energy parameters, and Figure 2.3 shows the constraint on the matter density parameter and the parameter of equation of state for dark energy, $p_{\rm d} = \omega\rho_{\rm d}$, assuming the flat lambda model. These constrains are derived from the observations of the CMB, the type I a supernova, and the baryon acoustic oscillation.

Explaining how each observation imposes the constraint is out of the scope of this thesis, however, the importance is that the parameters are well constrained so that we can conduct astrophysical researches to investigate thermal and structural histories using the well-constrained cosmological parameters.

As of today, the flat lambda model ($\Omega_K = 0$) in which three-fourth of total energy density is occupied with the dark energy is well consistent with all the observations. As far as we consider standard cosmological models, models without dark energy are rejected.

Throughout the thesis, we work on the flat ΛCDM Universe with the cosmological parameters constrained by the Planck satellite Planck Collaboration et al., 2016; the matter density, $\Omega_{\rm m0} = 0.308$, the baryon density, $\Omega_{\rm b0} = 0.0485$, the Hubble constant, $h_0 = 0.678$, the index of initial matter power spectrum, $n_{\rm s} = 0.968$, the rms mass fluctuation on 8 Mpc$/h$ scales at present day, $\sigma_8 = 0.828$, the mass fraction of Helium, $Y_{\rm He} = 0.249$. The types of the dark matter and its influences on the structure formation are explained in Section 3.2.4.

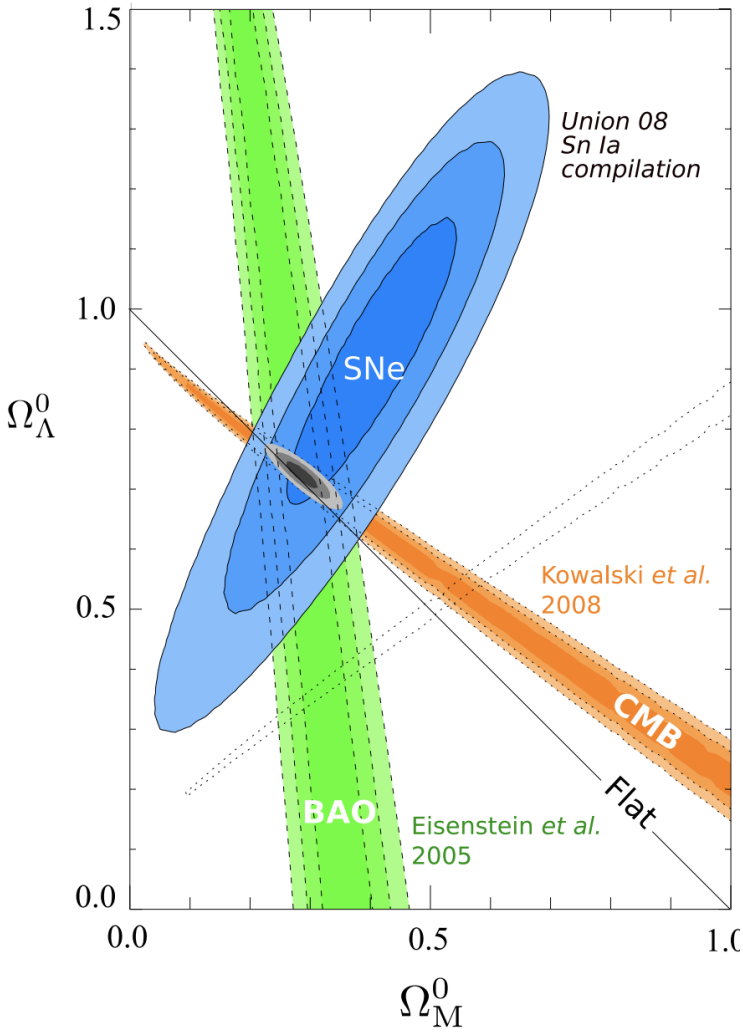

FIGURE 2.2: Constraint on Ω_{m0} and $\Omega_{\Lambda 0}$. The contour represents the statistical confidence levels of 68.3% (1σ), 95.4% (2σ) and 99.7% (3σ) from inside to outside. CMB: observation of cosmic microwave background, SNe: observation of distant supernova, BAO: observation of baryon acoustic oscillation. The gray contour is the combination of all the observation data. The figure is taken form Silvestri and Trodden, 2009.

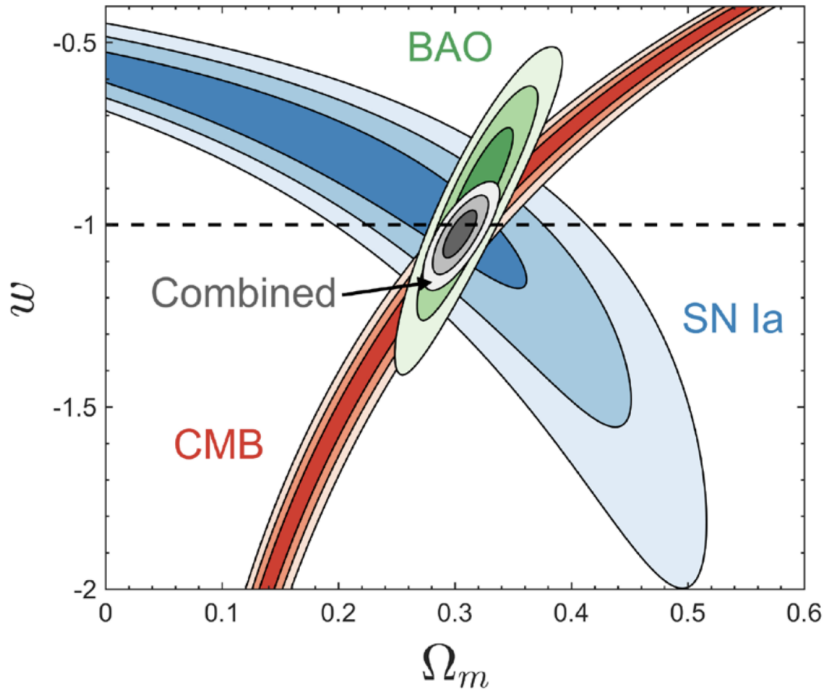

FIGURE 2.3: Constraint on Ω_{m0} and $\omega_{\rm d}$ The contour represents the statistical 68.3% (1σ), 95.4% (2σ) and 99.7% (3σ) confidence levels from inside to outside. CMB: observation of cosmic microwave background, SN Ia: observation of distant supernova, BAO: observation of baryon acoustic oscillation. The gray contour is the combination of all the observation data. The figure is taken form Huterer and Shafer, 2018.

Chapter 3

Structure formation

In the previous chapter, I described the basics of dynamical evolution of the Universe and explain that the constraints on the cosmological constants are fairly tight for discussing what has been happening in the Universe with the constrained parameters in the flat lambda model. I dedicate this chapter to summarize the basics of structure formation in the Universe. The CMB observation successfully revealed that the Universe at the early time is quite uniform. The fluctuations are as small as $\sim 10^{-5}$ in fraction. The variety of structures in the present Universe is formed from such small fluctuations with the help of the gravity. The theory of structure formation in which the gravity is thought to be driving force is called the gravitational instability theory. In the following I summarize the basics of the gravitational instability theory, starting from linear regime of matter fluctuations. The non-linear evolution, including the Zel'dvich approximation and cooling condition for star formation, are also described.

3.1 Linear perturbation theory

3.1.1 Basic equations

Only non-relativistic matter can grow and form a variety of structures in the Universe today. Relativistic radiation component has too large pressure to form structure. Therefore, I focus on the non-relativistic matter and depict the growth of its fluctuation, regarding the expanding Universe as background spacetime.

Assuming matter in the Universe can be well approximated as an ideal fluid, the states can be fully determined by mass density field, pressure field, and velocity field, $\rho_{\rm m}(\mathbf{r},t), p(\mathbf{r},t), v(\mathbf{r},t)$. The basic equations for the fluid are the continuous equation and the Euler equation, which can be written, in static and flat spatial coordinate $\mathbf{r}$, as

$$\frac{\partial \rho_{\rm m}}{\partial t} + \nabla \cdot (\rho_{\rm m}\mathbf{v}) = 0, \tag{3.1}$$

$$\frac{\partial \mathbf{v}}{\partial t} + (\mathbf{v}\cdot\nabla)\mathbf{v} = -\frac{\nabla p}{\rho_{\rm m}} - \nabla\phi, \tag{3.2}$$

where the $\phi(\mathbf{r}, t)$ is gravitational potential, $\nabla = \partial/\partial\mathbf{r}$. Equation (3.2) is the Newtonian equation of motion for fluid. The first term in the right hand side is the force applied by pressure gradient, and the second term corresponds to the force by gravity.

Now we re-written the two equations with the comoving coordinate $\mathbf{x} = \mathbf{r}/a$. The time derivative of the static coordinate $\mathbf{r}$ is expressed as

$$\dot{\mathbf{r}} = \dot{a}\mathbf{x} + a\dot{\mathbf{x}}. \tag{3.3}$$

The term $\dot{a}\mathbf{x}$ means the apparent velocity in the static coordination originated from the expanding background. Thus, in comoving coordination, the velocity component should be subtracted. To do that what should do is to replace $\mathbf{v}$ as $\mathbf{v} + \dot{a}\mathbf{x}$. Additionally, by converting time differential $\frac{\partial}{\partial t}$ and space differential ∇ appropriately in the coordination transformation of $(\mathbf{r}, t) \rightarrow (\mathbf{x}, t)$, equation (3.1) and (3.2) become,

$$\frac{\partial \rho_\mathrm{m}}{\partial t} + 3\frac{\dot{a}}{a}\rho_\mathrm{m} + \frac{1}{a}\nabla \cdot (\rho_\mathrm{m}\mathbf{v}) = 0, \tag{3.4}$$

$$\frac{\partial \mathbf{v}}{\partial t} + \frac{\dot{a}}{a}\mathbf{v} + \frac{1}{a}(\mathbf{v} \cdot \nabla)\mathbf{v} = -\frac{1}{a}\nabla\Phi - \frac{1}{\rho_\mathrm{m} a}\nabla p, \tag{3.5}$$

where, $\Phi = \phi + (1/2)a\ddot{a}|\mathbf{x}|^2$ whose second term compensates the apparent acceleration by expanding background in the static coordination. We need gravitational potential which is related with the deviation of matter density from the average,

$$\Delta\Phi = 4\pi G a^2(\rho_\mathrm{m} - \bar{\rho}_\mathrm{m}), \tag{3.6}$$

where we assume the energy density of the relevant fluid dominates other components. The assumption is fairly good approximation in the matter domination era. This equation is famous as the Poisson equation.

Taking spatial average of equation (3.4) produces,

$$\frac{d}{dt}(a^3\bar{\rho}_\mathrm{m}) = 0, \tag{3.7}$$

where, $\bar{\rho}_\mathrm{m}$ is the average of the mass density. This equation is corresponding to the conservation equation (2.6). We define the density fluctuation field $\delta(\mathbf{x}, t)$ and pressure fluctuation field $p(\mathbf{x}, t)$ as follows,

$$\delta(\mathbf{x}, t) = \frac{\rho_\mathrm{m}(\mathbf{x}, t) - \bar{\rho}_\mathrm{m}(t)}{\bar{\rho}_\mathrm{m}(t)}, \tag{3.8}$$

$$\delta p(\mathbf{x}, t) = p(\mathbf{x}, t) - \bar{p}(t), \tag{3.9}$$

where $\bar{p}$ is the average of pressure. Using equations (3.7), (3.8), and (3.9), the continuous equation (3.4) and the Euler equation (3.5) can be re-written as,

$$\frac{\partial \delta}{\partial t} + \frac{1}{a}\nabla \cdot [(1+\delta)\mathbf{v}] = 0, \tag{3.10}$$

$$\frac{\partial \mathbf{v}}{\partial t} + \frac{\dot{a}}{a}\mathbf{v} + \frac{1}{a}(\mathbf{v}\cdot\nabla)\mathbf{v} = -\frac{1}{a}\nabla\Phi - \frac{\nabla(\delta p)}{a\bar{\rho}_{\mathrm{m}}(1+\delta)}. \tag{3.11}$$

Also, the Poisson equation (3.6) becomes,

$$\Delta\Phi = \frac{4\pi G}{c^2}a^2\bar{\rho}\delta. \tag{3.12}$$

The equations (3.10), (3.11), and (3.12) are the basic equations to describe time-evolution of mass density fluctuation of non-relativistic matter in the expanding Universe. The degree of freedom of variables $\delta, \delta p, \mathbf{v}$ is five. On the other hand, the number of equations except for the Poisson equation is four. Therefore, we additionally need the equation of state to solve the equations.

3.1.2 Jeans instability

The gravity is attraction force. Thus, in early time, regions which are little bit denser attract more matter and become even denser. Then, the regions attract surrounding matter more strongly. This cycle lets initial small fluctuations extremely large at later time. However, if the pressure, which works as repulsive force, is strong enough to support the gravity force, the fluctuations can no longer grow. This leads to the condition for fluctuations to grow by gravitational instability.

The fluctuations are initially small probed by the CMB observation $\sim 10^{-5}$. The small fluctuations have to grow as a first step of structure formation. Thus, we first use linear approximation leaving only first order terms. By using equation (3.10) and equation (3.11), and deleting the velocity field $\mathbf{v}$, we obtain

$$\frac{\partial^2\delta}{\partial t^2} + 2\frac{\dot{a}}{a}\frac{\partial\delta}{\partial t} - \frac{\delta(\delta p)}{a^2\bar{\rho}_{\mathrm{m}}} = \frac{4\pi G}{c^2}\rho\delta, \tag{3.13}$$

where we assume the self-gravitating system, which means the relevant component dominates the other components. In addition, we assume the entropy fluctuation can be neglected ($\delta S = 0$), where S is the entropy per unit mass. Under the assumption, the equation of state $p = p(\rho_{\mathrm{m}}, S)$ can be expanded as,

$$\delta p = \left(\frac{\partial p}{\partial \rho_{\mathrm{m}}}\right)_S \bar{\rho}_{\mathrm{m}}\delta = c_{\mathrm{s}}^2\bar{\rho}_{\mathrm{m}}\delta, \tag{3.14}$$

where c_s is the speed of sound $c_s^2 = (\partial p/\partial \rho_m)_S$. Then, equation (3.13) can be re-written as,

$$\frac{\partial^2 \delta}{\partial t^2} + 2\frac{\dot{a}}{a}\frac{\partial \delta}{\partial t} - \left(4\pi G\bar{\rho}_m \delta + \frac{c_s^2}{a^2}\Delta\delta\right) = 0. \tag{3.15}$$

Converting equation (3.15) in Fourier space provides us with clear understanding of time-evolution of matter fluctuation in each scale indeed. The Fourier transformation and its inverse transformation of the mass density fluctuation are,

$$\tilde{\delta}(\mathbf{k}, t) = \int d^3x e^{-i\mathbf{k}\cdot\mathbf{x}}\delta(\mathbf{x}, t), \tag{3.16}$$

$$\delta(\mathbf{x}, t) = \int \frac{d^3k}{(2\pi)^3} e^{i\mathbf{k}\cdot\mathbf{x}}\tilde{\delta}(\mathbf{k}, t). \tag{3.17}$$

Then, equation (3.15) in Fourier space is,

$$\frac{\partial^2 \tilde{\delta}}{\partial t^2} + 2\frac{\dot{a}}{a}\frac{\partial \tilde{\delta}}{\partial t} - \left(4\pi G\bar{\rho}_m - \frac{c_s^2 k^2}{a^2}\right)\tilde{\delta} = 0. \tag{3.18}$$

Each Fourier mode evolves independently in linear approximation. Since different modes do not interact each other, the analysis is simple and we can obtain clear insight. Hereafter, we focus only on δ in Fourier space, and thus, we write $\tilde{\delta}$ as simply δ.

Equation (3.18) can be seen as the Newtonian equation of motion regarding δ as position of a particle. The first term corresponds to the acceleration of the particle. The second term can be understood as the friction proportional to the velocity. Also, we can recognize the third term as potential force depending on the particle position. The potential is $V(\delta) = -0.5\delta^2(4\pi G\rho_m - c_s^2 k^2/a^2)$.

Depending on the sign of $A \equiv 4\pi G\rho_m - c_s^2 k^2/a^2$, the behavior of δ is different. If A is negative, the potential is convex downward. The fluctuation δ can not grow because the δ oscillates as it is damping. This happens when the speed of sound is large, in other words, the pressure is large. The gravity which shrinks a over-dense region and the pressure which pushes back the region competes each other. Resultantly, the region oscillates. This oscillation phenomenon is so-called the acoustic oscillations.

If A is positive, on the contrary, the potential is convex upward. In this case, the fluctuation can grow even though the friction works as suppression. The gravity overcomes the pressure and matter contracts gravitationally. The friction is originated from the Hubble expansion. Namely, the expansion of the Universe suppress the growth of matter fluctuation.

$A = 0$ gives us the condition for the growth of fluctuation. The critical wave number $k_{\rm J}$ is,

$$k_{\rm J} = \frac{a\sqrt{4\pi G\bar{\rho}_{\rm m}}}{c_{\rm s}^2}. \tag{3.19}$$

The length of the scale is,

$$\lambda_{\rm J} \equiv \frac{2\pi a}{k_{\rm J}} = c_{\rm s}\sqrt{\frac{\pi}{G\bar{\rho}_{\rm m}}}. \tag{3.20}$$

The fluctuation whose scale is shorter than the $\lambda_{\rm J}$ can not grow due to pressure, and on the other hand, the fluctuation whose scale is longer can grow. This critical length $\lambda_{\rm J}$ is called the Jeans length. Also the mass in the sphere whose diameter is the Jeans length is called the Jeans mass which is expressed as follows:

$$M_{\rm J} \equiv \frac{4\pi\bar{\rho}_{\rm m}}{3}\left(\frac{\lambda_{\rm J}}{2}\right)^3 = \frac{\pi^{5/2}}{6}\frac{c_{\rm s}^3}{\sqrt{G^3\bar{\rho}_{\rm m}}}. \tag{3.21}$$

This provides us with the minimum mass of object that can grow through the gravitational instability.

3.1.3 Growth of density fluctuation

At much larger scales than the Jeans scale, the pressure is much weaker than gravity. Therefore, the time-evolution equation (3.18) becomes,

$$\ddot{\delta} + 2H\dot{\delta} - 4\pi G\bar{\rho}_{\rm m}\delta = 0. \tag{3.22}$$

To understand the time-evolution of fluctuation, we first apply equation (3.22) to the Einstein-de Sitter cosmological model. Using equation (2.26), and the energy density $\rho = \rho_0/a^3 = c^2/(6\pi G t^2)$, the Hubble parameter and the average mass density are,

$$H = \frac{\dot{a}}{a} = \frac{2}{3t}, \tag{3.23}$$

$$\bar{\rho}_{\rm m} = \frac{1}{6\pi G t^2}. \tag{3.24}$$

Then, equation (3.22) can be written as,

$$\ddot{\delta} + \frac{4}{3t}\dot{\delta} - \frac{2}{3t^2}\delta = 0. \tag{3.25}$$

By substituting $\delta \propto t^n$, we find the solutions of $n = 2/3, -1$. Thus, the general solution should be,

$$\delta = At^{2/3} + Bt^{-1}, \tag{3.26}$$

where, the first term is called the growing mode, and the second term is called the decaying mode. The decaying mode decreases rapidly as time passes so that the

term can not contribute to the structure formation. While, the growing mode has the same dependence on time as the scale factor does $a \propto t^{2/3}$, which suggests that the density fluctuation evolves as $\delta \propto a$ in the matter domination era.

In cases with non-zero curvature parameter and a cosmological constant, the solutions can be obtained analytically. The growing mode and the decaying mode are, respectively,

$$D_+ \propto H \int_0^a \frac{da}{a^3 H^3}, \tag{3.27}$$

$$D_- \propto H. \tag{3.28}$$

The $D_+(t)$ is particularly called the linear growth factor. After the matter domination, the Hubble parameter is expressed as,

$$H = H_0 \sqrt{\frac{\Omega_{\mathrm{m}0}}{a^3} + \Omega_{\Lambda 0} + \frac{1 - \Omega_{\mathrm{m}0} - \Omega_{\Lambda 0}}{a^2}}. \tag{3.29}$$

The linear growth factor can be written using the cosmological parameters Ω_{m} and Ω_Λ,

$$D_+ = \frac{5}{2} a \Omega_{\mathrm{m}} \int_0^1 \frac{dx}{(\Omega_{\mathrm{m}}/x + \Omega_\Lambda x^2 + 1 - \Omega_{\mathrm{m}} - \Omega_\Lambda)^{3/2}}. \tag{3.30}$$

If long enough time passes after the fluctuation starts to grow, neglecting the decaying mode is a good approximation. Thus, writing the density fluctuation at present time as $\delta_0(\mathbf{x})$, the density fluctuation in the past can be estimated by,

$$\delta(\mathbf{x}, t) = D(t)\delta_0(\mathbf{x}), \tag{3.31}$$

where, $D(t) \equiv D_+(t)/D_+(t_0)$ is the normalized linear growth factor.

3.2 Non-linear regime

In the previous section, I introduce the density fluctuation with linear approximation. The linear method is a good approximation as long as the fluctuation δ is much smaller than one. However, when the value of δ increases and becomes order of unity by the gravitational instability, the accuracy gets worse. In such non-linear regime, each Fourier mode starts to get coupled with the other modes, which makes calculation of the fluctuation growth more complicated. In the following, how we can approximately treat the non-linear evolution is described.

3.2.1 Spherical collapse model

The spherical collapse model is often used to investigate the non-linear evolution of the density fluctuation approximately. In this model, we work with a spherical density distribution. The center of the each spherical shell is located at a point.

We here neglect the velocity dispersion. Then, we can treat the system as a simple one-dimensional problem. For simplicity, we assume the Einstein-de Sitter model universe.

The force applied on a shell whose radius is R is determined only by the mass which is packed within R. Therefore, the equation of motion is

$$\frac{\mathrm{d}^2 R}{\mathrm{d}t^2} = -\frac{GM}{R^2}. \tag{3.32}$$

In the expanding universe, the shell has initially outward velocity. By integrating the equation of motion once,

$$\left(\frac{\mathrm{d}R}{\mathrm{d}t}\right)^2 = \frac{2GM}{R} + 2E, \tag{3.33}$$

where E is the integration constant, which corresponds to the total energy per unit mass. In the case of $E < 0$, integrating the equation above again provides us with

$$R = (GM)^{1/3} A^2 (1 - \cos\theta), \tag{3.34}$$

$$t = A^3 (\theta - \sin\theta), \tag{3.35}$$

while in the case of $E > 0$,

$$R = (GM)^{1/3} A^2 (\cosh\theta - 1), \tag{3.36}$$

$$t = A^3 (\sinh\theta - \theta), \tag{3.37}$$

where A is an integration constant. The mass density of the shell ρ_m is

$$\rho_\mathrm{m} = \frac{3M}{4\pi R^3}. \tag{3.38}$$

Since the background density in the Einstein-de Sitter universe is given by equation (3.24), the density fluctuation in the shell is

$$\delta(t) = \frac{9GMt^2}{2R^3} - 1, \tag{3.39}$$

where t is related to R with θ; In the case of $E < 0$,

$$\delta(t) = \frac{9}{2}\frac{(\theta - \sin\theta)^2}{(1 - \cos\theta)^3} - 1. \tag{3.40}$$

On the other hand, in the case of $E > 0$,

$$\delta(t) = \frac{9}{2}\frac{(\sinh\theta - \theta)^2}{(\cosh\theta - 1)^3} - 1. \tag{3.41}$$

When $E > 0$, the shell has enough energy to expand eternally. Thus no object can form. While, if $E < 0$, the expansion stops in finite time and start shrinking toward the center. The radius is maximum at the turning-around point $\theta = \pi$. The time and radius at the point are, respectively,

$$t_{\rm turn} = \pi A^3, \tag{3.42}$$

$$R_{\rm turn} = 2(GM)^{1/3}A^2. \tag{3.43}$$

The density fluctuation at the point is,

$$\delta_{\rm turn} = \frac{9\pi^2}{16} - 1 \sim 4.55. \tag{3.44}$$

At the point when the shell radius becomes zero, the density diverges to infinity. This divergence point corresponds to $\theta = 2\pi$. The time at the point is

$$t_{\rm coll} = 2t_{\rm turn} = 2\pi A^3. \tag{3.45}$$

The time from the turning-around to the collapse is so-called the free-fall timescale. With the density $\rho_{m,\rm turn} = 3M/(4\pi R_{\rm turn}^3)$, the free-fall time scale is

$$t_{\rm ff} = t_{\rm coll} - t_{\rm turn} = \pi A^3 = \sqrt{\frac{3\pi}{32G\rho_{\rm m,turn}}}. \tag{3.46}$$

Expanding the equations 3.34 and 3.40 gives

$$\delta = \frac{3}{20}\theta^2 + O(\theta^4), \tag{3.47}$$

$$t = \frac{A^3}{6}\theta^3 + O(\theta^5). \tag{3.48}$$

The time dependence of the first-order term ($\delta \propto t^{2/3}$) is identical with the linear evolution of density fluctuation (equation 3.26). The first term which we define as $\delta_{\rm L}$ can be written by

$$\delta_{\rm L}(t) = \frac{3(6t)^{2/3}}{20A^2}. \tag{3.49}$$

Then the values of the fluctuation at the turning-around point and collapse point are,

$$\delta_{\rm L}(t_{\rm turn}) = \frac{3(6\pi)^{2/3}}{20} \sim 1.06, \tag{3.50}$$

$$\delta_{\rm L}(t_{\rm coll}) = \frac{3(12\pi)^{2/3}}{20} \sim 1.69. \tag{3.51}$$

The results suggest that when the linear density fluctuation grows and become $\delta_{\rm L} =$

1.69, the non-linear spherical fluctuation indeed collapses, that is, some objects form. Although we proceed the calculations in the Einstein-de Sitter model until here, the values in different cosmological models do not change significantly.

3.2.2 Virial theorem

In the spherical collapse model, the density fluctuation diverges at the collapse point. However, the velocity dispersion is not negligible in reality so that the velocity-dispersion-supported system forms instead. When a system is gravitationally bound and in equilibrium, the total energy equals to the half of time-averaged potential energy, which is so-called the Virial theorem:

$$\langle E \rangle = \frac{1}{2}\langle U \rangle. \tag{3.52}$$

Because $E = K + U$, where K is the kinetic energy, the relation between the kinetic energy and the potential energy is

$$\langle K \rangle = -\frac{1}{2}\langle U \rangle. \tag{3.53}$$

Now we adopt the virial theorem to a simple case which is the gravitationally bound uniform sphere with radius R and mass M. The system is in equilibrium and has uniform mass density. The mass density is $\rho_{\rm m} = 3M/(4\pi R^3)$. The total mass inside a radius r ($0 < r < R$) is $4\pi r^3 \rho_{\rm m}/3 = Mr^3/R^3$. Also, the mass of a shell with width dr is $4\pi r^2 \rho_{\rm m} {\rm d}r = 3Mr^2 {\rm d}r/R^3$. Therefore, the potential energy of the unifrom sphere is

$$U = -\frac{3}{5}\frac{GM^2}{R}. \tag{3.54}$$

Then using the virial theorem provides us with the kinetic energy and the total energy,

$$K = \frac{3}{10}\frac{GM^2}{R}. \tag{3.55}$$

$$E = -\frac{3}{10}\frac{GM^2}{R}. \tag{3.56}$$

For simplicity, we assume the system consists of N particles with mass m so that $M = Nm$. Using the velocity dispersion $\sigma^2 = \sum_i |\mathbf{v}_i|^2/N$, where $\mathbf{v}_i$ is the velocity of the partile i, the kinetic energy is,

$$K = \frac{1}{2}m\sum_{i=1}^{N}|\mathbf{v}_i^2| = \frac{1}{2}M\sigma^2. \tag{3.57}$$

With equations (3.55) and (3.57),

$$\sigma^2 = \frac{3}{5}\frac{GM}{R}. \tag{3.58}$$

The velocity dispersion on the line of sight is relatively easy to observe. Assuming the isotropic velocity dispersion, the line-of-sight value equals to $\sigma_{\rm r}^2 = \sigma^2/3$. The mass defined with the $\sigma_{\rm r}$

$$M_{\rm vir} = \frac{5R\sigma_{\rm r}^2}{G}, \tag{3.59}$$

is the virial mass. This mass is derived from the simplified system so that it is not the exact mass of the observed object. However, the virial mass is frequently used as a roughly estimated value and is more importantly useful.

Next, we work on a uniform sphere, whose radius is R, composed of N particles of ideal gas with average molecular weight of μ. In this case, the velocity dispersion of the molecules can be written as

$$\langle v^2 \rangle = \frac{1}{N\mu m_{\rm H}} \sum_i m_i |\mathbf{v}_i|^2. \tag{3.60}$$

The kinetic energy is

$$K = \frac{1}{2} N\mu m_{\rm H} \langle v^2 \rangle. \tag{3.61}$$

With the virial theorem (equation 3.55) and $M = N\mu m_{\rm H}$,

$$\langle v^2 \rangle = \frac{3}{5}\frac{GM}{R}. \tag{3.62}$$

Regarding the kinetic energy as thermal energy and adopting the law of equipartition of energy $(1/2)\mu m_{\rm H}\langle v^2 \rangle = (3/2)k_{\rm B}T$, we define the temperature as the virial temperature:

$$T_{\rm vir} = \frac{\mu m_{\rm H} \langle v^2 \rangle}{3k_{\rm B}}. \tag{3.63}$$

In the case of uniform sphere (equation 3.62), the virial temperature is

$$T_{\rm vir} = \frac{GM\mu m_{\rm H}}{5k_{\rm B}R}. \tag{3.64}$$

Finally we adopt the virial theorem to the spherical collapse model discussed in the previous section. The potential of the system can be obtained with equation (3.54). At the turning-around point, the velocity of the shell becomes zero so that the potential energy at the time should be the same as the total energy of the system,

$$E = -\frac{3}{5}\frac{GM^2}{R_{\rm turn}}. \tag{3.65}$$

After turning around, the system begins to shrink. The sphere collapse to a central

point and the density diverges to infinity. But, the velocity dispersion supports the system in reality and the system reaches the virial equilibrium. The potential energy at the radius $R_{\rm vir}$,

$$U_{\rm vir} = -\frac{3}{5}\frac{GM^2}{R_{\rm vir}}. \tag{3.66}$$

With equations (3.65) and (3.52), the radius $R_{\rm vir}$,

$$R_{\rm vir} = \frac{1}{2}R_{\rm turn}. \tag{3.67}$$

Since it roughly takes the free-fall timescale to reach the virial equilibrium, we assume the system is in equilibrium at the time $t_{\rm coll}$. The background density at the time is $\bar{\rho}_{\rm m,coll} = 1/(6\pi G t_{\rm coll})$. Also using the density of the system $\rho_{\rm m,coll} = 3M/(4\pi R_{\rm vir}^3)$, the density fluctuation is

$$\delta_{\rm coll} = 18\pi^2 - 1 \sim 177. \tag{3.68}$$

Namely, the mass density of objects which is in the virial equilibrium is roughly 178 times denser than the background density at the collapse time.

3.2.3 Zel'dvich approximation

To analyze the non-linear evolution of non-spherical fluctuation is extremely difficult. Therefore, some approximation methodologies have been invented. I here describe the Zel'dvich approximation which is one of the analytical methods (Zel'Dovich, 1970).

In linear perturbation theory, the states of fluids such as mass density filed and velocity filed are expressed as functions of comoving coordinate x. This approach is called the Euler specification. On the other hand, using the coordination q which is sticked on a small fragment of fluid and tracing the dynamical evolution of the small fragment is the other approach which is so-called the Lagrangian specification. the coordinate q is called the Lagrange coordinate. The Zel'dvich approximation is based on the Lagrangian specification.

The Euler coordinate is related with the Lagrange coordinate as,

$$\mathbf{x}(\mathbf{q}, t) = \mathbf{q} + \mathbf{p}(\mathbf{q}, t), \tag{3.69}$$

where the $\mathbf{p}$ is displacement vector field. In the following, we try to write the density fluctuation and velocity with the displacement field $\mathbf{p}$. The mass density filed in the Euler coordinate is $\rho_{\rm m}(\mathbf{x}, t)$. In ideally homogeneous and isotropic universe, $\mathbf{x} = \mathbf{q}$ is satisfied and the mass density is $\bar{\rho}_{\rm m}(t)$ everywhere in the universe. Then the mass

conservation between the ideal universe and the inhomogeneous universe gives us,

$$\rho_{\mathrm{m}}(\mathbf{x}, t)\mathrm{d}^3x = \bar{\rho}_{\mathrm{m}}(t)\mathrm{d}^3q. \tag{3.70}$$

Using Jacobian, the density field can be written as

$$\rho_{\mathrm{m}}(\mathbf{x}, t) = \frac{\bar{\rho}_{\mathrm{m}}(t)}{\det(\partial\mathbf{x}/\partial\mathbf{q})} = \frac{\bar{\rho}_{\mathrm{m}}(t)}{\det(\delta_{ij} + \partial p_i/\partial q_j)}. \tag{3.71}$$

If the fluctuation is small, $\partial\mathbf{p}/\partial\mathbf{q}$ should be small. Thus, we expand about the value and hold only the first order term. Then the density fluctuation is

$$\delta(\mathbf{x}, t) = \frac{\rho_{\mathrm{m}}(\mathbf{x}, t)}{\bar{\rho}_{\mathrm{m}}} - 1 \approx -\nabla_{\mathbf{q}} \cdot \mathbf{p}, \tag{3.72}$$

where, $\nabla_{\mathbf{q}} = \partial/\partial\mathbf{q}$ is the gradient in Lagrange coordinate. While the velocity is

$$\mathbf{v}(\mathbf{x}, t) = a\dot{\mathbf{x}}(\mathbf{q}, t) = a\dot{\mathbf{p}}(\mathbf{q}, t). \tag{3.73}$$

Equations (3.72) and (3.73) are the functions of Euler coordinate $\mathbf{x}$. However, even if we replace $\mathbf{x}$ with $\mathbf{q}$, the difference comes from second and higher orders. Thus, as long as the δ is sufficiently small, the difference is tiny.

In linear regime, the fluctuation δ and velocity v should be consistent with the solutions of the linear theory. In Zel'dvich approximation, the displacement vector is determined so that equations (3.72) and (3.73) are consistent with the solution of the linear perturbation theory. Then, the $\mathbf{p}$ can be written as,

$$\mathbf{p}(\mathbf{q}, t) = D(t)\nabla_{\mathbf{q}}\psi_0(\mathbf{q}), \tag{3.74}$$

where, the $\psi_0(\mathbf{q})$ is not dependent on time but only on Lagrange coordinate $\mathbf{q}$, and it is calculated from the gravitational potential,

$$\psi_0(\mathbf{q}) = -\frac{\Phi_0(\mathbf{q})}{4\pi G\bar{\rho}_{\mathrm{m}}}, \tag{3.75}$$

where, the Φ_0 is the current value of gravitational potential.

The Zel'dvich approximation is the method to extrapolate the linear time-evolution of displacement field $\mathbf{p}$ and resulting fluctuation and velocity fields (equations (3.72) and (3.73)) to non-linear regime. Therefore, the accuracy decreases as non-linearity grows. However, compared with the N-body simulation, which calculates gravitational acceleration of each particle at each time step, the Zel'dvich approximation is computationally low-cost. Accordingly, it is often used especially in researches related with the structure formation on large scales.

3.2.4 Dark matter classification

Many of observations say that the dominant component among matter in the Universe is not baryon but the dark matter. However, what the dark matter is or what properties the dark matter has are not perfectly understood yet. The dark matter is defined as a matte that interacts only through gravity.

As for the structure formation with dark matter, the free streaming is essential. If the dark matter has the velocity dispersion, the free motion damps the fluctuations on small scales. The velocity dispersion is different in different models of dark matters. Thus, to observe the free-streaming effect is a strong way to constraint the models.

We assign $v(t)$ to typical velocity of dark matter particle. When particles run in a timescale $\mathrm{d}t$, we write the distance as $\mathrm{d}x$. Then $v(t)\mathrm{d}t = a(t)\mathrm{d}x$ is satisfied. Thus, the comoving scale of free streaming of the dark matter can be written as,

$$L_{\mathrm{fs}}(t) = \int_0^t \frac{v(t')}{a(t')}\mathrm{d}t' = \int_0^{a(t)} \frac{v\mathrm{d}a}{a^2 H}, \tag{3.76}$$

where we assume the particles decouple from other energy components and move freely at sufficiently early time, and therefore, we take zero as the lower limit of the integration.

When the particles are relativistic, its velocity is the speed of light. After the particles become non-relativistic, the velocity decreases as approximately,

$$v \sim \begin{cases} c & (a < a_{\mathrm{nr}}) \\ ca_{\mathrm{nr}}/a & (a > a_{\mathrm{nr}}) \end{cases} \tag{3.77}$$

where a_{nr} is the scale factor at which the dark matte particles become non-relativistic. If $a_{\mathrm{nr}} > a_{\mathrm{eq}}$, where a_{eq} is the scale factor at the matter-radiation equality, the dark matter behave as radiation and cannot contribute the structure formation. Thus, we work on the assumption of $a_{\mathrm{nr}} < a_{\mathrm{eq}}$.

We divide the integration in equation (3.76) into two parts: (1) before a_{nr} and (2) between a_{nr} and a_{eq}. Since the Hubble parameter in radiation domination evolve as $H(a) \approx H_0 \Omega_{\mathrm{r0}}^{0.5} a^{-2}$,

$$L_{\mathrm{fs}} \approx \frac{c}{H_0\sqrt{\Omega_{\mathrm{r0}}}} \int_0^{a_{\mathrm{nr}}} \mathrm{d}a + \frac{ca_{\mathrm{nr}}}{H_0\sqrt{\Omega_{\mathrm{r0}}}} \int_{a_{\mathrm{nr}}}^{a_{\mathrm{eq}}} \frac{\mathrm{d}a}{a} \tag{3.78}$$

$$= \frac{ca_{\mathrm{nr}}}{H_0\sqrt{\Omega_{\mathrm{r0}}}} \left[1 + \ln\left(\frac{a_{\mathrm{eq}}}{a_{\mathrm{nr}}}\right)\right]. \tag{3.79}$$

Thus, the important factor which determines the free-streaming scale is the time, a_{nr}.

If the dark matter particles become non-relativistic at sufficiently early time, the

particles do not have enough time to erase the roughness of the initial density fluctuation. In contrast, if the particles have large $a_{\rm nr}$, the fluctuation is flattened at larger scales.

$a_{\rm nr}$ is different for different types of dark matters. Therefore, dark matters are classified into three types depending on $a_{\rm nr}$: Hot Dark Matter, Warm Dark Matter, and Cold Dark Matter. The hot dark matter has the largest $a_{\rm nr}$, namely, the free-streaming effect affects on largest scales, while, the fluctuation reduction of the cold dark matter is negligible. The intermediate type is the warm dark matter.

Hot dark matter

In the case of hot dark matter, the structure formation starts from large scales which are not affected by the free-streaming of the dark matter particles. For example, neutrinos are classified as the hot dark matter. Their free-streaming scales are larger than that of superclusters. In the collapsed object, the smaller objects such as galaxy clusters and galaxies can form by the non-linear evolution. This story of structure formation is called the top-down scenario.

Observations reveal that the galaxies in the Universe have existed longer than the galaxy clusters. Also superclusters are now in the process of the formation. Therefore, the top-down scenario is not considered to be realistic.

Cold dark matter

The cold dark matter do not erase the small scale fluctuations. Variety of observations are consistent with this type of dark matter, and thus, the cold dark matter is in the standard model in recent years. For instance, the Weakly Interacting Massive Particles (WIMP) and Axion are classified as the cold dark matter.

In contrast to the hot dark matter, the small scale fluctuations remain preserved, hence, the smaller objects first form. Such small objects gather at later time and form larger objects. This story of structure formation is so-called bottom-up scenario.

Warm dark matter

Although the cold dark matter is the standard model, there is well-known missing-satellite problem (e.g. Kauffmann, White, and Guiderdoni, 1993; Moore et al., 1999) The theoretical prediction of the cold dark matter says that there should be more small scale structures compared with observations. In order to solve the difference between theory and observations, a dark matter whose free-streaming affects the relevant small scales has been considered. This intermediate type of dark matter is called the warm dark matter. However, such small objects should be influenced by non-linearity and baryonic physics which are highly complicated. Thus, whether

the missing-satellite problem is originated only from the dark matter free-streaming length is uncertain as of today.

3.3 Cosmological statistics

In the previous sections, I describe how the density fluctuation arisen in the early time evolves in both linear and non-linear regime in which approximation methods are utilized. The fluctuation itself is observable, however, theory does not predict a concrete value at a point of the Universe. What the theory forecasts is its statistical properties. In this section, I explain the two-point correlation function of the fluctuation and the power spectrum which corresponds to its Fourier transformation.

3.3.1 Tow point correlation function

Let us consider density fluctuation at $\mathbf{x}_\mathrm{A}$ and $\mathbf{x}_\mathrm{B}$. Fixing the distance of the two points, $x_\mathrm{AB} \equiv |\mathbf{x}_\mathrm{A} - \mathbf{x}_\mathrm{B}|$, we take ensemble average of the product of the two fluctuation values,

$$\xi(x_\mathrm{AB}) = \langle \delta(\mathbf{x}_\mathrm{A}) \delta(\mathbf{x}_\mathrm{B}) \rangle. \tag{3.80}$$

The $\xi(x_\mathrm{AB})$ is the two-point correlation function. If the values of density field distribute randomly regardless of values at other places, the correlation function should be zero. While, when $\delta(\mathbf{x}_\mathrm{A})$ is large and places whose distance is away from $\mathbf{x}_\mathrm{A}$ by x_AB tend to have large δ, then the correlation function has a positive value. In contrast, when they tend to have low density, the value should be negative.

Sine the spatial average of density fluctuation is zero, by integrating equation (3.80),

$$\int_0^\infty \mathrm{d}x x^2 \xi(x) = 0. \tag{3.81}$$

The two-point correlation function satisfies the condition above.

I here introduce the two-point correlation function which tells us the information on the statistical property of density fluctuation. But, the correlation function can be expanded to N-point correlation functions and the fluctuations in general has non-zero values of N-point correlations.

As special case, the probability field whose three-points or more correlations are all zero is called the Gaussian filed. By observations, the initial density fluctuation in the Universe is found to be fairly close to the Gaussian filed. If the non-Gaussianity is detected, it can in principle constrain the inflation models which affect the initial fluctuation.

3.3.2 Power spectrum

The power spectrum is the Fourier transformation of the two-point correlation function. By using equations (3.16) and (3.17) which are the Fourier transformation of fluctuation,

$$\langle\tilde{\delta}(\mathbf{k})\tilde{\delta}(\mathbf{k}')\rangle = \int \mathrm{d}x_{\mathrm{A}}^3 \mathrm{d}^3 x_{\mathrm{B}} e^{-i\mathbf{k}\cdot\mathbf{x}_{\mathrm{A}} - i\mathbf{k}'\cdot\mathbf{x}_{\mathrm{B}}} \xi(|\mathbf{x}_{\mathrm{A}} - \mathbf{x}_{\mathrm{B}}|). \tag{3.82}$$

The integration of the right hand side fixing x_{B} leads to the definition of the power spectrum $P(k)$ under the cosmological principle,

$$\langle\tilde{\delta}(\mathbf{k})\tilde{\delta}(\mathbf{k}')\rangle = (2\pi)^3\delta_{\mathrm{D}}^3(\mathbf{k}+\mathbf{k}') \int \mathrm{d}^3 x e^{-i\mathbf{k}\cdot\mathbf{x}} \xi(|\mathbf{x}|) \tag{3.83}$$

$$\equiv (2\pi)^3\delta_{\mathrm{D}}^3(\mathbf{k}+\mathbf{k}')P(k). \tag{3.84}$$

The power spectrum and the two-point correlation function are Fourier transformation of each other,

$$P(k) = \int \mathrm{d}^3 x e^{-i\mathbf{k}\cdot\mathbf{x}} \xi(|\mathbf{x}|), \tag{3.85}$$

$$\xi(x) = \int \frac{\mathrm{d}^3 k}{(2\pi)^3} e^{i\mathbf{k}\cdot\mathbf{x}} P(|\mathbf{k}|). \tag{3.86}$$

This relation is called the Wiener-Khintchine relation.

3.4 Star Formation in high redshift Universe

Until here in this chapter, we understand how the density fluctuation grows and the resultant halo formation. In the haloes which is composed of dark matter, the star formation occurs. Since stars are made of baryon gas, baryon physics is the key. Stars play various roles in thermal history and structure formation history of the Universe. Thus, in this section, I briefly summarize the classification of stars, their roles, and the observational aspects, especially focusing on the high redshift Universe.

3.4.1 Stellar population

Stars in the Universe can be classified into three populations, roughly depending on the abundance of heavy elements, that is metalicity (e.g. Hirano et al., 2015). Highly-metaled stars are called population I stars (pop I stars). The most observed stars in our galaxy, especially at the disk, are the pop I stars. The sun is classified in the pop I group. The abundance of hydrogen and helium of the sun is about 71 % and 27%. The element heavier than helium is about 2%. The ages of the observed pop I stars range from very young age to 10 billion years.

On the other hand, the population II stars (pop II stars) have little metalicity of around 1% of solar metalicity. The pop II stars are found to belong to bulge and halo. The estimated ages of the pop II stars are more than 10 billion years in most cases. Thus, the pop II stars are expected to have formed in the early Universe younger than 10 billion-year-old.

Finally, the population III stars are defined as zero-metal stars. The big bang nucleosynthesis does not create heavy elements, and therefore, the primordial gas must not have the metals. Consequently the first generation of stars in the Universe, which are so-called the first stars, are metal-free stars. Thus, the first stars are classified as Pop III stars. Even after the first generation of stars form, some places in the Universe can remain metal-free. For example, low-density regions begin star formation later than higher-density regions do. Such regions can hold no-metal gas at later time and possibly create Pop III stars (Mebane, Mirocha, and Furlanetto, 2018). In addition, less massive Pop III stars than $0.8M_{\odot}$ have longer age than cosmic age so that they can survive at present Universe even if they are born at early time. Simulations suggest that such survived Pop III stars are concentrated at the central region of halo and subhaloes (Ishiyama et al., 2016).

Pop III stars are classified into sub-categories, Pop III.1 and Pop III.2. Pop III.1 stars are the very first generation of stars, and on the other hand, Pop III.2 stars are the stars which are not only made of the primordial gas, which is the same as Pop III.1, but also are formed under the influence of radiations from the first stars. According to recent theoretical researches using numerical simulations, Pop III.2 stars tend to be more massive than Pop III.1 stars because the molecular hydrogen, which is important coolant in Pop III star formation, is dissociated by radiation (e.g. Hirano et al., 2015).

3.4.2 Gas cooling process

The virialized dark matter objects have 178 times larger density compared with the background $\delta \sim 177$ (section 3.2.2). After virialization, the energy is conserved so that the dark matter halo no longer shrink. On the other hand, since the baryon interact with photons, they can release energy by radiation. Such cooled baryon can contract further. Therefore, considering the cooling efficiency of baryon gas leads to the condition for star formation in a dark matter halo.

The radiation generated by interaction of particles carries energy away, which works as cooling. For instance, the collisional excitation excites electrons to upper energy levels. Then, the electrons would de-excite by spontaneous emission. The emission pull out some energy from the gas cloud. If the gas is optically thin, the cooling rate per unit volume per unit time by particle i and particle j interaction can

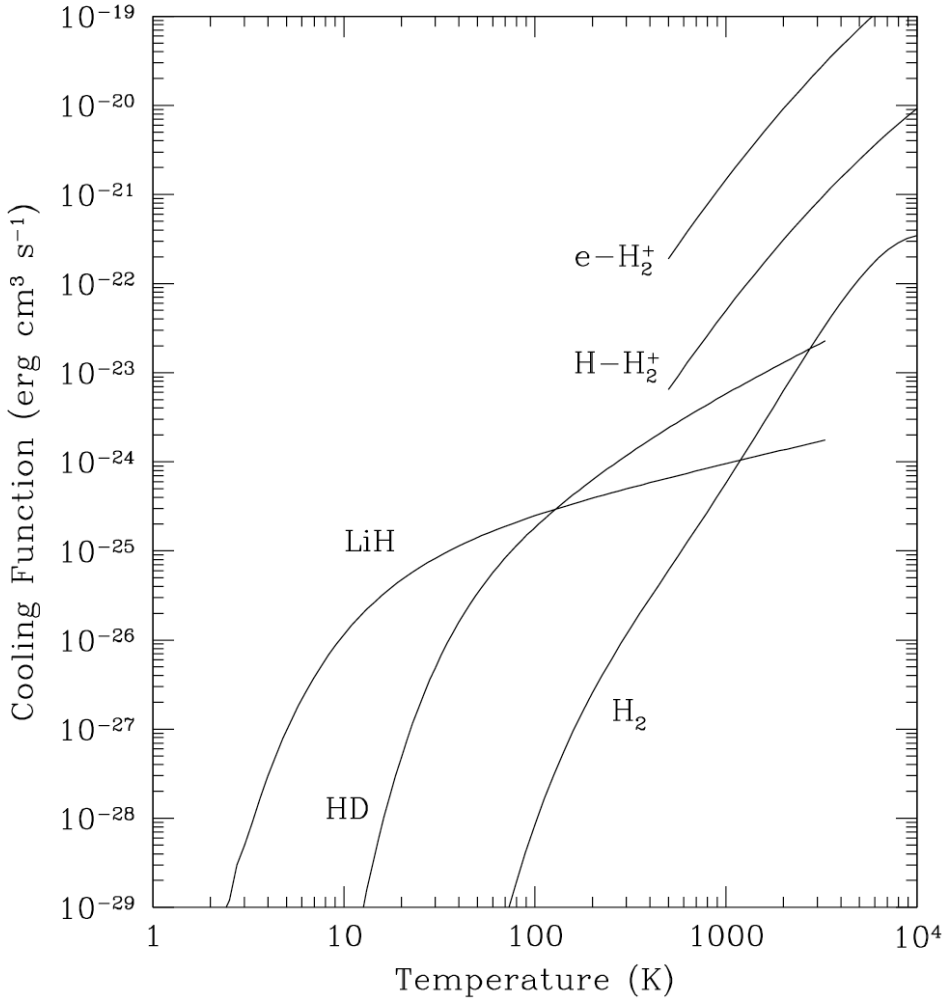

FIGURE 3.1: The cooling function of the primordial gas. The H_2 and HD (only if stars form from initially ionized gas) are important for Pop III star formation. The figure is taken from Galli and Palla, 1998.

be written as,

$$|\dot{E}_{\text{cool},ij}| = n_i n_j \Lambda_{ij}(T), \tag{3.87}$$

where n_i and n_j are the number density of particle i and j, $\Lambda_{ij}(T)$ is the cooling function depending on temperature. The cooling function of the primordial gas is shown in Figure 3.1. The values relating with H_2^+ or LiH are dominant in some range of temperature, but, the abundance of these molecules is much less than other particles so that these contributions can be neglected. The cooling by HD is dominant in some cases such that the gas is initially highly ionized. Pop III.1 stars are formed from the neutral gas, while, Pop III.2 stars formation can occur in such ionized gas clouds in which the HD cooling plays the important role.

When we write the gas kinetic energy as $E_{\rm k}$, the timescale of the cooling is

$$t_{\rm cool} = \frac{E_{\rm k}}{\sum_{ij} |\dot{E}_{{\rm cool},ij}|} \tag{3.88}$$

By comparing the cooling timescale with the free-fall timescale (equation 3.46), we can roughly estimate the condition of whether the gas can cool down enough to make star formation happen. Figure 3.2 shows the condition for star formation of a halo collapsed at $z_{\rm vir}$ with virial temperature of $T_{\rm vir}$.

If the cooling timescale is longer than the free-fall timescale, the gas cloud stops shrinking at the size when virial equilibrium is reached. Then, the cloud quasi-statically shrinks by the slow cooling process. This case corresponds the narrow area marked as $t_{\rm ff} < t_{\rm cool} < H^{-1}$. In this case, in smaller scales than the halo scale, structure formation cannot proceed, and thus, stars do not form in such slowly cooling gas cloud. On the other hand, if the cooling timescale is shorter than the free-fall timescale, the temperature decreases at sufficiently high rate, which is corresponding to the area marked as $t_{\rm ff} > t_{\rm cool}$. As a result, stars can form in the dark matter halo. If $H^{-1} < t_{\rm cool}$, the cooling takes longer than cosmic timescale so that the gas cannot cool, and certainly stars do not appear in such haloes.

3.4.3 Roles of Pop III stars in cosmic history and stellar properties

Pop III stars have several important roles in the thermal history and the structure formation history of the Universe. In this section, the key roles are concisely described especially focusing on the contribution to the cosmic reionization, the metal enrichment, and the candidate of the super massive black hole (SMBH) seed. Additionally, I introduce recent works investigating IMF of Pop III stars.

The first stars mainly form at redshift $20 - 30$ in MHs (e.g. Tegmark et al., 1997; Nishi and Susa, 1999; Abel, Bryan, and Norman, 2002; Bromm, Coppi, and Larson, 2002; Yoshida et al., 2003; Yoshida et al., 2006; Gao et al., 2007; O'Shea and Norman, 2007; Yoshida, Omukai, and Hernquist, 2008), which terminates the cosmic dark ages and tells the beginning of the epoch of reionization (EoR). The first stars are the first luminous object emitting ionizing photons after the cosmic recombination, apart from exotic sources. The IGM is almost fully neutral in the dark ages. The ionizing photons emitted from the first stars ionize the neutral IGM and create the ionized bubbles around thereof. Therefore, the first stars more or less contribute to the cosmic reionization (e.g. Alvarez, Bromm, and Shapiro, 2006; Johnson, Greif, and Bromm, 2007).

Pop III stars end their lives as energetic super nova (SN) expelling the heavy elements created in the nucleosynthesis in stars to the surrounding region. The heavier

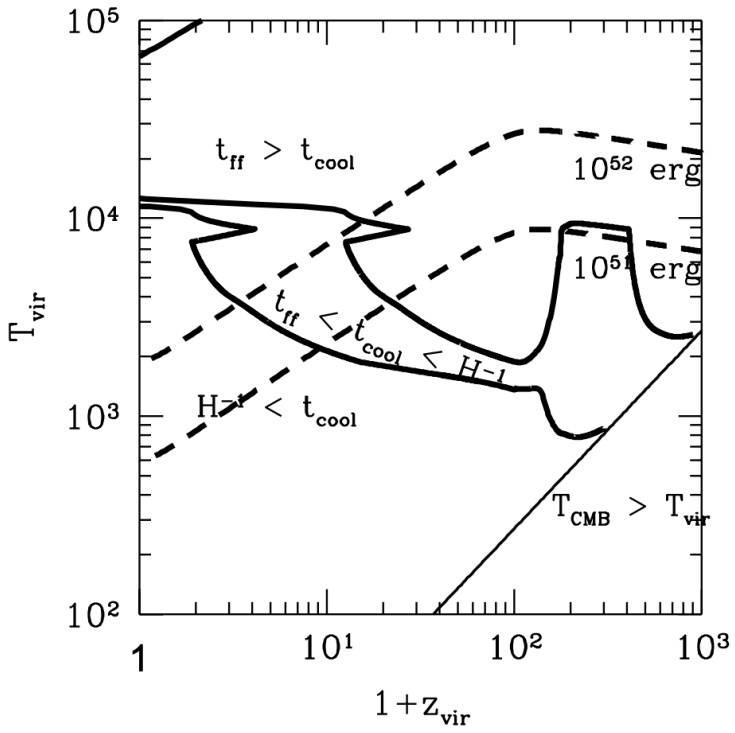

FIGURE 3.2: The cooling diagram in the redshift-virial temperature plane. The thick solid curves are derived from compering the cooling timescale, the free-fall timescale, and the Hubble timescale. The right bottom region marked by $T_{\rm CMB} > T_{\rm vir}$ is forbidden region where the virial temperature is higher than the CMB temperature so that the compton heating increases the gas temperature in haloes. The dashed lines mean the condition of whether gas cloud is destroyed by SN with energy of 10^{52} erg and 10^{51} erg, but, the SN effect is not in the scope of the thesis. The figure is taken from Nishi and Susa, 1999.

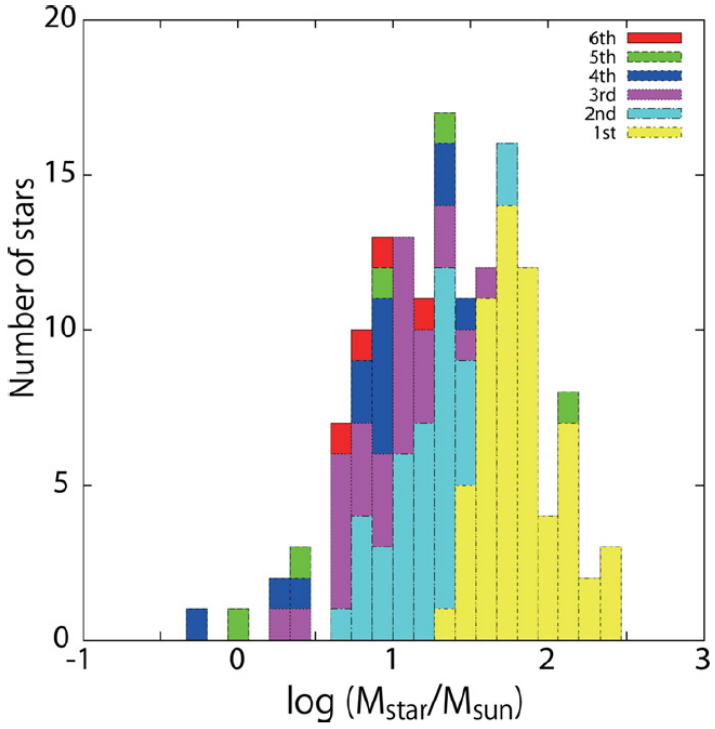

FIGURE 3.3: The initial mass function of Pop III stars. The figure is taken from Susa, Hasegawa, and Tominaga, 2014.

elements than lithium do not inhabit the primordial gas. The heavy elements scattered from the SN metal-enrich the circumference. From such metal enriched gas, the second generation of stars, that is pop II stars, form (e.g. Wise et al., 2012; Karlsson, Bromm, and Bland-Hawthorn, 2013).

The observations in the past ten years reveal that galaxies have a extremely massive black hole at the center with mass of $\sim 10^{6-9} M_\odot$ which depends on the size of galaxies (Venemans et al., 2013; Bañados et al., 2014; Wu et al., 2015). However, the seed of the super massive black holes (SMBHs) has not been clarified yet. Since Pop III stars tend to be massive and likely leave a BH after SN, Pop III stars are one of the candidates of SMBH's seed (Pelupessy, Di Matteo, and Ciardi, 2007; Li et al., 2007; Alvarez, Wise, and Abel, 2009).

How large impact Pop III stars have on the thermal history and the structure formation is strongly dependent on the stellar properties such as the initial mass function (IMF) and the star formation rate density (SFRD). For example, Pop III stars with masses between 25 $M_\odot$ - 140 $M_\odot$ and more massive than 260 $M_\odot$ leave a BH at the end of lifetime, but Pop III stars whose mass is not in the mass ranges do not (Heger and Woosley, 2002). As another example, the emissivity of ionizing photons are dependent on SFRD (and the escape fraction).

Since Pop III stars have not clearly been observed yet, the theoretical researches

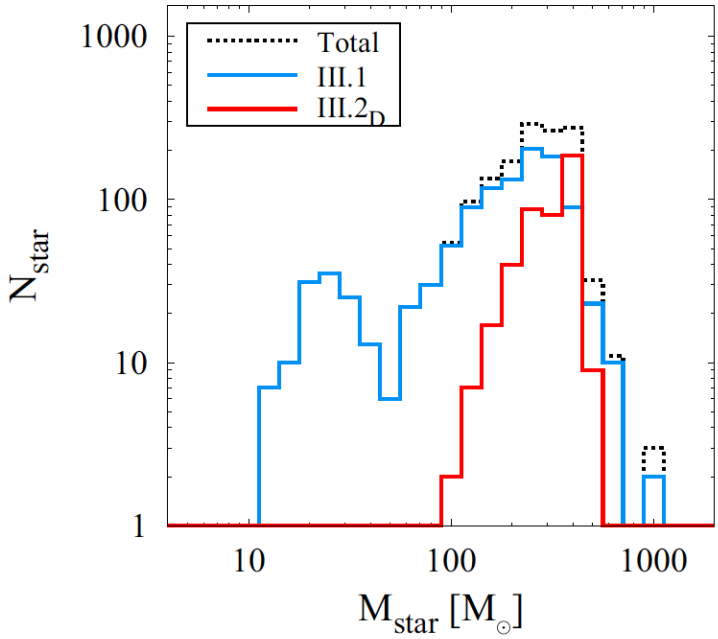

FIGURE 3.4: The initial mass function of Pop III stars. The figure is taken from Hirano et al., 2015.

have proceeded our understanding of the stellar properties. I show examples of theoretical studies investigating the IMF (Susa, Hasegawa, and Tominaga, 2014; Hirano et al., 2015) in Figure 3.3 and Figure 3.4. They take initial conditions from the cosmological simulations and then conduct local radiation hydrodynamics simulations to track star formation process. The resultant IMFs have different shapes: In Susa, Hasegawa, and Tominaga, 2014, the IMF has one peak around a few tens of solar mass, and on the other hand, the IMF in Hirano et al., 2015 has two peaks which around a few tens of solar mass and a few hundreds of solar mass.

One of the reasons why the two IMFs have different shape is the dimension of simulations: The simulations done by Hirano et al., 2015 is axisymmetrically two-dimensional, on the other hand, that of Susa, Hasegawa, and Tominaga, 2014 is three-dimensional. The protostellar disk, which is disk-like gaseous structure rotating around protostars, are known to fragment (e.g. Clark et al., 2011; Greif et al., 2011). The fragmented objects may end up as other stars, which means the multiple star formation in a MH. Three-dimensional simulation can follow the fragmentation, but while, the two-dimensional simulation cannot. One of the possible reasons why the IMF obtained by Susa, Hasegawa, and Tominaga, 2014 tend to be less massive than that by Hirano et al., 2015 is the dimensional difference. But, the two simulations are different in other methodological details, therefore, several reasons would complexly yield the difference.

3.4.4 Observational attempts for Pop III stars

Pop III stars play several key roles in the history of the Universe (see Section 3.4.3). Several observation projects are running or planning in order to observe Pop III stars. There are roughly two types of approaches. The one is direct observations of stars in high-redshift galaxies. The other is searching relic Pop III stars in the Milky Way galaxy.

First, the direct observations is explained. The effective temperature of Pop III stars is expected to be extremely high ($\sim 10^5$ K) due to the heaviness. Thus, Pop III galaxies, which are the galaxies mainly consisted of Pop III stars, emit abundant high-energy photons able to ionize HeII. Consequently, the spectral energy distribution (SED) of Pop III galaxy uniquely shows HeII recombination lines as shown in Figure 3.5. These HeII lines remain remarkable until the massive Pop III stars die. Because the typical lifetime of massive Pop III stars is about two million years, Pop III galaxy exhibits the HeII feature for 2 million years after the galaxy is born.

Some high-redshift galaxies displaying the HeII lines are reported, for example, the Cosmic Redshift 7 observed at $z \sim 6.6$ (Sobral et al., 2015). However, the evidence is not certainly clear. Although the observation of the first stars should be even more difficult, the next generation of observations such as the James Webb Space Telescope[1] and the Thirty Meter Telescope[2] aim to detect the light of the first stars.

Next, the seeking low metal stars in our galaxy is another approach. If Pop III stars are less massive than the solar mass, its lifetime is longer than the age of the Universe. Since mini-haloes merge to form large haloes, our galaxy would have the small Pop III stars. Indeed, the dozens of metal poor stars with $Z < 10^{-3.5}$ have already been found in the Galaxy. Simply judging from the metalicity, the stars are pop II stars. However, they are possibly Pop III star whose surface is contaminated by the accretion of metal-enriched gas.

In addition, the neutral hydrogen 21-cm line signal is recently getting more and more attention as a promising way to explore the high-redshift Universe including the era of Pop III star formation. The basics and recent observational progress are described in Chapter 4.

[1] https://www.jwst.nasa.gov/
[2] https://www.tmt.org/

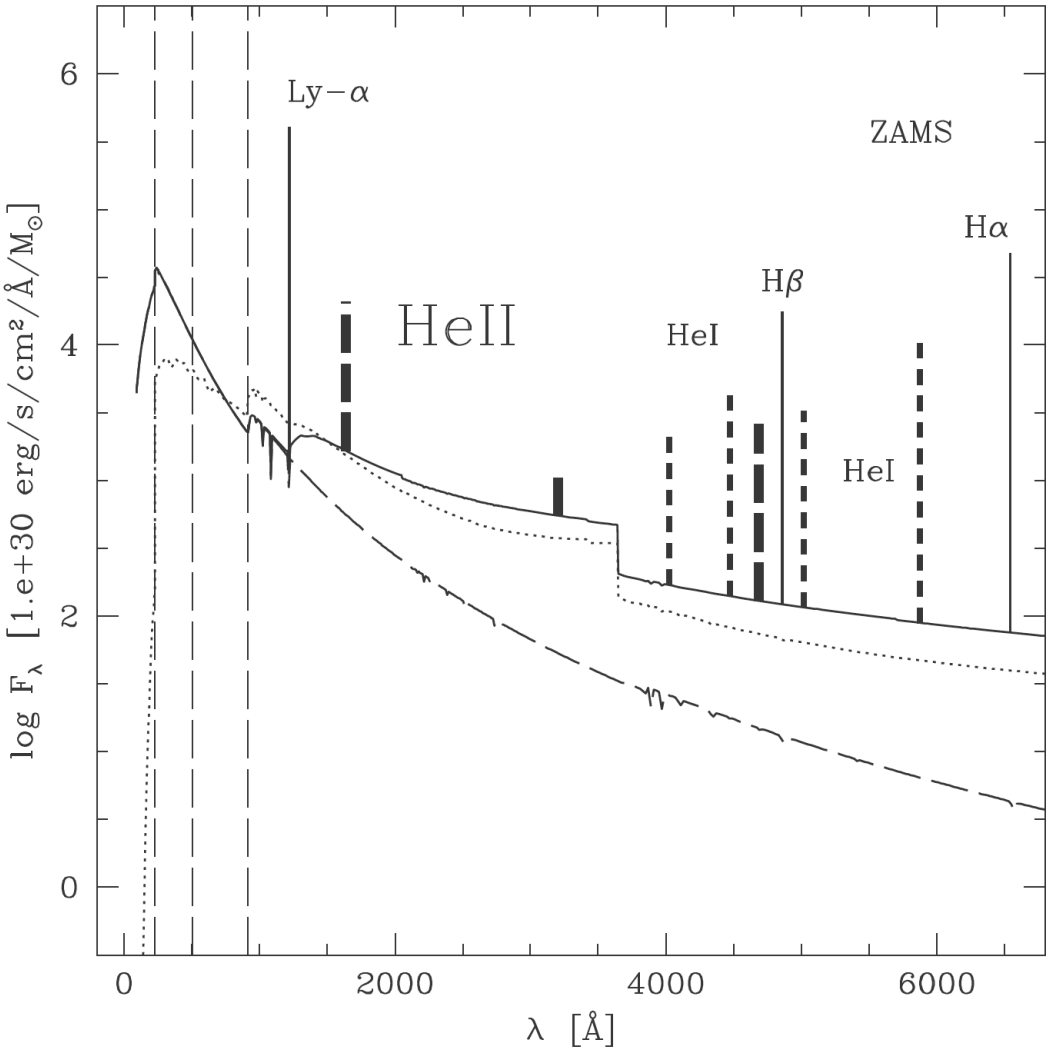

FIGURE 3.5: The spectral energy distribution of Pop III galaxy assuming the Salpeter IMF. The lower and upper limits of IMF are 1 and 500 $M_\odot$. The solid line is the emission taking into account the recombination lines of H and He from ionized gas around the galaxy. While, the dashed line is the pure stellar emission. To compare to pop II galaxy, the dotted line is the SED of pop II galaxy whose metalicity is $1/50 Z_\odot$ with Salpeter IMF whose lower and upper limit of mass are 1 and 150 $M_\odot$. The thick dashed lines on the spectrum are the recombination lines of HeII, and thin dashes lines are that of HeI. While the solid lines on the spectrum is that of H. The vertical lines correspond to energy needed to ionize H, He, and He^+. The figure is taken from Schaerer, 2002.

Chapter 4

The 21-cm line

In Section 3.4.4, I introduce some approaches to detect Pop III stars. Additionally, the neutral hydrogen 21-cm line signal is another powerful tool to investigate Pop III stars. In this section, I explain the basics of the 21-cm line, the statistics of the 21-cm brightness temperature which is the observable, and current status of 21-cm observations.

The neutral hydrogen has the hyperfine structure on its ground state. When the electron and the proton have the same direction of spin state, the energy level corresponds to the upper level. While, when the directions are anti-parallel, the energy level is the lower one. When the spin state flips from the parallel to the anti-parallel state, the photon whose wavelength is about 21 cm is emitted. The wavelength corresponds to the energy difference of the hyperfine structure.

The era when Pop III star formation dominates over that of other populations (the Pop III era) is the initial phase of the EoR, and there should be abundant fraction of neutral hydrogen. Therefore, the 21-cm line signal is a good tool to probe the Pop III era. The observed wavelength is stretched due to the Hubble expansion so that we observe $21 \times (1+z)$ cm radiation as the 21-cm line signal at redshift z. Consequently, by observing relevant range of frequency, we can tomographically scan the Universe.

4.1 21-cm brightness temperature

4.1.1 Radiative transfer

The radiative transfer equation adopted to a spectral line is

$$\frac{\mathrm{d}I_\nu}{\mathrm{d}l} = \frac{\phi(\nu)h\nu}{4\pi}[n_1 A_{10} - (n_0 B_{01} - n_1 B_{10}) I_\nu], \tag{4.1}$$

where, I_ν is the specific intensity with frequency ν, $\mathrm{d}l$ is a proper length element, n is the number density, 0 and 1 denote the lower and upper energy levels of the relevant transition. A_{10}, B_{01} and B_{10} are the Einstein coefficients of the spontaneous emission and collisional transitions where B_{ij} means that i is the initial state and j is the final state. ϕ is the line profile normalized as $\int \phi(\nu)\mathrm{d}\nu = 1$. The Einstein relations give us

the connection between the Einstein coefficients as follows

$$B_{10} = \frac{g_0}{g_1} B_{01}, \tag{4.2}$$

$$B_{10} = A_{10} \frac{c^2}{2h\nu^3}, \tag{4.3}$$

where g is the statistical degrees of freedom. In the case of 21-cm transition, $g_1/g_0 = 3$.

The spin temperature which corresponds to the excitation temperature for the spin flip transition is defined using the ratio of the number density of hydrogen whose electron is on each energy level,

$$\frac{n_1}{n_0} = \frac{g_1}{g_0} \exp\left(-\frac{T_*}{T_S}\right), \tag{4.4}$$

where T_* is the corresponding temperature of the spin flip transition $T_* \equiv E_{10}/k_B = 68$ mK. When the spin temperature is higher, more hydrogen atoms have its own electron on the upper energy level. If the spin temperature is much higher than the T_*, namely $T_S \gg T_*$, the electrons of three fourth of neutral hydrogen are asymptotically on the upper level, $n_1/n_0 \approx 3$.

It is convenient to use the brightness temperature $T_b(\nu)$ instead of the intensity I_ν. The brightness temperature is converted with $I_\nu = B_\nu(T_b)$ where $B_\nu(T)$ is the black body radiation with temperature T. As for the relevant range of frequency and temperature of 21-cm transition, the Rayleigh–Jeans limit is a good approximation.

With the Rayleigh-Jeans approximation and under the assumption of the thermal equilibrium, the equation of radiative transfer can be written as

$$T_b'(\nu) = T_S(1 - e^{-\tau_\nu}) + T_R'(\nu)e^{-\tau_\nu}, \tag{4.5}$$

where τ_ν is the optical depth, T_R' is the brightness temperature of the background radiation incident on a cloud, and the T_b' is the emerging brightness temperature from the cloud. To solve the equation, calculating the optical depth $\tau_\nu = \int \alpha \mathrm{d}l$ is needed, where α is the absorption coefficient which can be written as,

$$\alpha = \phi(\nu) \frac{h\nu}{4\pi} (n_0 B_{01} - n_1 B_{10}). \tag{4.6}$$

Since the condition $T_S \gg T_*$ is almost always satisfied in the relevant eras of the Universe, the ratio of number densities is $n_1/n_0 \approx 3$. Thus, the stimulated emission becomes non-negligible. The second term of equation (4.6) is the correction term due to the stimulated emission.

By re-writing the absorption coefficient (equation 4.6) with the Einstein relations

(equations 4.2 and 4.3), and using equation (4.4), the optical depth can be calculated by,

$$\tau_\nu = \int \mathrm{d}l \sigma_{01}(1 - e^{-T_*/T_\mathrm{S}})\phi(\nu) n_0 \tag{4.7}$$

$$\approx \sigma_{01} \left(\frac{h\nu}{k_\mathrm{B} T_\mathrm{S}}\right) n_0 \phi(\nu) l, \tag{4.8}$$

where $\sigma_{01} \equiv 3c^2 A_{10}/(8\pi\nu^2)$ and l is the length of the cloud in the line of sight. At the second line, we expand the exponential because the T_*/T_S is certainly small. Since the one fourth of neutral hydrogen have electron with lower hyperfine energy level, $n_0 \approx n_\mathrm{H} x_\mathrm{HI}/4$ where x_HI is the fraction of neutral hydrogen. Also using $\phi(\nu) \sim 1/(\Delta\nu)$ where the $\Delta\nu$ is calculated with the velocity dispersion of the cloud on the line of sight, the optical depth for the 21-cm emission is

$$\tau_{10} = \frac{3}{32\pi} \frac{hc^3 A_{10}}{k_\mathrm{B} T_\mathrm{S} \nu_{10}^2} \frac{x_\mathrm{HI} n_\mathrm{H}}{(1+z)(\mathrm{d}v_\parallel/\mathrm{d}r_\parallel)} \tag{4.9}$$

$$\approx 0.0092(1+\delta)(1+z)^{3/2} \frac{x_\mathrm{HI}}{T_\mathrm{S}} \left[\frac{H(z)/(1+z)}{\mathrm{d}v_\parallel/\mathrm{d}r_\parallel}\right], \tag{4.10}$$

where $\mathrm{d}v_\parallel/\mathrm{d}r_\parallel$ is the velocity gradient in the line of sight, and δ is overdensity. At the second line, we assume that the velocity gradient in the cloud is originated mainly from the Hubble expansion, and approximate the density evolution as the average IGM expanding uniformly due to the Hubble expansion.

In practice, the background radiation is the CMB radiation, $T_\mathrm{R}' = T_\mathrm{CMB}$. We observe the small deviation from the CMB temperature, so that we define the differential brightness temperature which is written as,

$$\delta T_\mathrm{b}(\nu) = \frac{T_\mathrm{S} - T_\mathrm{CMB}(z)}{1+z}(1 - e^{-\tau_{10}}) \tag{4.11}$$

$$\approx \frac{T_\mathrm{S} - T_\mathrm{CMB}(z)}{1+z}\tau_{10} \tag{4.12}$$

$$\approx 9 x_\mathrm{HI}(1+\delta)(1+z)^{1/2} \left[1 - \frac{T_\mathrm{CMB}(z)}{T_\mathrm{S}}\right] \left[\frac{H(z)/(1+z)}{\mathrm{d}v_\parallel/\mathrm{d}r_\parallel}\right] \ \mathrm{mK}. \tag{4.13}$$

At the second line, we expand the exponential because the optical depth is small enough. When the spin temperature of neutral gas is higher than the background CMB temperature $T_\mathrm{S} > T_\mathrm{CMB}$, the differential brightness temperature is positive which means the signal is emission against the CMB radiation. On the other hand, when the spin temperature is lower $T_\mathrm{S} < T_\mathrm{CMB}$, the δT_b is negative meaning that we observe the absorption signal. Also, when $T_\mathrm{S} = T_\mathrm{CMB}$, the differential brightness temperature is zero.

4.1.2 Spin temperature

The spin temperature is determined by the number densities of hydrogen whose electron is lower/upper energy level (equation 4.4). The three physical processes that cause the spin flip transition are important: (1) absorption and re-emission of the CMB photons, (2) collisions with gas particles, and (3) scattering with UV photons. Since the time scales of these processes are shorter than the cosmic time scale, the equilibrium of the three process determine the spin temperature,

$$n_1(C_{10} + P_{10} + A_{10} + B_{10}I_{\rm CMB}) = n_0(C_{01} + P_{01} + B_{01}I_{\rm CMB}), \tag{4.14}$$

where C_{10} and C_{01} are de-excitation and excitation rates due to collisions, P_{10} and P_{01} are de-excitation and excitation rates due to the scattering with UV photons. Re-writing equation (4.14) with the Rayleigh–Jeans approximation gives us,

$$T_{\rm S}^{-1} = \frac{T_{\rm CMB}^{-1} + x_{\rm c}T_{\rm gas}^{-1} + x_\alpha T_\alpha^{-1}}{1 + x_{\rm c} + x_\alpha}, \tag{4.15}$$

where $T_{\rm gas}$ is the gas kinetic temperature, T_α is the Lyα color temperature, $x_{\rm c}$ and x_α are the coupling coefficients for gas particle collisions and scattering with UV photons, respectively.

As for the collisional coupling, the coefficient for the collision of neutral hydrogen with particle i is

$$x_{\rm c}^i = \frac{C_{10}^i}{A_{10}}\frac{T_*}{T_{\rm CMB}} = \frac{n_i\kappa_{10}^i}{A_{10}}\frac{T_*}{T_{\rm CMB}}, \tag{4.16}$$

where κ_{10}^i the rate coefficient for the collision with particle i. Hydrogen atoms collide with other neutral hydrogen atoms, electrons, and protons. The collisions with deuterium and helium atoms are unimportant because their abundances are low. We sum up $x_{\rm c}^i$ for all species to obtain $x_{\rm c} = \sum_i x_{\rm c}^i$. Figure 4.1 shows the values of κ_{10}. The H-H collision almost always contributes most and determines the total coefficient $x_{\rm c}$ because the ionization fraction is small at Pop III era. In partially ionized gas, the H-e^- becomes important. The H-p^+ is main contributor only in the low temperature range.

The scattering with UV photons indirectly mix the hyperfine structure. I first describe the case of Lyman alpha photon as an example with Figure 4.2. Let us consider a neutral hydrogen atom whose electron is on the hyperfine upper level of the ground state. When the H absorb a Lyman alpha photon, the electron excite to the $n = 2$ level, where n is the quantum principle number. Then, the electron de-excites re-emitting a photon whose energy is that of Lyman alpha. At this point, the electron can de-excite to the both upper and lower levels. If the electron drops on the lower level, the spin flip occurs overall by absorbing and re-emitting Lyman alpha

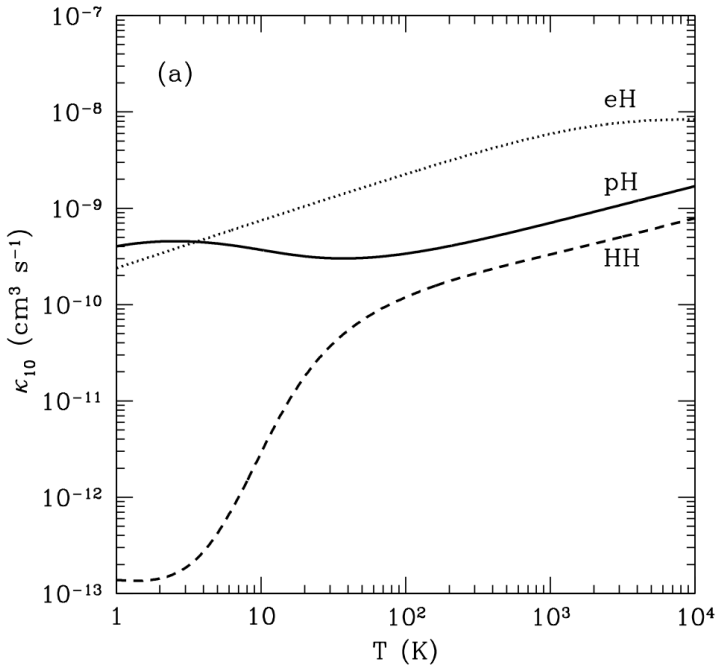

FIGURE 4.1: The rate coefficients of de-excitation for collisions of neutral hydrogen with neutral hydrogen (H-H), electrons (H-e^-), and proton (H-p^+). The figure is taken from Furlanetto and Oh, 2006.

photon. This process is the scattering with UV photons or so-called the Wouthuysen-Field effect (WF effect).

Other Lyman series photons contribute the 21-cm transition as well. For example, when hydrogen absorb the Lyman-γ, the electron climbs the energy potential to $n = 4$ energy level. Then, the electron can de-excite to the level with $n = 3$, and then to $n = 2$. Finally the electron de-excite to the ground state, possibly changing the initial hyperfine state. The cascade process increases the Lyman alpha coupling x_α. However, note that only Lyman-β does not contribute to the WF effect because of the electric dipole selection rules.

The coupling strength of the WF effect depends on the scattering rate of Lyman alpha photons P_α (the rate at which the gas is scattered with Lyman alpha photons per atom),

$$x_\alpha = \frac{4P_\alpha}{27A_{10}}\frac{T_*}{T_{\rm CMB}} \tag{4.17}$$

P_α is calculated by

$$P_\alpha = 4\pi\sigma_0 \int {\rm d}\nu J_\nu \phi_\alpha(\nu), \tag{4.18}$$

where $\sigma_0 \equiv (\pi e^2/m_e c) f_\alpha$ with the oscillator strength of the Lyman α transition $f_\alpha = 0.4162$, J_ν is the angle-averaged specific intensity, and $\phi_\alpha(\nu)$ is the line profile of Lyman α which is known to be the Voigt profile.

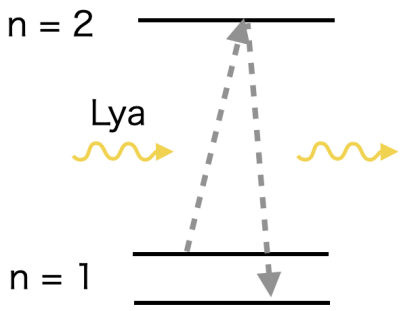

FIGURE 4.2: The figure illustrates how the absorption and re-emission of Lyman alpha photons contribute the 21-cm spin flip transition. The lines are the energy levels of electron with quantum principle number n.

The practical methods to calculate the coefficients x_c and x_α in simulations are introduced in Chapter 5.

4.2 21-cm statistics

Since the theory predicts only statistical properties of the 21-cm signals, I here introduce the 21-cm global signal which is the all-sky-averaged value and the 21-cm power spectrum.

4.2.1 The global signal

The 21-cm global signal is the averaged value of 21-cm brightness temperature over the sky. It is also called the monopole of the brightness temperature. Since different frequencies correspond to different redshifts, we can investigate the cosmic history from the global signal.

Figure 4.3 shows the global signal as a function of redshift (or frequency) and the corresponding evolutions of temperature and ionization degree. The black lines are the results from the standard model. Around $z \sim 200$, which is out of the redshift range of the figure but worth mentioning, the baryon gets decoupled with CMB photons. Thus, the redshift evolution of gas kinetic temperature changes from $T_k \propto (1+z)$ to $T_k \propto (1+z)^2$ which corresponds to the adiabatic cooling. As a result, the gas temperature cools faster than the CMB temperature making the difference between T_k and T_{CMB}. At that time, the Universe is so dense that the collisional coupling effectively couples the spin temperature with the gas temperature $T_S \sim T_k$. Therefore, the absorption signal emerges.

Until $z \sim 40$, the absorption signal becomes weak as the Universe expands and the IGM is diluted meaning that the gas particle collisions becomes ineffective for

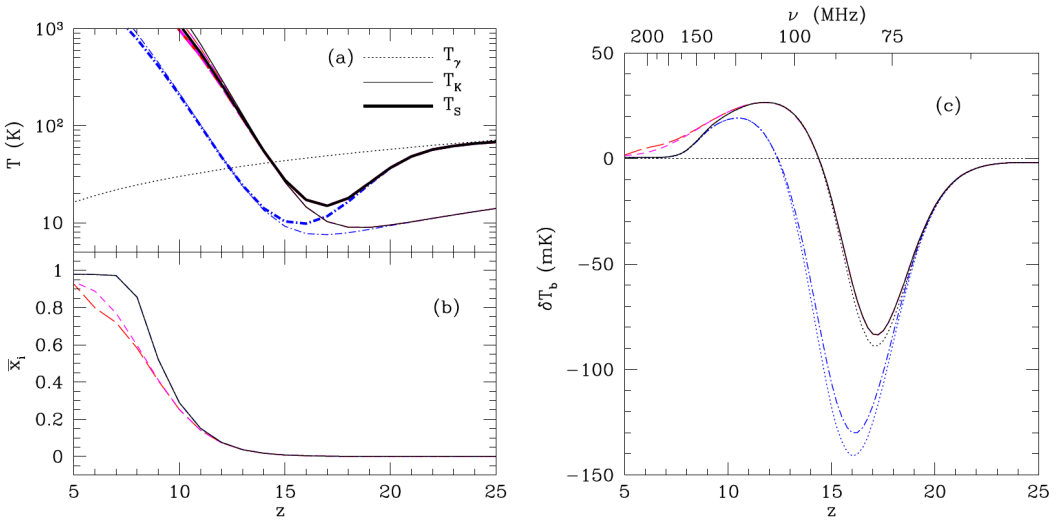

FIGURE 4.3: The histories of the 21-cm global signal and the relevant physical quantities. The black solid curves are the fiducial case, the blue curves are from model with less effective X-ray heating, and the long-dashed curves are from the model with strong photoheating feedback. The panel (a) shows the evolutions of the CMB temperature, the gas kinetic temperature, and the spin temperature. The panel (b) shows the ionization fraction as a function of redshift. The panel (c) shows the history of the 21-cm global signal as a function of redshift or frequency. This figure is taken from Furlanetto and Oh, 2006.

the coupling. Then the spin temperature gets closer to the CMB temperature. Thus, the differential brightness temperature is nearly zero from $z \sim 40$.

Around $z \sim 20 - 30$, the first generation of stars or the first stars form in the Universe and start emitting photons including Lyman series photons. The scattering of the UV photons increases the coupling coefficient x_α due to the WF effect. Thus, the spin temperature again gets decoupled from the CMB temperature, and approaches the colder gas temperature so that the strong absorption signal appears.

Then, around $z \sim 17$, the gas heating become sufficient to increase the gas temperature. In the standard model, the X-ray heating is considered. The possible sources of the X-rays are, for example, the high mass X-ray binaries, the photons which obtain energy by inverse Compton scattering with high-energy electrons accelerated in supernova, and any exotic sources like primordial black holes. As a result of the X-ray heating, the gas temperature increases beyond the CMB temperature, showing the emission signal.

Re-ionization starts affecting the global signal around $z \sim 10$. Since the fraction of neutral hydrogen decreases as the re-ionization proceeds, the emission signal becomes weaker and finally becomes nearly zero around $z \sim 7$.

The redshift of each epoch such as when the Lyman alpha coupling gets efficient and when X-ray heating becomes efficient strongly depends on the models. The astronomical uncertainties in high-redshift Universe is fairly large. Therefore, theoretical works to investigate the 21-cm signal should consider a wide range of parameters, and observations are also needed to constrain the theoretical models.

4.2.2 Power spectrum

The 21-cm global signal is the sky-averaged value of the 21-cm brightness temperature, as seen in the previous section. On the other hand, the spacial inhomogeneity of the signal has richer information than the global signal. The 21-cm power spectrum is the two-point statistics and reflects the statistical property of the inhomogeneity.

Let us define the fluctuation of the 21-cm brightness temperature as follows

$$\delta_{21}(\mathbf{x}, z) \equiv \frac{\delta T_{\rm b}(\mathbf{x}, z) - \overline{\delta T_{\rm b}}(z)}{\overline{\delta T_{\rm b}}(z)}, \tag{4.19}$$

where $\overline{\delta T_{\rm b}}(z)$ is the spacial average of the brightness temperature at redshift z which corresponds to the 21-cm global signal. The Fourier transformation of the two-point correlation of the 21-cm fluctuation is the 21-cm power spectrum $P_{21}(k)$,

$$\langle \tilde{\delta}_{21}(\mathbf{k}_1)\tilde{\delta}_{21}(\mathbf{k}_2)\rangle = (2\pi)^3 \delta_{\rm D}(\mathbf{k}_1 - \mathbf{k}_2) P_{21}(\mathbf{k}_1), \tag{4.20}$$

where $\tilde{\delta}_{21}(\mathbf{k})$ is the Fourier transformation of δ_{21} with the wave number vector $\mathbf{k}$, $\delta_{\rm D}$ is the Dirac delta function. Under the cosmological principle, we can convert the $P_{21}(\mathbf{k})$ to spherically-averaged power spectrum $P_{21}(k)$ with the norm of wave number vector k. The power spectrum whose unit is mK^2 is often used,

$$\Delta^2_{21}(k) = \frac{k^3}{2\pi^2} P_{21}(k) \langle \delta T_{\rm b}\rangle^2 \ [\mathrm{mK}]^2 \tag{4.21}$$

By observing the 21-cm power spectrum, we can obtain information on the history of the Universe. The results of a theoretical simulations are shown in Figure 4.4 and Figure 4.5 as examples.

At $z \sim 30$, the absorption signal is seen only at high-density regions because Lyman alpha coupling is prominent at denser regions due to more advanced structure formation than lower regions. Thus, the brightness temperature at the low-density regions is nearly zero. The inhomogeneity of the signal at this epoch is sourced by the Lyman alpha coupling.

Then, around $z \sim 21$, the structure formation in the Universe proceeds and the intensity of Lyman series photons become sufficient enough to couple the spin temperature with the gas temperature $T_{\rm S} \sim T_{\rm gas}$. At high-density regions, the gas is

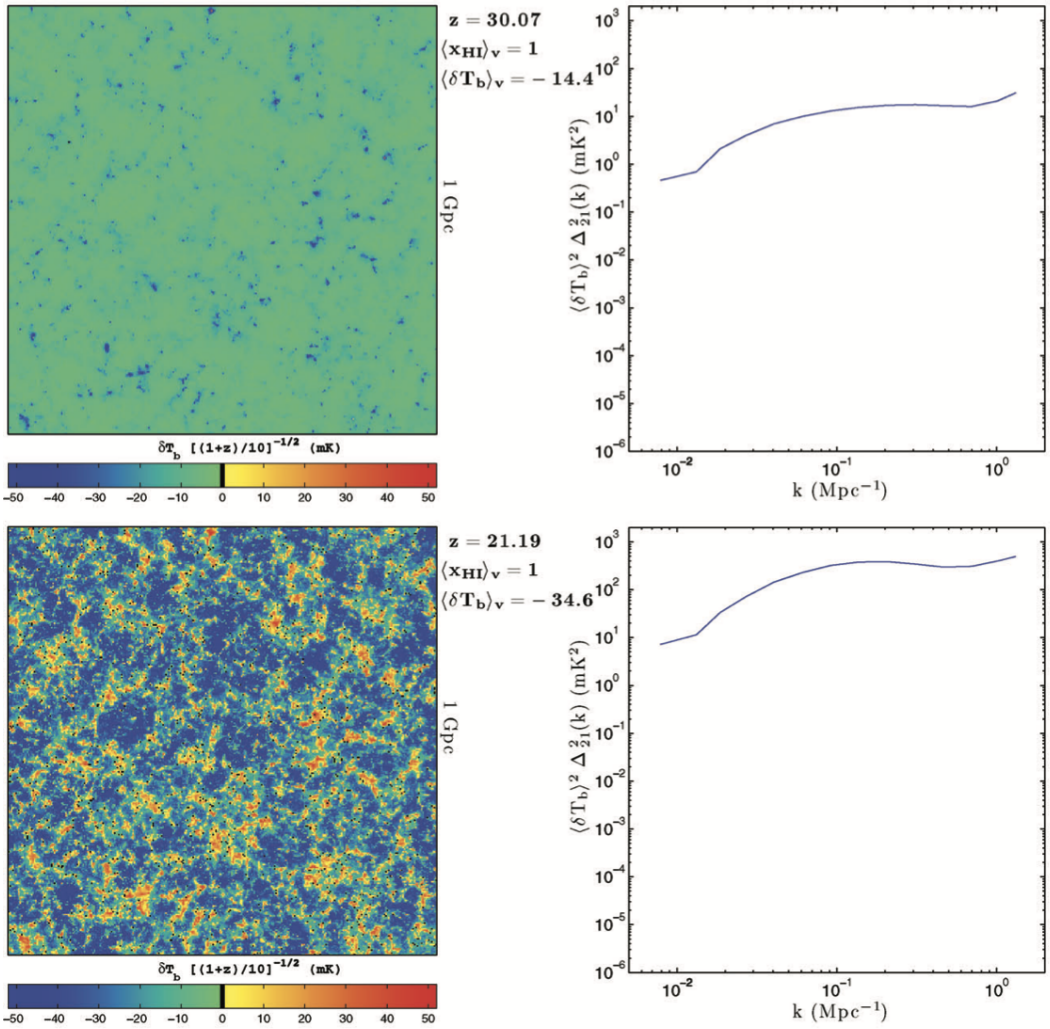

FIGURE 4.4: This figure shows the two-dimensional slice of three-dimensional 21-cm brightness temperature distribution calculated with the 21cmFAST which is publicly-opened semi-numerical simulation. The spherically-averaged three-dimensional power spectrum of the 21-cm signal is also displayed. When the redshift is $z \sim 30$ corresponds to the epoch before the Lyman alpha coupling dominates the most part of the Universe. While when the redshift is $z \sim 21$ is corresponding to the epoch when the WF effect strongly couple the spin temperature with the gas kinetic temperature almost everywhere in the Universe. This figure is taken from Mesinger, Furlanetto, and Cen, 2011.

heated above the CMB temperature mainly by X-rays, as a result, the brightness temperature is positive. While, at the low-density regions, the gas temperature is not increased yet, showing absorption signal. At this epoch, the power is dozens times larger than that at $z \sim 30$.

The gas heating proceeds as time passes and the gas temperature becomes much higher than the CMB temperature ($T_S \sim T_{gas} \gg T_{CMB}$) until around $z \sim 18$. The map of 21-cm brightness temperature and its power spectrum are shown in Figure 4.5. At this redshift, the neutral fraction is nearly one, that is, the cosmic reionization is still at the initial phase. Thus, the brightness temperature can be approximated by $\delta T_b \approx 9(1+\delta)(1+z)^{1/2}$ (c.f. equation 4.11). Namely, the signal fluctuates sourced by matter fluctuation. Thus, the observation of 21-cm signal at this epoch is important not only for astronomy but also for cosmology.

Then, around at $z = 10$, the cosmic reionization proceeds enough to affect the 21-cm signal. The ionized region is created mainly by UV photons emitted from stars. The mean free path of UV photons is fairly short, and therefore, the ionized region is nearly spherical centered at high-density regions. Such spherical ionized regions are often called ionized HII bubbles or simply bubbles. In the bubbles, almost no neutral hydrogen exist, thus, the brightness temperature is nearly zero. This highly inhomogeneous distribution of ionization degree boosts the power.

The redshift of each epoch is strongly dependent on the model parameters. For example, the ionization efficiency parameter which determines how efficiently stars ionize the IGM. Thus, the redshifts above are only examples of a specific model. Conversely, by estimating each epoch by observations, we can constrain the theoretical models. Therefore, one of what we should do is definitely to construct theoretical models of 21-cm signals precisely for forthcoming 21-cm observations such as the Square Kilometre Array.

4.3 21-cm line observations

Until the previous section, the theoretical framework of the 21-cm signal and some statistical signals such as the global signal and the power spectrum are described. In this section, I briefly introduce some current 21-cm observations and forthcoming future observations, focusing on the 21-cm global signal and the power spectrum.

As for the 21-cm global signal, the collaboration of the Experiment to Detect the Global EoR Signature (EDGES) has first reported the detection (Figure 4.6). They claim that the absorption trough at redshift around 17 which corresponds to the absorption era expected by theory when the Lyman alpha coupling effectively couple the spin temperature with the colder gas kinetic temperature than the CMB temperature.

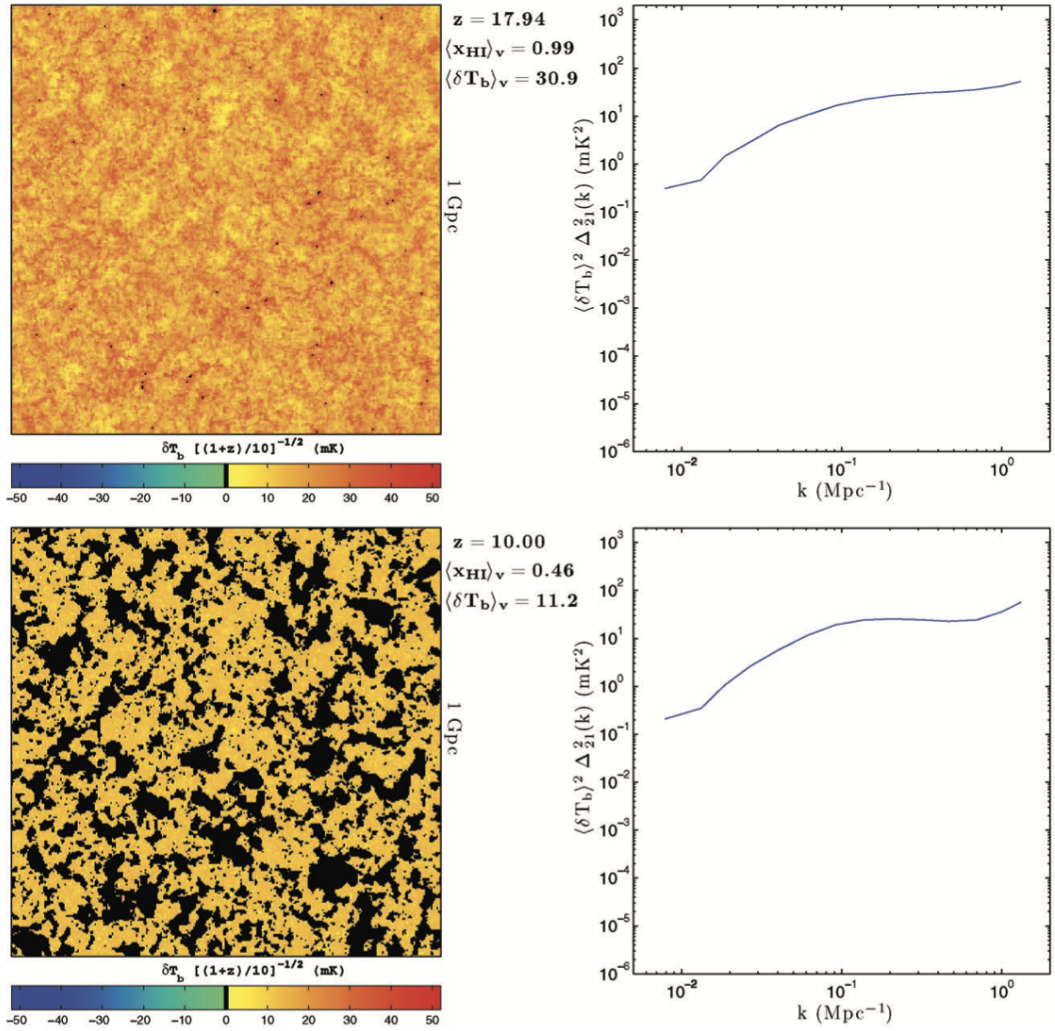

FIGURE 4.5: This figure is same as Figure 4.4, but at lower redshift when gas heating make the brightness temperature positive almost everywhere, and when the reionization is at its middle point. This figure is taken from Mesinger, Furlanetto, and Cen, 2011.

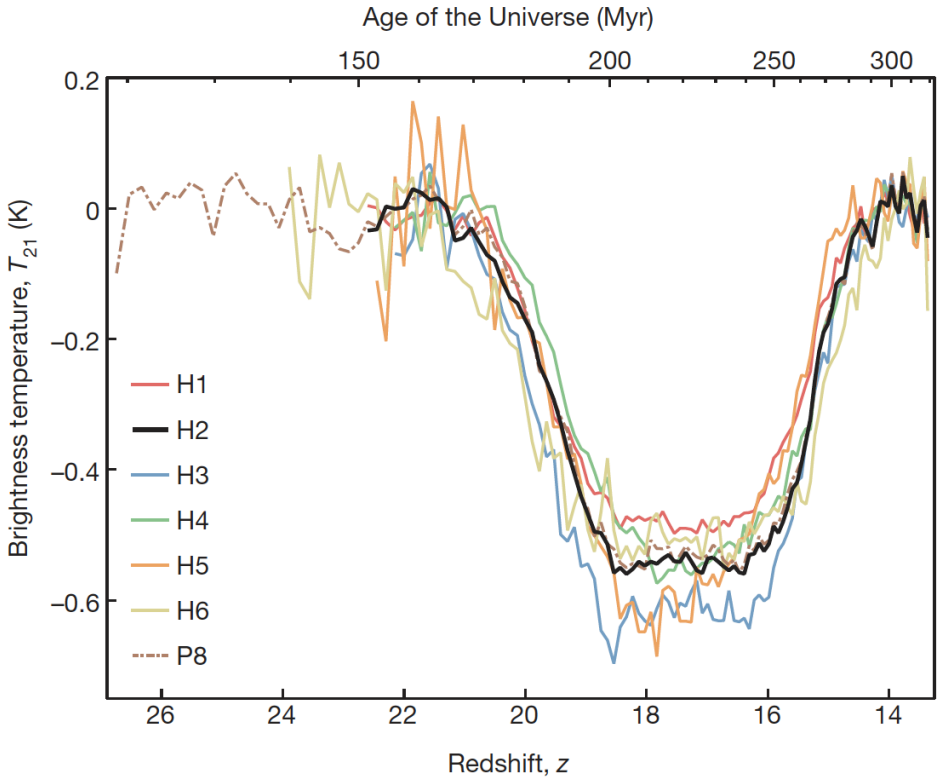

FIGURE 4.6: The global signal detected by the EDGES observation. The absorption trough around redshift 17 corresponds to the era when the Lyman series photons couple the spin temperature with the cold gas temperature through the WF effect. The absorption ($\sim$ 500 mK) is much deeper than standard theoretical models which is less than $\sim$ 350 mK. This figure is taken from Bowman et al., 2018.

However, the amplitude of the absorption $\sim$ 500 mK is much larger than that predicted by the standard model and even the case with tight coupling limit and no-heating limit. The baryon decouples from the CMB radiation at $z \sim 200$ and the gas temperature begins to decrease adiabatically ($T_{\rm gas} \propto (1+z)^2$). The CMB temperature is 2.7 K as of today, and thus, $T_{\rm CMB}(z = 200) = 56.7$ K because $T_{\rm CMB} \propto (1+z)$. On the other hand, if heating is not effective at redshift 20, the gas temperature is $T_{\rm gas}(z = 20) = T_{\rm CMB}(z = 200) \times (1+20)^2/(1+200)^2 = 5.9$ K. Assuming the tight coupling ($T_{\rm S} = T_{\rm gas}$), the global signal is $\delta T_{\rm b,global}(z = 20) = -355$ mK.

Many researches try to explain the difference between the observed amplitude and the theoretical value. For example, the interaction between baryon and dark matter can additionally transfer the energy from gas to dark matter resulting in a colder gas temperature (Barkana, 2018). As another example, the enhancement of the diffuse radio background can explain the larger absorption amplitude (Feng and Holder, 2018). As of today the discussion over the EDGES result has not converged yet. We need not only more theoretical works to explore possibilities to explain the excess of the absorption but also further observations of the 21-cm global signal.

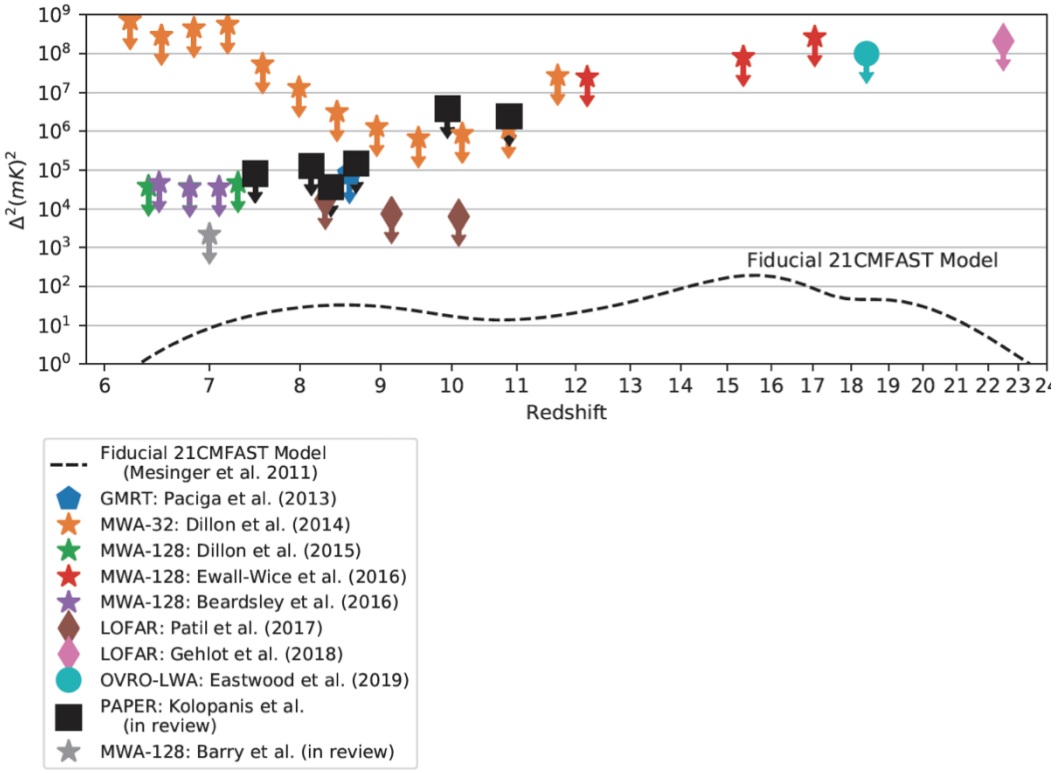

FIGURE 4.7: The upper limits imposed on the 21-cm power spectrum by current 21-cm observations: the GMRT, the MWA, the LOFAR, the OVRO-LWA, and the PAPER. The dashed line is the fiducial model calculated by the semi-numerical simulation code, 21cmFAST. Although the upper limits are not imposed on the same scale, but, they are plotted for easy by-eye comparison on one figure. The scales of these observations are distributed roughly around 0.1 Mpc^{-1}. This figure is taken from Parsons et al., 2019.

As for the 21-cm power spectrum, several observatories have already imposed upper limits around the scale of $k \sim 0.1$ Mpc^{-1} as shown in Figure 4.7. Any current observations have not reached the fiducial model, however, the forthcoming Square Kilometre Array (SKA) is planned to have enough sensitivity to detect the fiducial signal. The SKA will start the routine science observation in late 2020s.

The main difficulty of detecting the 21-cm signal is originated from the foreground. The amplitude of both extra-galactic and galactic foregrounds are order of Kelvin, on the other hand, the desired 21-cm signal from hydrogen at high redshift Universe has signal amplitude of only order of 1 - 10 mK. Therefore, foreground removal is extremely difficult.

Chapter 5

21-cm signal around population III stars

In this chapter, I summarize my study about the 21-cm signal structure around individual population III stars. This work focuses on the small scales, while, the other study of mine about large scale cosmological 21-cm signature is described in Chapter 6. This chapter is mainly composed of (Tanaka et al., 2018).

5.1 Introduction: Previous works and aim of the chapter

It is highly expected that the distribution of 21-cm line signal reflects the stellar mass because the ionization state and temperature of the gas around the pop III stars are determined by their luminosity. Chen and Miralda-Escudé (2008) computationally showed that a distinctive 21-cm signature appears around the pop III star. In the very vicinity of the pop III star, there is almost no 21-cm signal because the gas is highly ionized. At the ionization front (I-front), the gas is partially ionized and heated. The gas far from the I-front is colder than the Cosmic Microwave Background (CMB) temperature, and the gas temperature almost equals to the spin temperature owing to the coupling process through the Lyman-α (Lyα) pumping (Wouthuysen-Field effect; hereafter WF effect Wouthuysen, 1952; Field, 1958). Consequently, a 21-cm emitting region is surrounded by a 21-cm absorption region. Yajima and Li (2014) also studied the 21-cm signature around the pop III stars by conducting radiative transfer simulations, and estimated the detectability of the signal with the Square Kilometre Array (SKA). They concluded that detecting the signal is difficult even with the SKA.

However, these studies consider a static and uniform medium around the pop III stars and seem to miss some important points that affect the estimated 21-cm signature. For example, the dense gas distributed in a mini-halo, which they did not resolve, likely impacts the escape fraction of ionizing photons from the halo, thus the resultant size of the ionized region around the halo may change accordingly. In

order to estimate the escape fraction precisely, radiation hydrodynamics (RHD) simulations are required. Kitayama et al. (2004) performed RHD simulations to study the evolution of ionized regions around the pop III stars. They found that a halo hosting the pop III star is completely photo-ionized if an I-front changes from the D-type I-front to the R-type I-front[1] within the lifetime of the central star. Since the transition of the I-front occurs when the central region in a halo dynamically expands due to the thermal pressure enhanced by photo-heating, the type transition is sensitive to the amount of the gas in the halo, the potential of the halo, and the luminosity of the pop III star. Therefore the time evolution of the escape fraction strongly depends on the stellar and halo masses (Kitayama et al., 2004).

In addition to the 21-cm signal in the vicinity of an individual halo, the 21-cm global signal likely has some imprints reflecting the properties of the pop III stars (Chen and Miralda-Escudé, 2004; Furlanetto, 2006; Pritchard and Loeb, 2010; Mesinger, Ferrara, and Spiegel, 2013; Yajima and Khochfar, 2015), and recently attracts more attention due to the claim of detection of the signal (Bowman et al., 2018). However, previous studies based on simplified one-zone models and did not take into account the stellar-mass dependence of the global signal; the stellar-mass-dependent escape fraction mentioned above brings about the mass-dependent-heating rate of the intergalactic medium (IGM). Besides, even with a given cosmic star formation rate density (SFRD), the cosmic stellar mass density would depend on the stellar mass function of the pop III stars because their lifetime has a dependence on their mass.

To obtain reliable 21-cm signatures around the pop III stars, in this work, we conduct a series of spherically symmetric one-dimensional RHD simulations for individual pop III stars. In particular, we resolve the high-density region within a halo, by which we are able to appropriately consider the escaping process of ionizing photons from a halo and to evaluate time evolution of the radial profile of the 21-cm brightness temperature. Based on our simulation results, we explore the dependence of the 21-cm signal around the pop III stars on their stellar mass, halo mass, and their formation redshift. Furthermore, using our simulation results, we evaluate the detectability of the 21-cm signal around individual pop III stars and the dependence of the global 21-cm signal on properties of the pop III stars.

This chapter is organized as follows. In Section 5.2, we describe the methodology of our simulations. Then in Section 5.3, we show simulated spatial distributions of the 21-cm brightness temperature around individual pop III stars and evaluate the detectability of these signals with the SKA. In Section 5.4, we compute the global

[1] A D-type I-front slowly propagates in a high-density region. On the other hand, an R-type I front travels through a rarefied medium with supersonic speed.

21-cm signal by using our simulation results. Section 5.5 is devoted to discuss uncertainties in our results. Finally, we summarize this chapter in Section 5.6.

5.2 Mothod

5.2.1 Setup

We consider a single pop III star embedded in a mini-halo, and each run starts just after the ignition of the pop III star. Each simulation run is characterized by three parameters: the halo mass ($M_{\rm halo}$), the stellar mass ($M_{\rm star}$), and the formation redshift of the pop III star ($z_{\rm f}$). The halo mass is defined as the total mass of three components, i.e, the gaseous, stellar, and dark matter components, within the virial radius $r_{\rm vir}$:

$$M_{\rm halo} = M_{\rm star} + M_{\rm gas} + M_{\rm DM}, \tag{5.1}$$

$$M_{\rm DM} = \left(1 - \frac{\Omega_{\rm b}}{\Omega_{\rm m}}\right) M_{\rm halo}, \tag{5.2}$$

where $M_{\rm gas}$ and $M_{\rm DM}$ are respectively the gas mass and the dark matter mass. Once the halo mass is determined, the corresponding virial radius can be expressed as

$$r_{\rm vir} = 50.8 \left(\frac{M_{\rm halo}}{10^5 {\rm M}_\odot}\right)^{1/3} \left(\frac{1+z_{\rm f}}{20}\right)^{-1} \text{ physical pc}. \tag{5.3}$$

The initial gas density profile in a halo is assumed to obey a power-law distribution with the index of -2.2, which is indicated by previous studies (e.g., Omukai and Nishi, 1998; Susa, Hasegawa, and Tominaga, 2014; Hirano et al., 2015), and is serially connected to the uniform IGM density at a given redshift, $\rho_{\rm IGM}(z) = 8.6 \times 10^{-30} \Omega_{\rm b0} (1+z)^3$ g cm^{-3}. Hence the gas density distribution is given by

$$\rho_{\rm gas}(r) = \max\left\{\rho_{\rm IGM}(z_{\rm f}),\ \rho_{\rm gas,c}\left(\frac{r}{r_{\rm c}}\right)^{-2.2}\right\}, \tag{5.4}$$

where r is the distance from the centre of the halo, $\rho_{\rm gas,c}$ is the gas mass density of the innermost shell, and $r_{\rm c}$ is the core radius. We set $\rho_{\rm gas,c} = 1.67 \times 10^{-18}$ g cm^{-3} so that the central gas number density corresponds to 10^6 cm^{-3}, as in Kitayama et al. (2004). The core radius, $r_{\rm c}$, is determined to satisfy a condition of $4\pi \int_0^{r_{\rm vir}} \rho_{\rm gas}(r) r^2 {\rm d}r = M_{\rm gas}$. As for the dark matter density profile in a halo, we use the NFW profile (Navarro, Frenk, and White, 1995; Navarro, Frenk, and White, 1996; Navarro, Frenk, and White, 1997) given by

$$\rho_{\rm DM}(r) = \frac{\rho_{0,\rm DM}}{(r/r_{\rm s})(1+r/r_{\rm s})^2}, \tag{5.5}$$

where $r_{\rm s}$ is the scale radius defined as $r_{\rm s} = r_{\rm vir}/c_{\rm vir}$. We employ the concentration parameter, $c_{\rm vir}$, depending on redshift and halo mass shown by Bullock et al. (2001).

The amplitude of the profile is determined so that the total dark matter mass within $r_{\rm vir}$ corresponds to $M_{\rm DM}$.

The initial gas temperature is determined based on the following assumption; The gas adiabatically evolves after the decouple epoch $1+z_{\rm dec} \approx 137$ (Peebles, 1993), and the gas in high-density regions cool via molecular hydrogen cooling down to 500 K. Letting $T_{\rm IGM}(z_{\rm f})$ be the IGM temperature at $z_{\rm f}$, the temperature distribution is given by

$$T_{\rm gas}(r) = \min\left\{ T_{\rm IGM}(z_{\rm f}) \left(\frac{\rho_{\rm gas}(r)}{\rho_{\rm IGM}(z_{\rm f})} \right)^{2/3}, 500\ {\rm K} \right\}, \tag{5.6}$$

where $T_{\rm IGM}(z_{\rm f}) = T_{{\rm CMB},z_{\rm dec}} \left(\frac{1+z_{\rm f}}{1+z_{\rm dec}} \right)^2$, with being $T_{{\rm CMB},z_{\rm dec}} = 2.725 \times (1+z_{\rm dec})$ K at the decoupling epoch $z_{\rm dec}$. The index of $2/3$ is derived from the assumption that the gas is adiabatically heated up.

For the initial velocity, we only consider the Hubble velocity, $v_{\rm init}(r) = r/H(z_{\rm f})$. In reality the gas in a halo should still accretes toward the centre of the halo when the central star is born. However, such an initial infall velocity hardly changes the resultant structure of the 21-cm brightness temperature because it reverses due to the thermal pressure of ionized gas soon after the simulation starts.

Run Name	Dynamics	Halo gas	Redshift	Stellar Mass [$M_\odot$]	Halo Mass [$M_\odot$]	$t_{\rm life}$ [Myr]
Run-Ref	no	no	20	100	-	2.7
Run-z20S100H8e5	yes	yes	20	100	8×10^5	2.7
Run-z20S500H8e5	yes	yes	20	500	8×10^5	1.9
Run-z20S40H8e5	yes	yes	20	40	8×10^5	3.8
Run-z20S100H3e5	yes	yes	20	100	3×10^5	2.7
Run-z20S100H3e6	yes	yes	20	100	3×10^6	2.7
Run-z10S100H8e5	yes	yes	10	100	8×10^5	2.7
Run-z30S100H8e5	yes	yes	30	100	8×10^5	2.7

TABLE 5.1: Summary of representative runs performed in this chapter. Note that each run is named after the formation redshift, the stellar mass, and the halo mass employed in the run. Dynamics means whether each run includes gas dynamics or not, Halo gas indicates whether we consider halo gas whose density profile is explained in Section 5.2, redshift is the redshift at which the star is formed and begins to emit photons.

We conduct each simulation during the main-sequence lifetime of the pop III star, $t_{\rm life}$. The values of the effective temperature, $T_{\rm eff}$, the total number of ionizing photon emitted per second, $\dot{n}_{\rm ion}$, and $t_{\rm life}$, depending on the stellar mass $M_{\rm star}$, are taken from Schaerer (2002). For simplicity, the time evolution of the spectrum is not considered.

Since it is important to discuss the impact of resolving dense gas in a mini-halo, we also perform a reference run employing a static and uniform medium, which is assumed in previous studies (Chen and Miralda-Escudé, 2008; Yajima and Li, 2014). In this run, we assume 50 per cent of ionizing photons can escape from the halo. Table 5.1 summarizes representative runs that we perform in this study.

5.2.2 Simulation code

Based on the initial setup, the evolution of the gas in a halo is calculated with a modified version of an RHD simulation code used in previous studies (Kitayama et al., 2000; Kitayama et al., 2001; Kitayama et al., 2004; Hasegawa, Umemura, and Kitayama, 2009), which adopts the Lagrangian finite-difference scheme in a spherically symmetric geometry. The code enables us to solve hydrodynamics, non-equilibrium chemistry regarding primordial gas, and the radiative transfer of ionizing photons self-consistently.

The basic equations for a Lagrangian gas shell are

$$\frac{{\rm d}m}{{\rm d}r} = 4\pi r^2 \rho, \tag{5.7}$$

$$\frac{{\rm d}^2 r}{{\rm d}t^2} = -4\pi r^2 \frac{{\rm d}p}{{\rm d}m} - \frac{GM_{\rm tot}(r)}{r^2} + \frac{{\rm d}(rH)}{{\rm d}t}, \tag{5.8}$$

$$\frac{{\rm d}u}{{\rm d}t} = \frac{p}{\rho^2}\frac{{\rm d}\rho}{{\rm d}t} + \frac{\mathcal{H}-\mathcal{L}}{\rho}, \tag{5.9}$$

where r, m, ρ, p, u, $M_{\rm tot}(r)$, H, $\mathcal{H}$, and $\mathcal{L}$ are the distance from the central star, mass, mass density, pressure, specific internal energy, the total mass inside r of the shell, the Hubble parameter, the heating rate, and the cooling rate, respectively. Also, $m_{\rm p}$ and $k_{\rm B}$ respectively indicate the proton mass and the Boltzmann constant. The equation of state, $p = (2/3)\rho u = \rho k_{\rm B} T_{\rm gas}/(\mu m_{\rm p})$, is used to close the equations above, letting μ be the mean molecular weight. We treat the dark matter component as a static medium, by which we consider a dynamically relaxed (virialized) halo. As for the equation of motion, equation (5.8), we neglect the radiation force caused by ionizing photons but consider the Hubble expansion, because of the following reasons: (i) the impact of the radiation force on the gas in a halo is remarkable only at a very early phase after the central pop III star starts to shine (Kitayama et al., 2004), and (ii) the 21-cm signal around the pop III star is often extended up to 1 comoving

Mpc where the Hubble expansion is not negligible (e.g., Chen and Miralda-Escudé, 2008; Yajima and Li, 2014).

To solve the energy equation, equation (5.9), the heating rate, $\mathcal{H}$, and the cooling rate, $\mathcal{L}$, are obtained by solving the radiative transfer of ionizing photons and the chemical reactions regarding primordial gas. The chemical evolution follows

$$\frac{\mathrm{d}n_i}{\mathrm{d}t} = C_i(T_{\rm gas}, n_j) - D_i(T_{\rm gas}, n_j)n_i, \tag{5.10}$$

where n_i is the number density of the i-th species, C_i and D_i are the creation and destruction rates of the i-th species. In addition to chemical species of e, HI, HII, H^-, H_2, H_2^+, which are originally considered in Kitayama et al. (2004), we further consider HeI, HeII, and HeIII to calculate the distributions of HI and gas temperature accurately. The chemical reactions and cooling rates of He are taken from Fukugita and Kawasaki (1994). The thermal and chemical evolution are implicitly solved at the same time, assuming the initial abundance shown by Galli and Palla (1998).

When we solve the thermal and chemical evolution, the photo-heating and photo-ionization rates of i-th species (i=HI, HeI, and HeII) should be determined consistently, by solving the radiative transfer. Taking the weight of the absorption probability by the i-th species into account, we estimate the photo-ionization rates at each time step as (Susa, 2006; Yoshiura et al., 2017),

$$k_{i,\gamma}(r) = \frac{1}{V_{\rm shell}n}\int_{\nu_i}^{\infty}\mathrm{d}\nu\frac{n_i\sigma_i(\nu)}{\sum_j n_j\sigma_j(\nu)}\frac{L(\nu)}{h\nu}\mathrm{e}^{-\tau_\nu(r)}(1-\mathrm{e}^{\Delta\tau_\nu(r)}), \tag{5.11}$$

where $V_{\rm shell}$ is the volume of the shell, $\sigma_i(\nu)$ is the cross section of the i-th species, $L(\nu)$ is the luminosity of the central source, ν_i is the ionization threshold frequency of the i-th species, $\tau_\nu(r)$ is the optical depth between the central star and the shell,

$$\tau_\nu(r) = \sum_i \sigma_i(\nu)\int_0^r n_i\mathrm{d}r, \tag{5.12}$$

$\Delta\tau_\nu$ is the optical depth in the shell, and h is the Planck constant. In the radiative transfer calculation, we employ the on-the-spot approximation because the transfer of diffuse photons hardly affects the dynamics and the distribution of neural hydrogen (Hasegawa and Umemura, 2010).

Similar to the photo-ionization rates, the total photo-heating rate is given by

$$\mathcal{H}(r) = \frac{1}{V_{\rm shell}}\sum_i\int_{\nu_i}^{\infty}\mathrm{d}\nu\frac{n_i\sigma_i(\nu)}{\sum_j n_j\sigma_j(\nu)}\frac{L(\nu)}{h\nu}\mathrm{e}^{-\tau_\nu(r)} \times(1-\mathrm{e}^{\Delta\tau_\nu(r)})(h\nu-h\nu_i)(1-\eta_\alpha), \tag{5.13}$$

where, η_α is the fraction of the ejected electrons' energy which is not directly converted to the thermal energy but is used for exciting neutral hydrogen (see Section 5.2.3). We use the formula $\eta_\alpha(x_{\rm HII}) = 0.4766(1-x_{\rm HII}^{0.2735})^{1.5221}$, where $x_{\rm HII}$ is the ionization fraction of hydrogen (Shull and van Steenberg, 1985).

Since the relevant physical scales widely range from $\sim$ 0.1 pc (the core scale of a halo) to $\sim$ 100 kpc (the size of an ionized bubble), a uniform shell mass is inappropriate to solve the equation of motion. Therefore, we employ the shell mass that logarithmically increases toward outside,

$$\log m_n = \log m_{\rm min} + (n-1)\frac{\log m_{\rm max} - \log m_{\rm min}}{N_{\rm bin}}, \tag{5.14}$$

where, m_n is the mass of the n-th shell ($n = 1, 2, \cdots, N_{\rm bin}$), $N_{\rm bin}$ is the total number of the shells for which we adopt $N_{\rm bin} = 500$. With $m_{\rm min}$ being the central mass of a halo ($4\pi/3 r_{\rm c}^3 \rho_{\rm gas,c}$) and $m_{\rm max} = 10^{10}{\rm M}_\odot$, we can resolve inner $\sim$ 0.1 physical pc, and can trace the evolution of an ionization front up to $\sim$ 100 physical kpc.

5.2.3 Computing 21-cm signal

Based on results from the RHD simulations, we compute the 21-cm signal around the pop III star. The basics of 21-cm line signal are explained in Section 4.1, therefore, we here introduce the method to calculate the coupling coefficients (See equations 4.16 and 4.17) in detail.

We rewrite the equation that determines the 21-cm differential brightness temperature (equation 4.11), assuming the peculiar velocity of gas is negligible compared to the Hubble velocity

$$\begin{aligned}\delta T_{\rm b} =& \frac{T_{\rm S} - T_{\rm CMB}(z)}{1+z}(1 - e^{-\tau_{21}}) \\ \approx& 38.7 \frac{n_{\rm HI}}{\bar{n}_{\rm H}} \left(\frac{1+z}{20}\right)^{1/2} \frac{T_{\rm S} - T_{\rm CMB}(z)}{T_{\rm S}}\ {\rm mK},\end{aligned} \tag{5.15}$$

In order to determine C_{10}, we take into account collisions of neutral hydrogen with neutral hydrogen, protons and electrons:

$$C_{10} = n_{\rm HI}\kappa_{\rm HI}(T_{\rm gas}) + n_{\rm e}\kappa_{\rm e}(T_{\rm gas}) + n_{\rm p}\kappa_{\rm p}(T_{\rm gas}). \tag{5.16}$$

As for these collisional coupling coefficients, $\kappa_{\rm HI}$, $\kappa_{\rm e}$, and $\kappa_{\rm p}$, we use the fitting formulae given by Kuhlen, Madau, and Montgomery (2006), Liszt (2001), and Smith (1966). The quantities required for calculating the coefficients, i.e. $n_{\rm HI}$, $n_{\rm e}$, $n_{\rm p}$, and $T_{\rm gas}$, can be obtained from the RHD simulations.

We basically follow the method developed by Chen and Miralda-Escudé (2008) to calculate the coupling via the WF effect. The Lyα mean intensity at a position r is

required to obtain P_{10}, for which we consider two processes. One is the redshifted ultraviolet (UV) continuum photons emitted from the central star with frequencies between the Lyα frequency and the Lyman limit frequency: The resonance occurs when the redshifted photons coincide with particular energies of the Lyman series. In this case, the subsequent cascade process leads to the production of new Lyα photons. The number intensity of these "recycled" Lyα photons can be written by

$$J_{\rm c} = \sum_{n=2}^{n_{\rm max}} \Theta(\nu_{n+1} - \nu'_n) f_{\rm recycle}(n) \frac{N(\nu'_n)}{(4\pi)^2 r^2}, \tag{5.17}$$

where Θ is the Heaviside function to take into account horizon scales of Lyman series photons (Ahn et al., 2015), ν'_n is the frequency of emitted photons at the rest frame of the central star, which can redshift to the frequency corresponding the n-th excitation level, ν_n, when they arrive at r, $N(\nu)$ is the number luminosity per frequency of the central star, and $f_{\rm recycle}(n)$ is the fraction of Lyman series photons which turn out to be Lyα photons via cascades (Furlanetto and Oh, 2006). The typical optical depth of each shell in our simulations is much larger than unity. For that reason, we assume that emitted photons with frequencies of ν_n-ν_{n+1} are immediately absorbed when their frequencies becomes ν_n. Therefore, each Lyman series photon has its horizon scale, beyond which any absorptions do not happen. The summation of n should be stopped at some large $n_{\rm max}$ for which we set $n_{\rm max} = 30$ (Furlanetto and Oh, 2006).

The other process is excitations of neutral hydrogen by secondary electrons ejected via photo-ionization. Since we consider photons with hard spectra from the central stars, the ejected electrons have kinetic energies high enough to excite neutral hydrogen. The Lyα mean intensity produced by subsequent de-excitations is expressed as

$$J_{\rm i} = \frac{c\eta_\alpha \mathcal{H}}{4\pi H(z) h \nu_\alpha^2}. \tag{5.18}$$

By using $J_{\rm c}$ and $J_{\rm i}$, P_{10} is described as

$$P_{10} = \frac{4}{27} H(z) \tau_{\rm GP}(z) \frac{J_{\rm c} S_{\rm c} + J_{\rm i} S_{\rm i}}{\tilde{J}_0}. \tag{5.19}$$

Here $\tilde{J}_0$ is defined as $cn_{\rm H}/(4\pi\nu_\alpha)$. The Gunn-Peterson optical depth, $\tau_{\rm GP}$, is given by

$$\tau_{\rm GP} = \frac{\chi_\alpha \bar{n}_{\rm HI}(z) c}{H(z)\nu_\alpha}. \tag{5.20}$$

Here, $\chi_\alpha = (\pi e^2/m_e c) f_\alpha$ is the Lyα absorption cross section at the line centre , $f_\alpha = 0.4162$ is the oscillator strength of the Lyα transition, $\bar{n}_{\rm HI}$ is the average number density of the neutral hydrogen. In equation (5.19), $S_{\rm c}$ and $S_{\rm i}$ are the suppression factors originated from the fact that the shape of the radiation spectrum changes during

multiple scattering. We assume that $S_c = S_i$, and use the fitting formula given by Furlanetto and Pritchard (2006):

$$S_c = S_i \approx 1 - \frac{4\pi}{3\sqrt{3}\Gamma(2/3)}\alpha + \frac{8\pi}{3\sqrt{3}\Gamma(1/3)}\alpha^2 - \frac{4}{3}\alpha^3, \tag{5.21}$$

$$\alpha = 0.717 T_{\rm gas}^{-2/3} \left(\frac{\tau_{\rm GP}}{10^6}\right)^{1/3}, \tag{5.22}$$

in the wing approximation of the Voigt profile. Here, $\Gamma(x)$ is the Gamma function.

5.3 21-cm signature around the pop III star

5.3.1 Importance of resolving gas in a halo

As described in Section 5.1, considering gas dynamics in each halo is indispensable to precisely calculate the time-evolving escape fraction. Thus, our simulations take into account gas dynamics and resolve gas distribution in a mini-halo unlike previous studies (Chen and Miralda-Escudé, 2008; Yajima and Li, 2014). In this section, we investigate how the effects of resolving dense gas in a halo and gas dynamics impact the emerging radial distribution of δT_b. To do this, we compare Run-Ref, in which static and uniform gas density is assumed, and Run-z20S100H8e5, in which the RHD effect is considered (see Table 5.1). Figure 5.1 shows the radial profiles of the 21-cm brightness temperature at $t_{\rm age} = 0.5$, 1.5, 1.7, and 2.7 Myr, where the upper and lower panels correspond to the profiles obtained from Run-z20S100H8e5 and Run-Ref. Figure 5.2 shows the time evolution of physical quantities relevant to the brightness temperature in these runs.

In Run-Ref, a well-known characteristic feature, i.e. an emitting region surrounded by an absorption region, monotonically moves away from the central star as an I-front propagates. This characteristic feature is known to be caused by combination of partially ionized warm gas in the I-front and abundant Lyff photons, forcing the spin temperature to be coupled with the gas temperature, in front of the I-front (see the right panels in Figure 5.2).

Compared to Run-Ref, there are two remarkable features in Run-z20S100H8e5. One is the strong emission region at $r \sim 10^{-2}$ kpc, which disappears in a short timescale within 0.5 Myr. The other is the deep absorption feature outside the virial radius, which is almost steady until $t_{\rm age} = 1.5$ Myr and then decays with time. The strong emission region has not been calculated in previous studies because the halo was considered to be too small for observations. The amplitude of the high temperature in the strong emission region is proportional to the number density of neutral hydrogen (see Equation 5.15), therefore, if the halo has a denser core, the emission from the central region of the halo would be stronger. Note that Equation (5.15) is

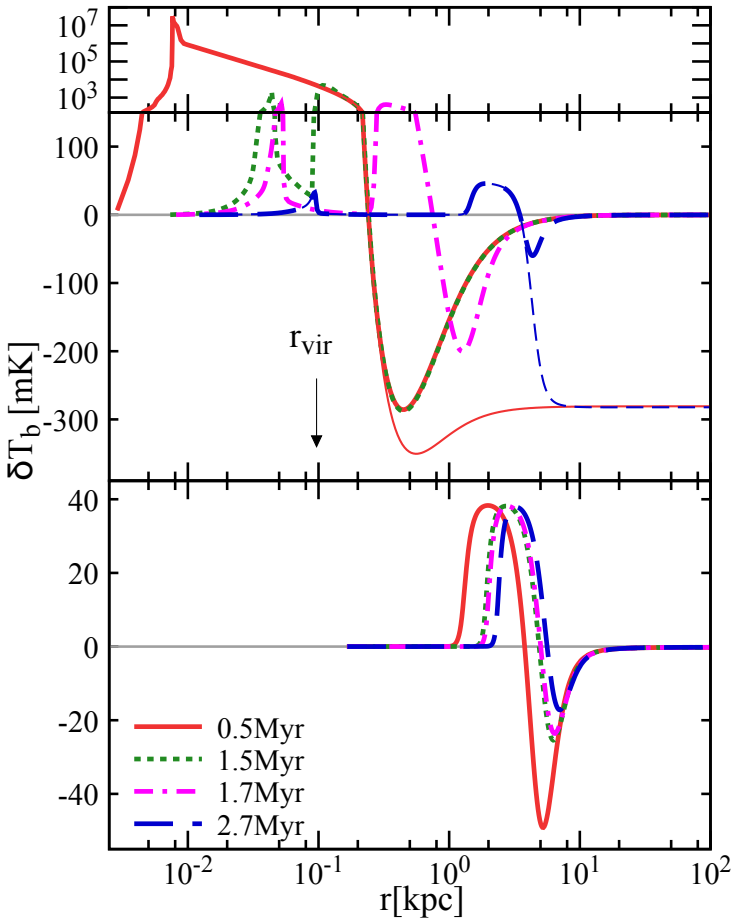

FIGURE 5.1: Radial profile of the differential brightness temperature as a function of the distance from the central star. The upper and lower panels respectively show the profiles in Run-z20S100H8e5 and Run-Ref. In these runs, the parameters are $M_{\rm star} = 100{\rm M}_\odot$, $z_{\rm f} = 20$, and $M_{\rm halo} = 8 \times 10^5{\rm M}_\odot$. The red solid, green dotted, magenta dot-dashed, and blue dashed curves represent the profiles at $t_{\rm age} =$ 0.5Myr, 1.5Myr, 1.7Myr, and 2.7Myr, respectively. The thin curves show $\delta T_{\rm b}(r)$ which is based on an assumption that the spin temperature is completely coupled with the gas temperature. The vertical arrow with $r_{\rm vir}$ indicates the virial radius.

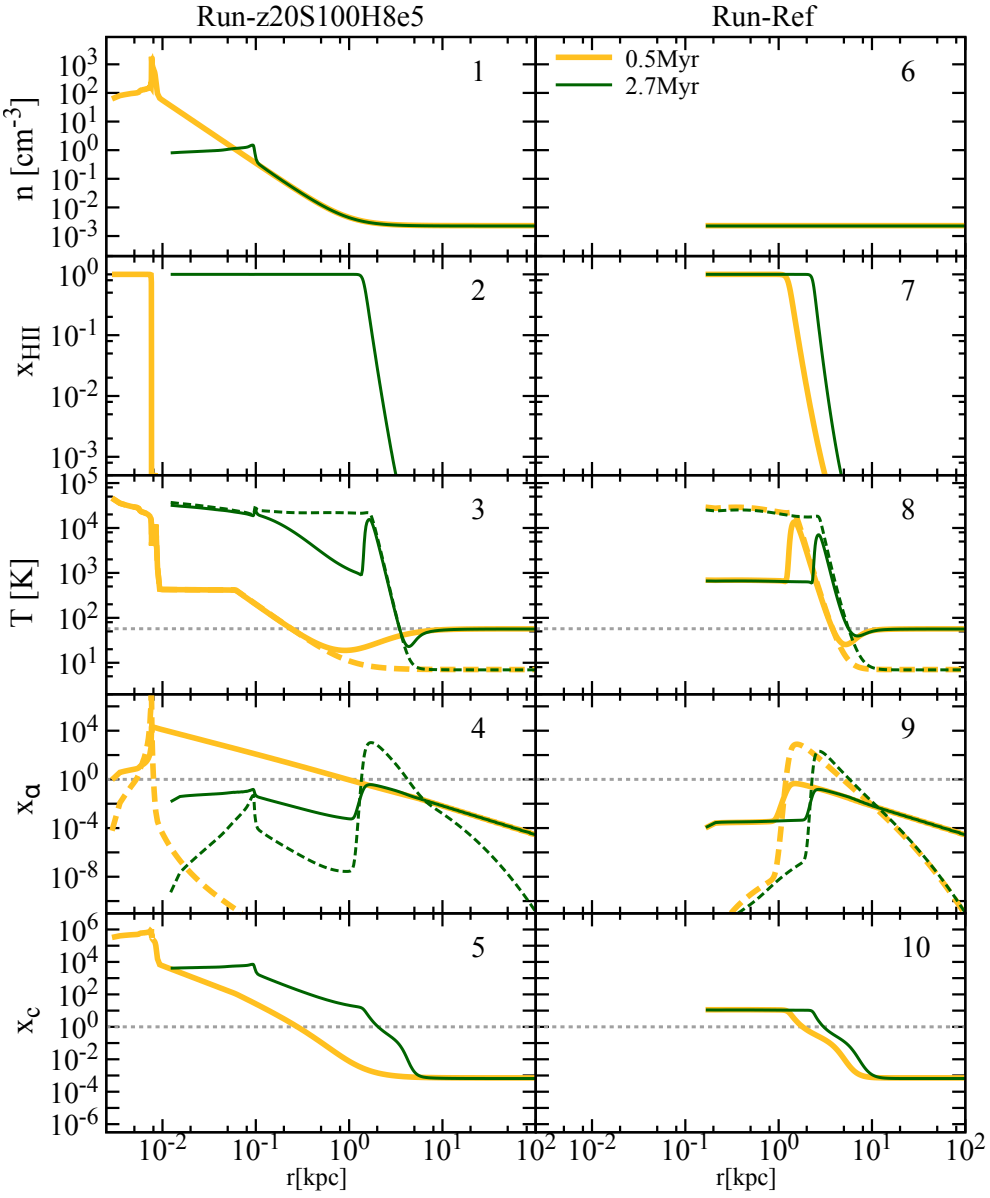

FIGURE 5.2: Radial profiles of physical quantities associated with the differential brightness temperature in Run-z20S100H8e5 (left column) and Run-Ref (right column) at $t_{\rm age} = 0.5$Myr (yellow thick curves) and $t_{\rm age} = 2.7$Myr (green thin curves). From top to bottom, each panel shows the radial profiles of the number density, ionized fraction of hydrogen, the spin and gas temperatures, the Lyα coupling coefficients originated in the continuum photons (solid) and the secondary excitation (dashed), and the collisional coupling coefficient. In Panel 3 and 8, the CMB temperature is shown by the horizontal dotted line, and the gas and spin temperatures are respectively represented by the solid and dashed curves. In Panel 4, 5, 9 and 10, the horizontal dashed line indicates unity above which the coupling processes effectively work to couple the spin temperature to the gas temperature.

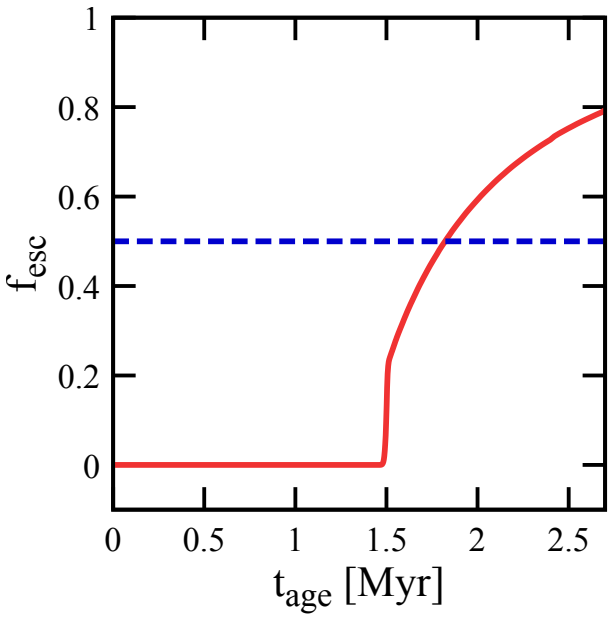

FIGURE 5.3: Time evolution of the escape fraction in Run-z20S100H8e5. The constant escape fraction of $f_{esc} = 0.5$, which is assumed in Run-Ref, is also shown by the horizontal dashed line.

not accurate for computing δT_b in haloes, because haloes are isolated from the cosmic expansion. With an appropriate treatment for 21-cm optical depth in haloes (e.g., equation (7) in Furlanetto and Loeb, 2002), the δT_b becomes smaller by about two orders of magnitude. Nevertheless, the overestimation does not affect our claims in later sections because the volume of the emission region is significantly small. Figure 5.2 reveals that the spike in the emitting region ($\delta T_b > 0$) is caused by a shock preceding the I-front (see Panel 1 of Figure 5.2). Although the brightness temperature at the spike is high at the very early phase, the spike rapidly disappears because the shock propagates outward quickly. On the other hand, the deep absorption feature comes from the gas residing in the outer rim of the halo where the gas is slightly overdense and colder than the CMB temperature. As shown by Kitayama et al. (2004), the ionized region is well confined until the I-front is converted from D-type to R-type (Panel 2 of Figure 5.2). Therefore photo-heating does not work at the outer rim of the halo, and the gas is kept as the cold state (Panel 3 of Figure 5.2). In contrast to the ionizing photons, UV continuum photons, which enable the spin temperature to be coupled with the gas temperature through the WF effect, can reach the outer edge of the halo (Panel 4 of Figure 5.2). Furthermore, the radial profile of $\delta T_b \propto n_{HI}\left(1 - \frac{T_{CMB}}{T_S}\right)$ has the local minimum (the thin solid curve in the upper panel of Figure 5.1) in the case that the spin temperature is completely coupled with the gas temperature ($T_S = T_{gas}$). The combination of the local minimum of $n_{HI}\left(1 - \frac{T_{CMB}}{T_S}\right)$ and the dilution of the Lyff flux results in the remarkable absorption

feature at the outer rim of the halo.

The rapid decay of the absorption feature starts when the ionizing photons escape from the halo. The escape fraction of ionizing photons can be calculated by

$$f_{\rm esc} = \frac{\int_{\nu_{\rm HI,L}}^{\infty} \frac{L(\nu)}{h\nu} {\rm e}^{-\tau_\nu(r_{\rm vir})} {\rm d}\nu}{\int_{\nu_{\rm HI,L}}^{\infty} \frac{L(\nu)}{h\nu} {\rm d}\nu}, \tag{5.23}$$

where $\nu_{\rm HI,L}$ is the Lyman limit frequency. Figure 5.3 shows the time evolution of the escape fraction of ionizing photons. The escape fraction sharply rises at $t_{\rm age} \sim 1.5$ Myr, when the absorption feature starts to decay. Hereafter, we call this characteristic time as $t_{\rm decay}$. As shown by Figure 5.3, the escape fraction in Run-z20S100H8e5 after $t_{\rm decay}$ is higher than that assumed in Run-Ref, i.e., $f_{\rm esc} = 0.5$. This is a reason why the I-front in Run-z20S100H8e5 almost catches up that in Run-Ref at $t_{\rm age} > t_{\rm decay}$ (e.g., $t_{\rm age} \sim 2.7$ Myr in Panel 2 and 7 of Figure 5.2). We note that the expansion of the ionized region due to hydrodynamics does not appear significantly because the recombination time is much shorter than the lifetime of the central star.

It is worth to mention that the dominant process coupling the spin temperature with the gas temperature differs between Run-Ref and Run-z20S100H8e5. Since the spin temperature deviates from the CMB temperature if the coupling coefficient (either $x_{\rm c}$ or x_α) is greater than unity, the size of a signal region is roughly determined by the position where a coupling coefficient becomes unity. As shown by Panel 5 of Figure 5.2, the collisional coupling process is important only in the high-density region, and is usually less efficient than Lyα coupling processes. Thus, we hereafter focus solely on x_α. In Run-Ref, the size of the signal region is determined by the secondary excitation process rather than redshifted UV continuum at any evolutionary phases (see Panel 9 of Figure 5.2), because the absorption region moves with the I-front where electrons are ejected by photo-ionization (Chen and Miralda-Escudé, 2008). On the other hand, in Run-z20S100H8e5, the process determining the size of the signal region differs according to dynamical evolution. Before $t_{\rm decay}$, the size is determined by the redshifted UV continuum photons emitted from the central star, as shown in Panel 4 of Figure 5.2. This is because the ionized region is well confined in the halo, so that the contribution from Lyα flux induced by the secondary electrons does not work at the outer edge of the absorption region and the radial size of the absorption region is smaller than that in Run-Ref which is calculated in the same manner as (Chen and Miralda-Escudé, 2008). After $t_{\rm decay}$, because the I-front is converted into R-type, the ionized region expands rapidly beyond the virial radius. Correspondingly, the Lyα photons associated with the secondary excitation start dominating the coupling process at the absorption region as in Run-Ref. However, the radial size of the absorption region is still smaller than that in Run-Ref because the propagation of the I-front is initially delayed due to the attenuation by

the halo gas.

The deep absorption region may be an attractive target for observations in the future, because the existence of such a deep absorption implies a mini-halo hosting the pop III star. Even if the profile is not resolved, the spatially smoothed signal within the resolution of a telescope is more or less influenced by the high amplitude as we discuss in Section 5.3.5 and Section 5.3.6. We also show that the decay time $t_{\rm decay}$ plays an important role on the detectability of the individual 21-cm signal, and is strongly dependent on the stellar mass, the halo mass, and the formation redshift in the following sections Section 5.3.2, Section 5.3.3, and Section 5.3.4.

5.3.2 Stellar mass dependence

Since unveiling the mass of the pop III stars is very important issue, we now investigate how the 21-cm signal around the pop III star depends on the stellar mass.

Figure 5.4 shows the time evolution of the radial profiles of the brightness temperature in Run-z20S500H8e5, Run-z20S100H8e5, and Run-z20S40H8e5, in which stellar masses are respectively 500 $M_\odot$, 100 $M_\odot$, and 40 $M_\odot$. In the runs, other parameters are fixed as $M_{\rm halo} = 8 \times 10^5 M_\odot$ and $z_{\rm f} = 20$. At a very early phase of $t_{\rm age} = 0.3$ Myr, the shapes of the profiles in these three runs are very similar to each other, and the peak positions of the absorption feature are almost identical. However, at later phases, the shape of the radial profile strongly depends on the stellar mass; $t_{\rm decay}$ becomes earlier as the stellar mass increases. Figure 5.5 shows the time evolution of the escape fractions in these three runs. The result with a luminous massive star suggests that the short $t_{\rm decay}$ is originated in the leakage of ionizing photons due to rapid expansion of the ionized region. In the case of a less massive star, ionizing photons cannot escape from the halo during the lifetime of the central star so that the deep absorption feature lasts longer as shown by the green dotted curve in Figure 5.4. Thus, we find that $\delta T_{\rm b}(r)$ sensitively depends on the mass of the pop III stars. We would like to emphasize that such a strong dependence of $\delta T_{\rm b}(r)$ on stellar mass appears only if the absorption of ionizing photons in a mini-halo is appropriately solved.

5.3.3 Halo mass dependence

Since the time evolution of $\delta T_{\rm b}(r)$ is sensitive to the dynamics of the ionized gas in a halo as shown in Section 5.3.1, the time evolution is expected to be sensitive to halo mass as well. In this section, we perform simulations with various halo masses and examine the halo mass dependence of the 21-cm signal.

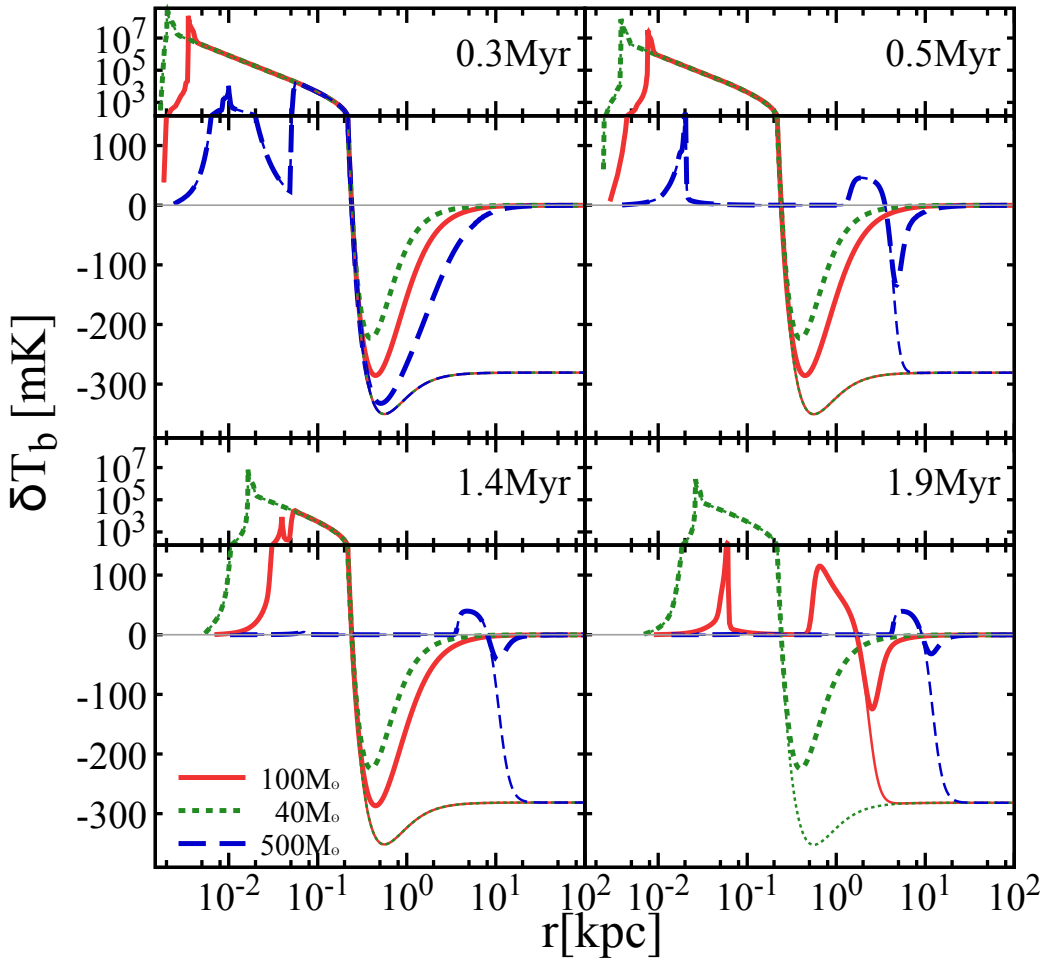

FIGURE 5.4: Radial profiles of the differential brightness temperature at $t_{\rm age} = 0.3$ Myr (upper left), 0.5 Myr (upper right), 1.4 Myr (lower left), and 1.9 Myr (lower right). The profiles obtained from Run-z20S500H8e5, Run-z20S100H8e5, and Run-z20S40H8e5 are shown by the blue dashed, red solid, and green dotted curves, respectively. The thin curves show $\delta T_{\rm b}(r)$ assuming the spin temperature tightly coupled with the gas temperature.

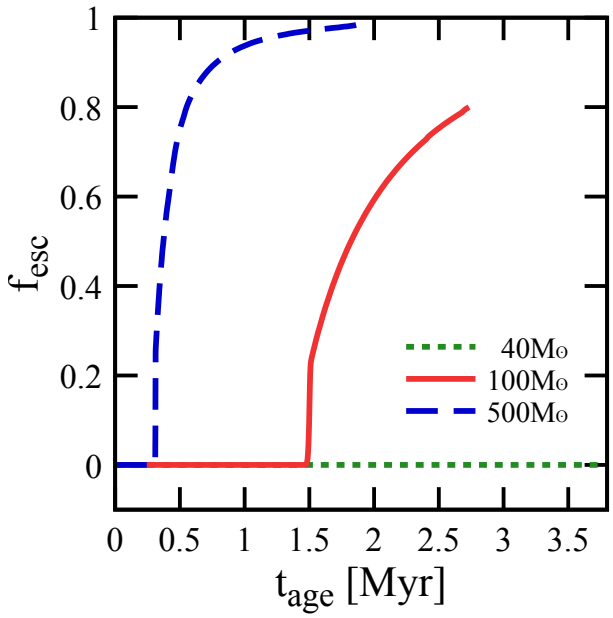

FIGURE 5.5: Time evolution of the escape fraction in Run-z20S500H8e5 (blue dashed curve), Run-z20S100H8e5 (red solid curve), and Run-z20S40H8e5 (green dotted curve).

Figure 5.6 shows the radial profiles of the brightness temperature in Run-z20S100H3e5, Run-z20S100H8e5, and Run-z20S100H3e6, in which different halo masses of 3×10^5 $M_\odot$, 8×10^5 $M_\odot$ and 3×10^6 $M_\odot$ are employed.

The results at an early phase ($t_{age} = 0.4$ Myr) show that the absorption feature has its peak position in further distance from the central star for more massive haloes, and also its amplitude is smaller for more massive haloes. As discussed in Section 5.3.1, the peak position is determined by the distributions of n_{HI} and T_{gas}. More massive haloes are spatially more extended following $r_{vir} \propto M_{halo}^{1/3}$, thus the peak is located farther for more massive haloes. This fact also indicates that Lyα flux from the central star at the peak is weaker for more massive haloes, thus its amplitude is smaller for more massive halo.

In addition, the time evolution from $t_{age} = 0.4$ Myr to 2.7 Myr shows that t_{decay} becomes longer for more massive haloes. This delay is caused by the abundant gas and deep gravitational potential of a massive halo. Figure 5.7 shows the escape fraction of ionizing photons and indeed the rapid increase of the escape fraction is delayed as the halo mass increases. As a result, the massive halo with 3×10^6 $M_\odot$ is able to exhibit the deep absorption feature over the lifetime of the central star even if the star is as massive as 100 $M_\odot$.

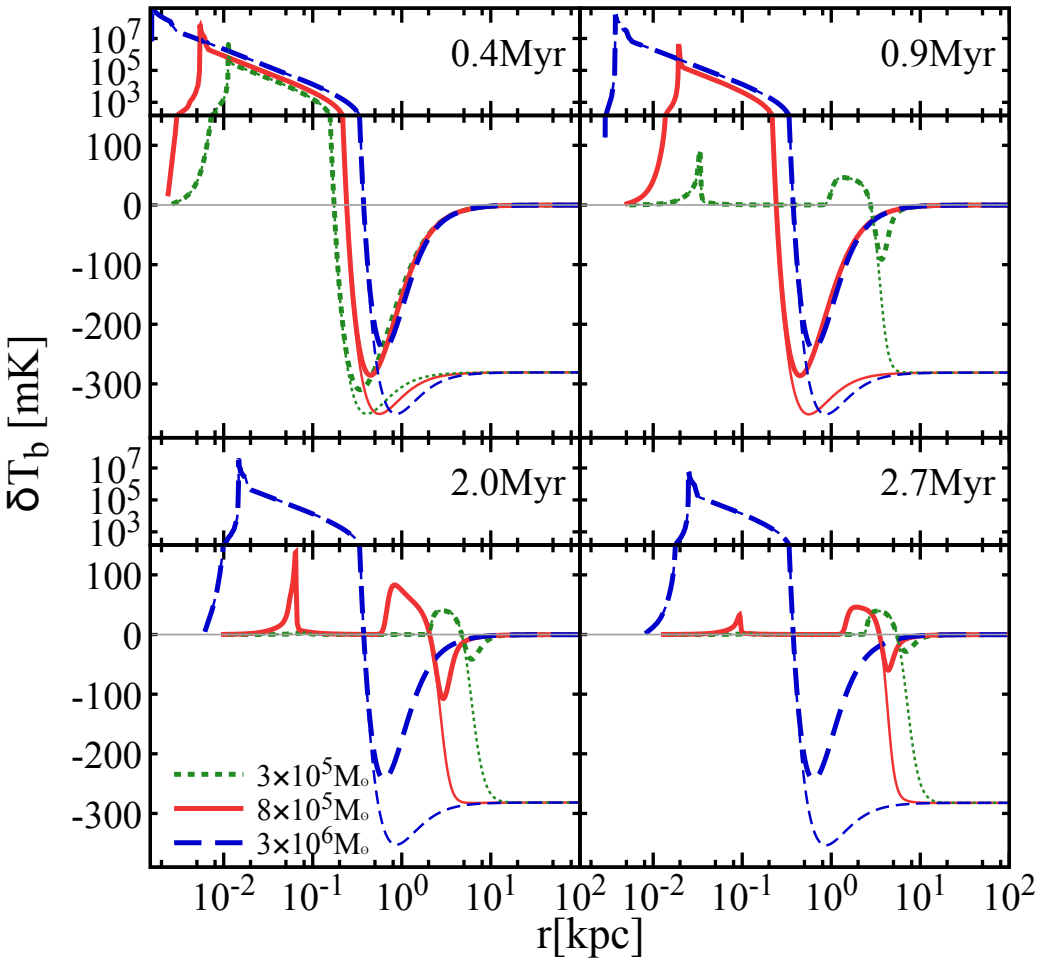

FIGURE 5.6: Same as Figure 5.4, except for showing Run-z20S100H3e5 (green dotted curve), Run-z20S100H8e5 (red solid curve), and Run-z20S100H3e6 (blue dashed curve).

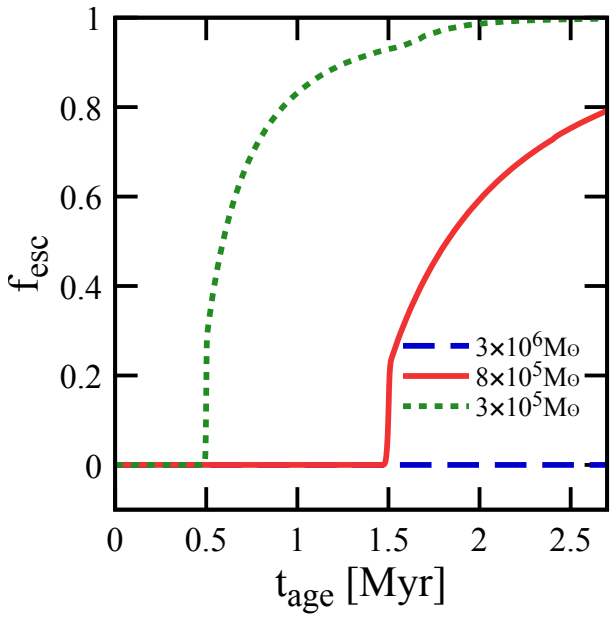

FIGURE 5.7: Same as Figure 5.5, except for showing Run-z20S100H3e5 (green dotted curve), Run-z20S100H8e5 (red solid curve), and Run-z20S100H3e6 (blue dashed curve).

5.3.4 Redshift dependence

In this section, we investigate the redshift dependence of the radial profile of the 21-cm signal, which is likely caused by the variation of gravitational potential and the gas density of a halo at different redshifts.

Figure 5.8 represents the time evolution of $\delta T_{\rm b}(r)$ in Run-z30S100H8e5, Run-z20S100H8e5, and Run-z10S100H8e5. The results at $t_{\rm age} = 0.5$ Myr show that the amplitude of the signal increases as redshift decreases. This behaviour is understood as follow; the differential brightness temperature is approximately proportional to $-1/\sqrt{1+z_{\rm f}}$, because the gas temperature and the CMB temperature respectively scale as $T_{\rm gas} \propto (1+z_{\rm f})^2$ and $T_{\rm CMB} \propto (1+z_{\rm f})$. In addition, the Ly$\alpha$ coupling coefficient, x_α, is proportional to $S_\alpha(z)/T_{\rm CMB}(z)$, where S_α weakly depends on redshift. These two redshift dependences work so as to make the differential brightness temperature lower for lower redshift.

As straightforwardly expected, $t_{\rm decay}$ is earlier for lower redshift halo because of the shallower potential, as indicated by the time evolution of the escape fraction in Figure 5.9. Therefore, the deep absorption feature around the halo at $z = 10$ rapidly disappears, while that at $z = 30$ is sustained for long time.

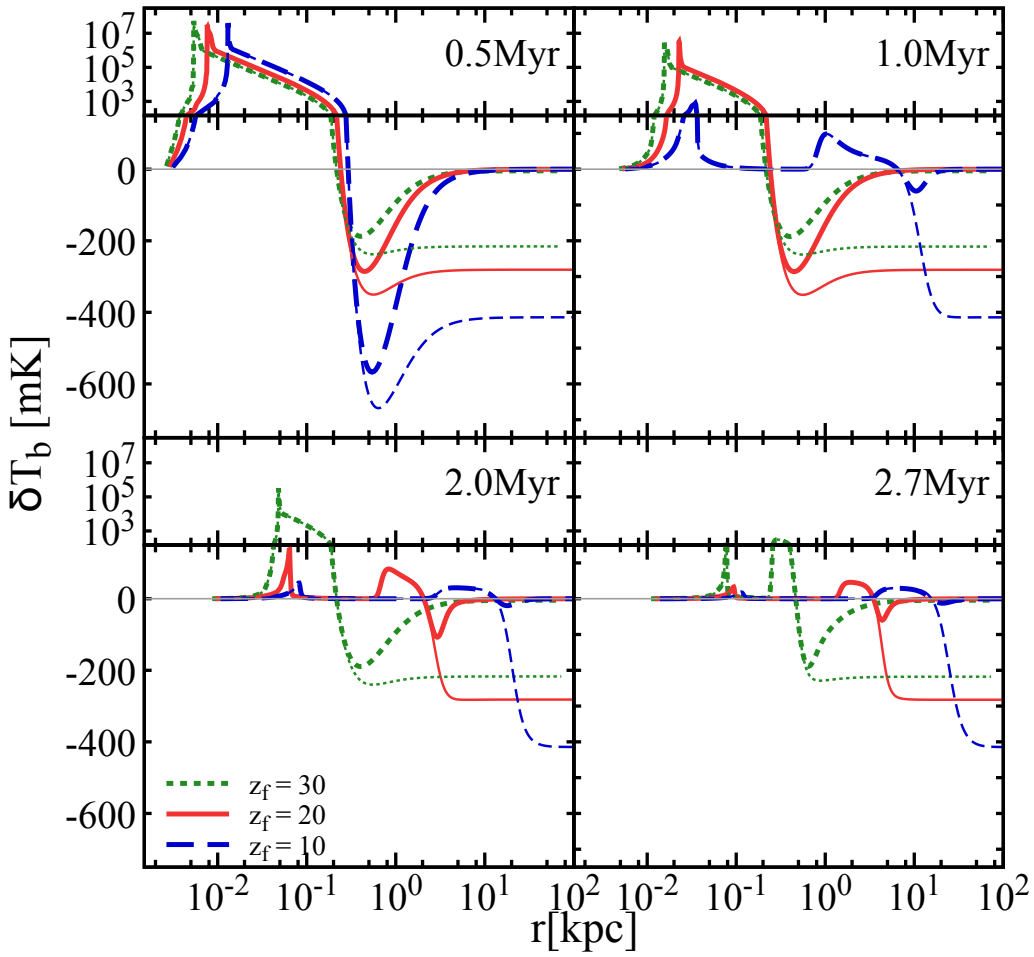

FIGURE 5.8: Same as Figure 5.4, except for showing Run-z30S100H8e5 (green dotted curve), Run-z20S100H8e5 (red solid curve), and Run-z10S100H8e5 (blue dashed curve).

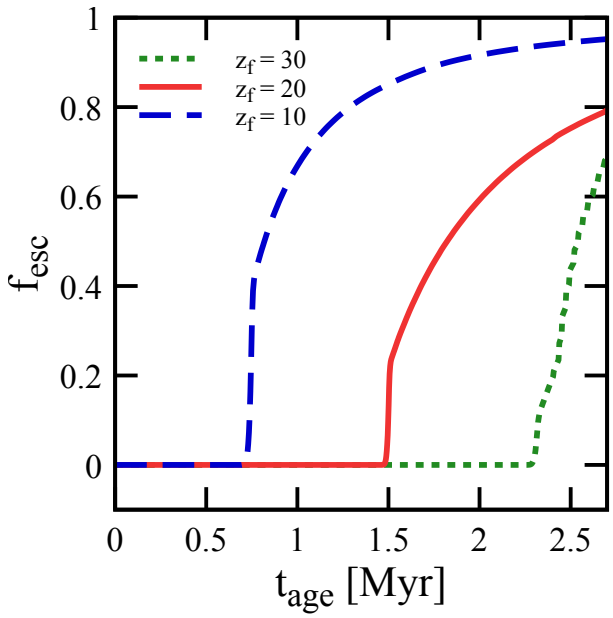

FIGURE 5.9: Same as Figure 5.5, except for showing Run-z30S100H8e5 (green dotted curve), Run-z20S100H8e5 (red solid curve), and Run-z10S100H8e5 (blue dashed curve).

5.3.5 Time evolution of spatially smoothed signal

Our results indicate that the radial profile of the differential brightness temperature is sensitive to the properties of the pop III star. Therefore the detection of the 21-cm signal around individual mini-haloes likely provides us with fruitful information. Before estimating the detectability of signals from individual stars, which we show in the next section, we here calculate the volume-weighted average of $\delta T_{\rm b}(r)$ (hereafter $\langle \delta T_{\rm b} \rangle$) within an expected angular resolution of the SKA (1 arcmin) and understand the behaviour of the smoothed signal.

Figure 5.10 shows the time evolution of the smoothed signals $\langle \delta T_{\rm b} \rangle$ for various parameter sets. Note that we show the absolute values of $\langle \delta T_{\rm b} \rangle$ in Figure 5.10, though all of the original values are negative. As shown in previous sections, the deep absorption feature with ~ -100 mK is most notable if the radial profiles of $\delta T_{\rm b}$ can be spatially resolved. However, the expected angular resolution of the SKA, which corresponds to 1.5×10^2 physical kpc at $z = 20$, does not allow us to resolve it. Therefore, the very weak 21-cm signals ($\delta T_{\rm b} \sim 0$ at the region extended outer than the absorption region) dominate the area within the scale of the SKA angular resolution and the amplitude of a smoothed signal is only up to $\sim 0.1 - 1$ mK. Besides, the amplitude of a smoothed signal becomes stronger for higher $z_{\rm f}$ despite the fact that the absorption features on spatially resolved profiles show the opposite trend (see Section 3.4). The redshift dependence of the smoothed signal is originated from smaller physical scale corresponding to 1 arcmin for higher z, i.e. 1.1×10^2 physical

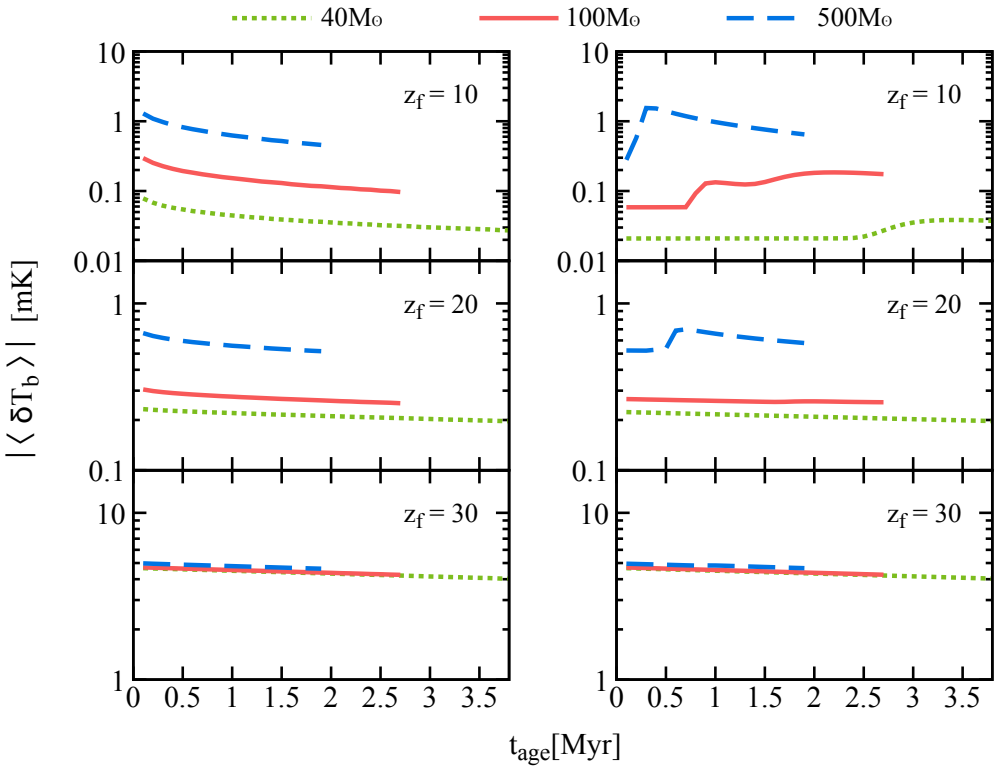

FIGURE 5.10: Time evolution of the spatially smoothed differential brightness temperature $\langle \delta T_b \rangle$, where the smoothing scale corresponds to $\sim$ 1 arcmin. Note that the absolute values of $\langle \delta T_b \rangle$ are shown, though all of the original values are negative. The left and right columns respectively correspond to the cases without and with the dense gas in mini-haloes. In each panel, the time evolution of $\langle \delta T_b \rangle$ for $M_{star} = 40 M_\odot$, $M_{star} = 100 M_\odot$, and $M_{star} = 500 M_\odot$ are indicated by the green dotted, red solid, and blue dashed curves, respectively. In the all cases, the halo mass is set to be $M_{halo} = 8 \times 10^5 M_\odot$.

kpc at $z = 30$ whereas 2.6×10^2 physical kpc at $z = 10$.

The left panels of Figure 5.10 show the time evolution of $\langle \delta T_{\rm b} \rangle$ in the cases of a static and uniform medium (e.g. Run-Ref), where the amplitudes of the smoothed signals monotonically decrease with time and increase with stellar mass because the amplitudes are determined by $x_{\rm ff}$ which is roughly proportional to $M_{\rm star}/r^2$.

On the other hand, the time evolution of $\langle \delta T_{\rm b} \rangle$ obtained from our RHD simulations behaves differently as shown in the right panels of Figure 5.10. (To help understanding the behaviour, the blue dashed line in the right middle panel well represents the typical time evolution.) At the phase of $t_{\rm age} < t_{\rm decay}$, the smoothed signals hardly evolve because the radial profiles are almost steady (see Figure 5.1). Although Figure 5.1 also shows that the absorption feature on $\delta T_{\rm b}(r)$ starts to decay soon after $t_{\rm decay}$, the rapidly expanding signal region, which works to increase the amplitude, dominantly affects the smoothed signal rather than the decreasing amplitude of the deep absorption, thus the amplitude of $\langle \delta T_{\rm b} \rangle$ rapidly increases at this phase. After the sudden increase in $|\langle \delta T_{\rm b} \rangle|$, Ly$\alpha$ coupling efficiency decreases due to the dilution of radiation, resulting in the gradually decreasing $|\langle \delta T_{\rm b} \rangle|$. Although this sequence is commonly seen in $|\langle \delta T_{\rm b} \rangle|$ as far as $t_{\rm decay} < t_{\rm life}$, the earlier phase can only be seen if $t_{\rm decay}$ is late (e.g. Run-z10S100H8e5 indicated by the red solid line in the right-top panel in Figure 5.10). In the cases in which $t_{\rm decay} > t_{\rm life}$ is satisfied (e.g., Run-z30S40H8e5 indicated by the green dotted line in the right-bottom panel in Figure 5.10), $|\langle \delta T_{\rm b} \rangle|$ monotonically decreases as the IGM density decreases via the Hubble expansion.

We emphasize that the amplitudes of the smoothed signals based on the RHD simulations are usually larger than those in the cases with a static and uniform medium after $t_{\rm decay}$, because the smoothed signals in the latter cases start to decay soon after the birth of the star (e.g., comparison between the blue dashed curves in the top panels of Figure 5.10). In contrast, when $t_{\rm age} < t_{\rm decay}$, the opposite trend appears (i.e, the amplitudes of the smoothed signals in the former cases are smaller than those in the latter cases), because the signal regions are quite localized within the vicinities of the haloes. Thus, roughly speaking, resolving gas in a halo enhances the detectability of its smoothed signal if the pop III star (the host halo) is massive (less massive) for which $t_{\rm decay}$ is typically early.

5.3.6 Detectability of 21-cm signal around a mini-halo

In this section, we compare the smoothed signal $\langle \delta T_{\rm b} \rangle$ with noise temperature expected for the SKA. Following Furlanetto et al. (2009), the noise temperature is approximately given by

$$T_{\rm noise} \sim 1.9 \times 10^2 \left(\frac{10^6 \ {\rm m}^2}{A_{\rm eff}} \right) \left(\frac{1 \ {\rm arcmin}}{\Delta\theta} \right)^2 \times \left(\frac{1+z}{21} \right)^{4.6} \left(\frac{\rm MHz}{\Delta\nu} \frac{1000 \ {\rm h}}{t_{\rm int}} \right)^{0.5} \ {\rm mK} \tag{5.24}$$

where $A_{\rm eff}$ is the effective collect area, $\Delta\nu$ is the bandwidth, $\Delta\theta$ is the angular resolution, and $t_{\rm int}$ is the integration time. We adopt $A_{\rm eff} = 10^6$ m^2, $\Delta\theta = 1$ arcmin, $\Delta\nu = 1$ MHz, and $t_{\rm int} = 1000$ h, respectively. According to equation (5.24), $T_{\rm noise} = 9.7$ mK at $z = 10$, $T_{\rm noise} = 1.9 \times 10^2$ mK at $z = 20$, and $T_{\rm noise} = 1.2 \times 10^3$ mK at $z = 30$.

Figure 5.10 immediately informs us that the expected noise level is too high to detect the simulated signals around individual haloes, although the time averaged $|\langle \delta T_{\rm b} \rangle|$ is enhanced by considering dense gas in a halo and the radiation hydrodynamic effects in some cases. One may think that the signals tend to be detectable if we improve the angular resolution. However, finer spatial resolutions in observations do not enhance the detectability because the noise level increases faster than the signals. Therefore we need to increase $A_{\rm eff} \times t_{\rm int}^{0.5}$ to detect the individual signals. For example, $A_{\rm eff} = 2.6 \times 10^6$ m^2 and $t_{\rm int} = 1500$ h are required for detecting the peak in Run-z10S500H8e5 (the blue dashed curve in the top right panel of Figure 5.10) with S/N = 2.

5.4 Application to 21-cm global signal

In this section, we study the 21-cm global signal which reflects properties of the pop III stars, such as SFRD ($\dot{\rho}_\star$), and their typical stellar mass. The results in Section 5.3 show that the radial profiles of the gas temperature, the neutral hydrogen number density, and the Lyff coupling coefficient are written as functions of $M_{\rm star}$, $M_{\rm halo}$, $t_{\rm age}$, and $z_{\rm f}$ (see Figure 5.2). These results allow us to compute the 21-cm global signal considering inhomogeneities of physical quantities required for calculating $\delta T_{\rm b}$ at each position. The following describes the steps for computing the global signal with a given parameter set of $M_{\rm star}$, and $\dot{\rho}_\star$. The redshift is fixed to be $z = 20$ because this is currently the most attractive redshift (Bowman et al., 2018).

1. We randomly place 10 stars with $t_{\rm age}$ in a periodic three dimensional calculation box. The average volume which a pop III star occupies equals to $n_{\rm star}^{-1}$ Mpc^3,

thus the volume of the calculation box containing 10 stars is corresponding to $10 n_{\rm star}^{-1}$ Mpc^3. Here, the number density of the pop III stars, $n_{\rm star}$, is given by

$$n_{\rm star} = \frac{\dot{\rho}_\star t_{\rm life}}{M_{\rm star}}, \tag{5.25}$$

which enables us to take into account $t_{\rm life}$ previous works did not consider. The number of grids is determined so as to let the spatial resolution be 4 physical kpc [2]. The probability distribution of $t_{\rm age}$ obeys the uniform probability with $0 \leq t_{\rm age} \leq t_{\rm life}$. Whereas the masses of haloes hosting the stars are randomly determined according to the Press-Schechter mass function raging from 3×10^5 M$_\odot$ to 4×10^6 M$_\odot$ [3]. The lower limit of the mass function roughly corresponds to the minimum halo mass above which H_2 cooling effectively works (e.g. Tegmark et al., 1997; Nishi and Susa, 1999).

2. We assign $T_{\rm gas}$ and $n_{\rm HI}$ to all grids, by referring to the radial profiles of $T_{\rm gas}$ and $n_{\rm HI}$ obtained from the RHD simulations. We allow the overlaps of haloes: we calculate $n_{\rm HI}$ by summing up components of the all overlapped haloes, and designate the maximum value of $T_{\rm gas}$ among the overlapped components.

3. We determine the Lyα coupling coefficients x_α at all grids. In contrast to the case of an isolated halo shown in Section 5.3, many stars contribute to x_α at a given position. In this case, redshifted continuum photons mainly contribute to x_α. We extrapolate x_α assuming $x_\alpha \propto r^{-2.4}$, and truncate the x_α at the horizon scale of Lyβ photons (see Section 5.2.3 for the detailed explanation of the horizon scale). Then, we sum up all values of x_α at each grid to consider the Lyα flux from all stars. The scaling relation is motivated by the fact that horizon scales are smaller for higher Lyman series photons (Pritchard and Furlanetto, 2006).

4. According to $T_{\rm gas}$, $n_{\rm HI}$, and x_α assigned to all grids, we finally compute $\delta T_{\rm b}$ at the grids with equation (5.15) and (4.15), and average them to obtain the global 21-cm signal, $\delta T_{\rm b,\ global}$. Note that the halo components increase the total hydrogen mass in the calculation box, resulting in an artificially high $\delta T_{\rm b,\ global}$. Thus, we rescale $\delta T_{\rm b,\ global}$ so as to compensate the artificial increase in the total hydrogen mass [4].

We repeat these steps 2000 times to evaluate the mean value and the variance of the global 21-cm signals for a given parameter set of $M_{\rm star}$ and $\dot{\rho}_\star$.

[2] We confirmed that estimated global signals hardly change even if we improve the grid size by an order of magnitude.

[3] We divide the halo mass range into 5 bins of $M_{\rm halo} = 4 \times 10^5M_\odot$, 6×10^5M$_\odot$, 8×10^5M$_\odot$, 10^6M$_\odot$, and 2×10^6M$_\odot$, for which we additionally performed runs.

[4] Without the rescaling, $|\delta T_{\rm b,\ global}|$ turns out to be significantly higher than ~ 200 mK in the case of 40 $M_\odot$ and $\dot{\rho}_\star = 5 \times 10^{-3}$ M$_\odot$ yr^{-1} Mpc^{-3}.

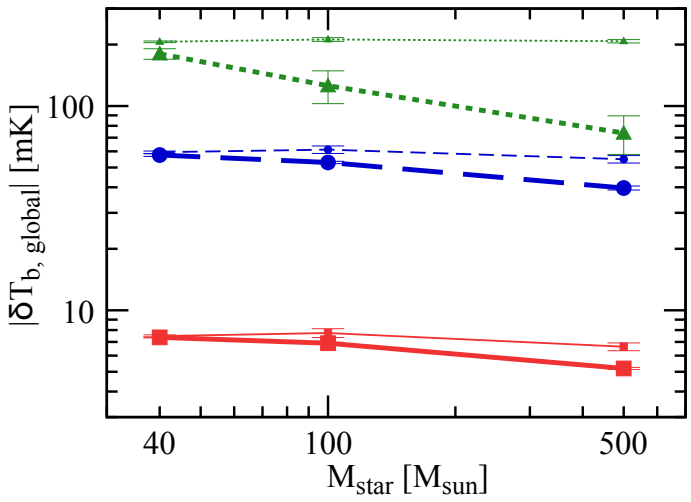

FIGURE 5.11: Absolute value of global 21-cm signals at $z = 20$ for $\dot{\rho}_\star = 5 \times 10^{-5}$ $M_\odot$ yr^{-1} Mpc^{-3} (red solid line), $\dot{\rho}_\star = 5 \times 10^{-4}$ $M_\odot$ yr^{-1} Mpc^{-3} (blue dashed line), $\dot{\rho}_\star = 5 \times 10^{-3}$ $M_\odot$ yr^{-1} Mpc^{-3} (green dotted line) as a function of the stellar mass. Note that all of the original values of the global signals shown in this figure are negative. As for the thick lines the temperature distribution is computed based on the results on RHD simulations, whereas $T_{\rm gas} = T_{\rm IGM}$ is assume for the thin lines.

It is worth clarifying differences between our method and one-zone models which are usually used for evaluating the global signal (e.g. Furlanetto, Oh, and Briggs, 2006). The notable difference appears when the Lyα radiation fields become quite inhomogenous. For example, in a case of $\dot{\rho}_\star = 5 \times 10^{-5}$ $M_\odot$ yr^{-1} Mpc^{-3} and $M_{\rm star} = 500 M_\odot$, we obtain $\bar{x}_\alpha = 0.51$ with our method and $x_\alpha = 0.20$ with an analytical method by Furlanetto, Oh, and Briggs (2006). Accordingly, while our method gives $\delta T_{\rm b,\,global} = -5.2$ [mK], the uniform x_α gives $\delta T_{\rm b,\,global} = -46$ [mK].

As stated in Section 5.1, the stellar-mass-dependent lifetime and heating rate, which previous studies did not consider appropriately, are expected to leave their footprints on the global 21-cm signal. Figure 5.11 shows the obtained global signals for 40 $M_\odot$ $< M_{\rm star} <$ 500 $M_\odot$ and 5×10^{-5} $M_\odot$ yr^{-1} Mpc^{-3} $< \dot{\rho}_\star < 5 \times 10^{-3}$ $M_\odot$ yr^{-1} Mpc^{-3}. Let us pop III discuss how the stellar-mass-dependent lifetime is important, by showing the global signals obtained with an assuming of $T_{\rm gas} = T_{\rm IGM}(z)$ (see equation 5.6) as the thin lines in Figure 5.11. As previous studies (Furlanetto, 2006; Pritchard and Loeb, 2010; Mesinger, Ferrara, and Spiegel, 2013; Yajima and Khochfar, 2015) showed, the amplitude becomes stronger for higher SFRD, because the WF effect becomes more efficient as the number of stars increases. Furthermore, the amplitude decreases with increasing stellar mass: roughly speaking, the amount of Lyα photons is proportional to the total stellar mass, which follows $\propto \dot{\rho}_\star t_{\rm life}$ (equation 5.25). As shown by Table 5.1, the lifetime is longer for less massive

stars, thus the WF effect effectively works to couple the spin temperature with the gas temperature if the pop III stars are less massive. Note that the stellar mass dependence of the global signal coming from the lifetime is weak. For example, with $\dot{\rho}_\star = 5 \times 10^{-4}$ M$_\odot$ yr^{-1} Mpc^{-3}, the amplitudes are -59 mK for $M_{\rm star} = 40$M$_\odot$, and -55 mK for $M_{\rm star} = 500$M$_\odot$.

The discrepancy between the thin and thick lines in Figure 5.11 reflects the importance of heating, because the thick lines are obtained by taking photo-heating by the pop III stars into account. In the highest SFRD case of $\dot{\rho}_\star = 5 \times 10^{-3}$ M$_\odot$ yr^{-1} Mpc^{-3}, the global signal is controlled by the average gas temperature owing to the effective WF effect, consequently the discrepancy is most notable in this case. We note that the heating is less remarkable if $M_{\rm star} = 40$ M$_\odot$ even though the total stellar mass is the largest in this case. This seemingly strange behaviour is caused by the stellar-mass-dependent escape fraction shown in Section 5.3, where we show $t_{\rm decay}$ is later for less massive stars. When $M_{\rm star} = 40$ M$_\odot$, ionizing photons suffer from the absorption by the gas in haloes, thus hardly heat the IGM even with the highest SFRD. In the contrary case of the very massive pop III stars ($M_{\rm star} = 500$ M$_\odot$) for which $t_{\rm decay}$ is early, ionizing photons from the pop III stars well heat the IGM, resulting in the large discrepancy between the thin and thick lines in Figure 5.11. We would like to emphasize that it is very difficult to enhance the amplitude of the global signal if the typical mass of the pop III stars is massive, because the photo-heating rate as well as the Lyα flux increases with SFRD even if we do not consider X-ray radiation.

To conclude, the stellar mass dependence of the 21-cm global signal especially caused by the time-evolving escape fraction is quite important, though the calculation in this section may be too simplified to quantitatively promise the dependence of the global signal on the SFRD and the pop III star mass.

5.5 Discussion

In this work, we focus only on the 21-cm signature around the main sequence pop III stars. However, in reality even after the lifetime of the central stars, partially ionized regions remain as relic HII regions. Tokutani et al. (2009) found that relic HII regions are bright in the 21-cm line during the recombination time of the IGM. Since the recombination time, which corresponds to an order of 10 Myr at high redshifts, is much longer than the typical lifetime of the pop III stars, the emission from such relic HII regions likely contribute to the global 21-cm signal. In addition, it has been known that the fate of the pop III star depends on its mass (e.g., Heger and Woosley, 2002; Umeda and Nomoto, 2002; Tominaga, Umeda, and Nomoto, 2007), and the pop III star with a certain mass range ends its life as an energetic supernova

(SN). Kitayama and Yoshida (2005) reported that the SN significantly affects the distribution of the gas temperature and density around a mini-halo. Shocks induced by the SN expand outward and sweep up the gas in a relic HII region, resulting in the enhancement of the detectability of an individual relic region. Also high energy photons emitted from the heated gas are expected to affect the IGM temperature and thus impact the 21-cm brightness temperature. Further studies of the stellar mass dependence of the 21-cm signals by considering the effects of relic HII regions, SN, and high-energy photons are needed.

Yajima and Li (2014) studied the distinctive 21-cm signatures around the galaxies and quasars, but did not consider the effects by the dense gas in a halo and gas dynamics. The effects are also expected to play an important role on the brightness temperature around galaxies and quasars as well as the pop III stars as shown in the chapter.

When we evaluate the global 21-cm signal, we simply assume that the pop III stars are randomly distributed. However, in reality, the distribution of the stars obeys the background matter distribution, and the number density of the pop III stars depends on the local density (Ahn et al., 2012). Measuring the 21-cm fluctuation arisen by the inhomogeneous distribution of the pop III stars likely provides us with the information of the clustering of the pop III stars as well as the typical scale of a 21-cm signal region. Such large scale 21-cm signal and its fluctuations are studied in the next chapter.

5.6 Summary of this chapter

In this work, we first performed RHD simulations resolving gas distribution in a mini-halo which previous studies omitted, to investigate the 21-cm signal distribution around the pop III stars. The simulations with such a new point enable us to consider the time-evolving escape fraction. When the escape fraction is considerably small, a characteristic deep absorption feature with $\delta T_{\rm b} < -100$ mK appears at the outer rim of a halo where the gas is colder than the CMB temperature. The deep absorption signal starts to decay after the escape fraction rapidly increases at the characteristic time $t_{\rm decay}$, then the signal shape becomes similar to that in previous studies where they assume the static and uniform medium. We found for the first time that the resultant radial profile of the brightness temperature strongly depends on the properties of the pop III stars and the host halo, because the time evolution of the escape fraction is sensitive to the luminosity of the central star and the gravitational potential of the halo as shown by Kitayama et al. (2004). In our simulations, $t_{\rm decay}$ is earlier for more massive stars, for less massive haloes, and for lower redshift

haloes, as straightforwardly expected. In some cases that $t_{\rm decay}$ is longer than the stellar lifetime, the absorption feature is sustained until the central star dies.

Next, we discussed the detectability of the 21-cm signals around individual haloes by comparing the simulated signals with the currently expected specification of the SKA. Since an expected angular resolution of the SKA is much larger than the typical virial radius, the radial profile of $\delta T_{\rm b}$ is spatially smoothed out and its amplitude decreases down to $\sim 0.1-1$ mK. Thus, the currently expected specification of the SKA is insufficient to detect the individual signal, although the time-evolving brightness temperature in our simulations often enhances the amplitude of the smoothed signal. We proposed that $A_{\rm eff} \times t_{\rm int}^{0.5} = 1.0 \times 10^8$ [m^2 h$^{0.5}$] is at least required for the detection of the 21-cm signal around individual haloes.

We finally investigated how the properties of the pop III stars are reflected on the 21-cm global signal, by utilizing our simulation results. Given SFRD, less massive stars with longer lifetime provide larger amount of Lyα photons than massive stars do, thus the WF effect becomes more effective if the pop III stars are typically less massive. However, this effect turns out to be not notable because of the weak dependence of the lifetime on the stellar mass (see Table 5.1). The dominant process controlling the stellar mass dependence of the 21-cm global signal is the heating rate originated in the time-evolving escape fraction described above: the earlier $t_{\rm decay}$ for more massive stars leads to more efficient heating of the IGM. An interesting prediction from our results is that the extremely strong absorption feature of the 21-cm global, e.g. ~ -200 mK at $z = 20$, is difficult to be reproduced even with an extremely high SFRD if the pop III stars are typically very massive. In summary, to interpret the 21-cm global signals, it is desirable to take into account heating by the pop III stars, which strongly depends on $t_{\rm decay}$ (thus on the stellar mass).

Chapter 6

Cosmological 21-cm signal and population III stars

In this chapter, we summarize our research about the cosmological 21-cm signal originated from Pop III stars. This chapter is mainly composed of (Tanaka and Hasegawa, 2020)

6.1 Introduction: Previous works and aim of the chapter

As we see in the previous chapter, detecting the individual 21-cm signature around Pop III stars is difficult even with SKA. Thus, theoretically modeling the cosmological scale signal, which is much more detectable than the individual signal, is urgently needed to extract information on the properties of Pop III stars. Ahn et al., 2012 have conducted the radiative transfer (RT) simulations in cosmological scale with the sub-grid model about the number of MHs in simulation grids, instead of directly resolving MHs which need enormous computational resources. They have calculated 21-cm power spectrum assuming the tight coupling between the gas kinetic temperature and the spin temperature (Shapiro et al., 2012). Visbal, Bryan, and Haiman, 2020 have used semi-analytic methods to efficiently calculate the 21-cm signal. However, the models of Pop III stars in these previous works are rather simple. For instance, they assume constant escape fraction of ionizing photons in time. Therefore, we in this work develop an elaborated model of Pop III stars, focusing on not only the escape fraction of the ionizing photons and also UV photo-heating on the gas kinetic temperature, which has ever been neglected, and investigate impacts of the escape fraction and UV photo-heating on the 21-cm statistics such as the 21-cm global signal and the power spectrum.

The escape fraction is known to depend on the halo mass and the stellar mass in the halo (Kitayama et al., 2004; Tanaka et al., 2018). The LW negative feedback boosts the minimum halo mass able to hold enough number of molecular hydrogen for star formation, therefore, the escape fraction of MHs should depend on the LW intensity. Therefore, the escape fraction of the LW photons is also important as well as that of

ionizing photons, however, it is often neglected and set to be unity in cosmological 21-cm signal calculations (e.g. Visbal, Bryan, and Haiman, 2020; Qin et al., 2020a; Qin et al., 2020b). We self-consistently incorporate the LW negative feedback on the Pop III star formation and the escape fractions of ionizing photons and the LW photons.

UV photo-heating has ever been neglected in 21-cm signal simulations because its mean free path is relatively short so that the UV photo-heated region and the ionized region well overlap each other. However, Yajima and Li, 2014 found that Pop III stars create large partially ionized region due to the high effective temperature, in which the gas temperature is much higher than the CMB temperature resulting in positive value of 21-cm brightness temperature. Also, Tanaka et al., 2018 found that this UV photo-heating has non-negligible effect on the global 21-cm signal in some cases like star formation rate density (SFRD) is high by simple estimation using the results from the radiation hydrodynamics (RHD) simulations which is summarized in the previous chapter.

In this work, we develop new MH model, focusing on the escape fractions of both ionizing and H_2-dissociating photons, and installed it in the public semi-numerical simulation code, 21cmFAST (Mesinger, Furlanetto, and Cen, 2011). Also, our simulation, for the first time, incorporates the effect of UV photo-heating using the results of detailed RHD simulation. And, we evaluate the impacts of LW-intensity-dependent escape fractions and UV photo-heating on the cosmological 21-cm signals.

This chapter is organized as follows. In Section 6.2, we describe the method to account for UV photo-heating, to incorporate the LW negative feedback, and to model time-evolving escape fraction dependent on the LW background intensity using RHD simulation results. Also, we explain the modification of ionization calculation of 21cmFAST in order to solve some difficulties occurred due to the time-evolving escape fraction. Then, showing simulation results in Section 6.3, we explain how our escape fraction model and UV photo-heating affect the ionization history, the 21-cm global signal, and the 21-cm power spectrum. In addition, whether we can distinguish SFRD and typical stellar mass of Pop III stars is investigated. We next discuss the limitation and uncertainties of this work in Section 6.5, and finally summarize this chapter in Section 6.6.

6.2 New simulation code

In this section, we first summarize the basics of the 21-cm signal, introduce the public code, 21cmFAST, and then describe the method to take into account UV photo-heating, the model of time-evolving escape fractions, and the modification of the ionization calculation of the 21cmFAST code.

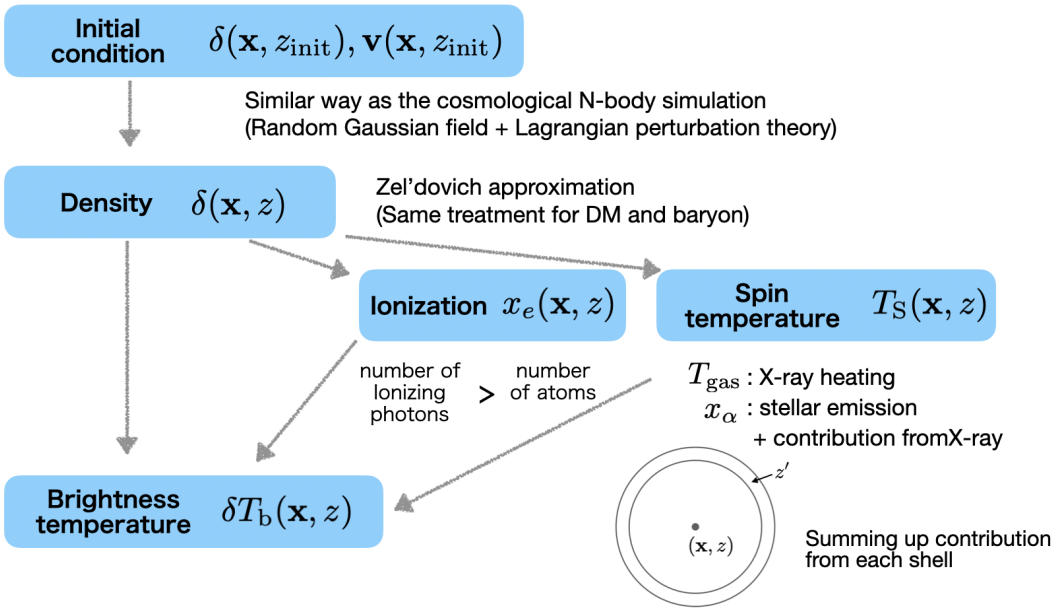

FIGURE 6.1: The calculation flow of 21cmFAST.

The cosmological 21-cm signal can be written as (e.g. Furlanetto and Oh, 2006)

$$\delta T_{\rm b} = 38.7 x_{\rm HI}(1+\delta)\left(\frac{1+z}{20}\right)^{1/2}\frac{T_{\rm S}-T_{\rm CMB}(z)}{T_{\rm S}}{\rm mK}, \tag{6.1}$$

where $x_{\rm HI}$ is fraction of neutral hydrogen, δ is overdensity, and $T_{\rm CMB}(z)$ is the CMB temperature at redshift z, respectively. The spin temperature $T_{\rm S}$ is determined by,

$$T_{\rm S}^{-1} = \frac{T_{\rm CMB}^{-1} + x_{\rm c}T_{\rm gas}^{-1} + x_\alpha T_\alpha^{-1}}{1 + x_{\rm c} + x_\alpha} \tag{6.2}$$

where $T_{\rm gas}$, T_α, $x_{\rm c}$, and x_α are the gas kinetic temperature, the color temperature of the Lyα photons, the collisional coupling coefficient, and Lyα coupling coefficient, respectively. We assume $T_\alpha = T_{\rm gas}$ because of the large cross section of Lyα photons to neural hydrogen.

6.2.1 21cmFAST

We develop new module for Pop III stars and install it on the 21cmFAST which is publicly opened semi-numerical simulation code able to efficiently generate three-dimensional realizations of the cosmological 21-cm signal and its time evolution (Mesinger, Furlanetto, and Cen, 2011). The advantage of 21cmFAST is low computational cost so that we can run simulations relatively many time with limited computational resources.

The calculation flow of 21cmFAST is shown in Figure 6.1. The initial condition is generated in roughly the same way as the cosmological N-body simulations, that

is, the combination of the initial random Gaussian field and the Lagrangian perturbation theory. Then, using the obtained initial conditions of density field and velocity field at initial redshift $z_{\rm ini}$, the 21cmFAST code calculates the density field at z ($z < z_{\rm ini}$) with the Zel'dovich approximation (Section 3.2.3). The baryon is treated in the same way as the dark matter. This approximation enables us to simulate fast, but, at non-linear regime, the calculation accuracy decreases. As long as we focus on the linear regime, it should be a good approximation.

The method to obtain ionization field is described in detail in Section 6.2.4, but basically, 21cmFAST judges whether the cell is ionized or not by comparing the numbers of ionizing photons and atoms in that cell. The emissivity of ionizing photons is controlled by the parameter, $N_{\rm UV}$, which is the number of ionizing photons produced by single stellar baryon.

As for the field of spin temperature, inhomogeneous Lyα radiation field is taken into account. Not only the direct stellar emission but also contribution from X-ray are considered as Lyα sources: When the X-ray photon ionizes a HI, high-energy electron is produced. The electron excites surrounding HI, and the excited HI emits Lyman series photons. As for gas temperature, the X-ray gas heating is considered. In order to calculate the X-ray intensity or Lyα intensity at position $\mathbf{x}$ at redshift z, 21cmFAST sums up contributions from shells whose center is at $(\mathbf{x}, z)$ instead of solving the radiative transfer equation. This method remarkably reduces the computational cost. The emisivity of Lyman series photons is based on the spectral model of Barkana and Loeb, 2005.

The self-consistently generated 3D distributions of density, HI fraction, and spin temperature are used to obtain the 21-cm brightness temperature field at the end.

6.2.2 Gas heating by UV radiation

Even though the mean free path of UV radiation emitted from massive PopIII stars is longer than that of galaxies due to the high effective temperature, and have considerable impact on surrounding 21-cm signature, it is still too short to consider UV photo-heating is uniform in a simulation grid (The grid size of semi-numerical simulation is typically ~ 1 comoving Mpc). In the case of X-ray, mean free path is exceedingly long (~ 1 Gpc at $z = 20$, $h\nu = 5$ keV, assuming cosmic mean baryon density) so that X-ray heating can be treated as uniform heating in grid. On the other hand, the mean free path of UV photons (~ 1 kpc at $z = 20$, $h\nu = 50$ eV) is much shorter than the size of simulation grids. In the calculation of 21-cm brightness temperature, when sub-grid scale fluctuation of gas temperature is neglected and averaged gas temperature is used, the resulting 21-cm brightness can be totally wrong because of the non-linearity of the gas temperature dependence of 21-cm brightness. For instance, if gas temperature is extremely high in a small region in a grid and the other

regions are cold, the averaged gas temperature of the grid would become hotter than the CMB temperature, resulting in emission signal, nevertheless, the absorption signal should be obtained.

In order to incorporate the inhomogeneous UV photo-heating in sub-grid scale, we develop a new method: we divide the whole region of a grid into three different regions which are the ionized region, the cold region, and the heated region. The ionized region is where no neutral hydrogen exists and no signal comes from. The cold region is a neutral region and not heated so that gas in this region absorbs the background CMB radiation. The heated region is slightly ionized and its gas temperature is higher than the CMB temperature, creating a emission signal. When we write the 21-cm brightness temperatures in these three regions as $\delta T_{\rm b,ion}$, $\delta T_{\rm b,cold}$, $\delta T_{\rm b,heat}$, the 21-cm signal of the grid can be written as:

$$\delta T_{\rm b,grid} = \sum_i f_i \delta T_{{\rm b},i} \quad (i = \text{ion, cold, heat}), \tag{6.3}$$

where $f_{\rm i}$ is the volume fraction of i region. Since $\sum_i f_i = 1$, we need ionized fraction $f_{\rm ion}$ and ratio of heated region to ionized region, $\gamma_{\rm h/i} \equiv f_{\rm heat}/f_{\rm ion}$. We describe how to calculate ionization filed with semi-numerical simulations in Section 6.2.4. The 21-cm brightness temperatures in these three regions are expressed as

$$\delta T_{\rm b,ion} = 0\ {\rm mK}, \tag{6.4}$$

$$\delta T_{\rm b,cold} = 38.7(1+\delta)\left(\frac{1+z}{20}\right)^{1/2}\frac{T_{\rm S}-T_{\rm CMB}(z)}{T_{\rm S}}\ {\rm mK}, \tag{6.5}$$

$$\delta T_{\rm b,heat} = 38.7(1+\delta)\left(\frac{1+z}{20}\right)^{1/2}\ {\rm mK}. \tag{6.6}$$

where we assume strong Lyα coupling in the heated region because the heated region is close enough to Pop III stars to have high intensity of Lyman series photons shown by Tanaka et al., 2018.

In order to investigate $\gamma_{\rm h/i}$, we conduct one-dimensional spherically-symmetric RHD simulations developed by Tanaka et al., 2018. The RHD simulation can produce the profile of 21-cm brightness temperature around an individual MH hosting a Pop III star by solving gas dynamics, radiative transfer of ionizing photons, and non-equilibrium chemical reactions. We assume that one MH hosts one PopIII star at the center. As some studies have shown (Tanaka et al., 2018; Chen and Miralda-Escudé, 2008; Yajima and Li, 2014), the 21-cm signature around the Pop III star has typical structure: The most-inner region is ionized region where no neutral hydrogen remain, resulting in a zero signal. The next outer region is a heated region where gas is partially ionized and heated above the CMB temperature so that the emerging signal is emission. The region outside the heated region is the cold region where the

gas remain cold below the CMB temperature while the Lyα coupling is sufficiently strong to couple the spin temperature with the cold gas temperature, showing the absorption signal.

To estimate $\gamma_{\rm h/i}$, we use the profiles of ionized fraction and 21-cm brightness temperature calculated with the RHD simulations. We locate the ionized and heated regions around the MHs as follows: The boundary between these two is defined as the shell whose neutral fraction is 1%. Whereas the boundary between the heated and cold regions is defined as where the $\delta T_{\rm b}$ first turns to be positive, judging from the most-outer cold shell. Once we locate the radius of the ionized region $r_{\rm ion}$ and the outer radius of the heated region $r_{\rm heat}$, $\gamma_{\rm h/i}$ can be calculated as $\gamma_{\rm h/i} = (r_{\rm heat}^3 - r_{\rm ion}^3)/r_{\rm ion}^3$. The ionization fraction at the heated region defined in this way is less than 10%, therefore we treat the heated region as neutral one for simplicity.

Figure 6.2 shows $\gamma_{\rm h/i}$ as a function of redshift. At higher redshift, the value decreases. To understand the behaviour, we write the ratio as $\gamma_{\rm h/i} = 3(l/r_{\rm ion}) + 3(l/r_{\rm ion})^2 + 3(l/r_{\rm ion})^3$ where $l \equiv r_{\rm heat} - r_{\rm ion}$ is the width of the heated region which roughly corresponds to the average mean free path of UV photons. To think simply, we regard the ionized region as ionized sphere which located at uniform density field and its ionization status is far from the ionization equilibrium. Then the $r_{\rm ion} \propto n^{1/3}$ because $N_{\rm ion} = (4/3)\pi r_{\rm ion}^3 n$ for given ionizing photon number $N_{\rm ion}$, where n is the number density of gas, assuming the gas is composed of only hydrogen. On the other hand, $l \propto n^{-1}$, therefore as redshift increases and the mean density of the Universe gets denser, $l/r_{\rm ion}$ becomes smaller, resulting in smaller $\gamma_{\rm h/i}$.

The stellar mass dependence of $\gamma_{\rm h/i}$ is smaller than the error which is originated from the spacial resolution of the RHD simulations (see the blue solid line, orange dashed line, and these error regions in Figure 6.2), so that we neglect the stellar mass dependence. In details, the stellar mass dependence of the effective temperature affects the mean free path of UV photons. Also, the different life time of different stellar mass of Pop III stars slightly influences the resulting $\gamma_{\rm h/i}$.

The halo mass dependence is too small to affect the $\gamma_{\rm h/i}$ (see the dashed orange line and green dash-dotted line in Figure 6.2) as well as the stellar mass dependence. Thus, we neglect the dependence in this work. Although $\gamma_{\rm h/i}$ of massive MHs ($\gtrsim 3 \times 10^6 {\rm M}_\odot$) would be different because of dense gas profile in and near the vrial radius, the Pop III star does not emit enough ionizing photons within the lifetime to ionize whole gas in such massive haloes. Therefore, these massive MHs do not contribute ionization degree of the Universe due to the nearly-zero escape fraction of ionizing photons.

We develop the fitting formula for $\gamma_{\rm h/i}$ (the thin black solid line in Figure 6.2):

$$\log(\gamma_{\rm h/i}) = -3.11 \log(1+z) + 5.23. \tag{6.7}$$

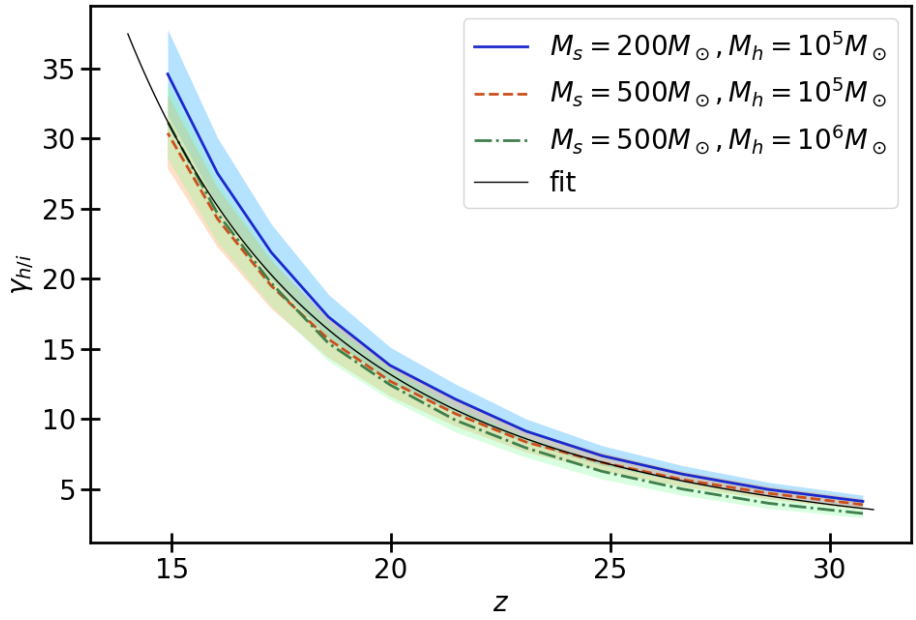

FIGURE 6.2: $\gamma_{\mathrm{h/i}}$ as a function of redshift. The blue solid line is the case of $M_{\mathrm{s}} = 200\mathrm{M}_\odot$, $M_{\mathrm{h}} = 10^5\mathrm{M}_\odot$, the orange dashed line is the case of $M_{\mathrm{s}} = 500\mathrm{M}_\odot$, $M_{\mathrm{h}} = 10^5\mathrm{M}_\odot$, the green dashed-dotted line is the case of $M_{\mathrm{s}} = 500\mathrm{M}_\odot$, $M_{\mathrm{h}} = 10^6\mathrm{M}_\odot$. The shaded regions represent the errors originating from the spacial resolution of the one-dimension RHD simulation. The thin black solid line is fitted line.

We use the formula to obtain the value of $\gamma_{\mathrm{h/i}}$.

6.2.3 LW feedback

The LW photons dissociate molecular hydrogen, suppressing the formation of Pop III stars in MHs. In this work, we take into account the negative feedback and its redshift dependence by calculating the box-averaged LW intensity at each redshift. The LW intensity, J_{LW}, boosts the minimum halo mass which can hold enough number of molecular hydrogen to cool gas and form stars, M_{cool}. The relation of J_{LW} and M_{cool} is investigated with numerical simulations (Machacek, Bryan, and Abel, 2001; Wise and Abel, 2007; O'Shea and Norman, 2008), and it is well fitted by (Visbal et al., 2014)

$$M_{\mathrm{cool}} = 3.4 \times 10^5 \left(\frac{1+z}{21}\right)^{-1.5} \times \left\{1 + 6.96\left(4\pi J_{\mathrm{LW}}(z)\right)^{0.47}\right\} M_\odot, \tag{6.8}$$

where, the unit of J_{LW} is $[10^{-21}\ \mathrm{erg\ s^{-1}\ cm^{-2}\ Hz^{-1}\ str^{-1}}]$.

We calculate $J_{\mathrm{LW}}(z)$ by averaging the LW intensity at each grid, $\mathcal{J}_{\mathrm{LW}}(\mathbf{x}, z)$, over the simulation box. $\mathcal{J}_{\mathrm{LW}}(\mathbf{x}, z)$ is obtained by the way similar to that of X-ray intensity implemented in the original 21cmFAST and that used in Fialkov et al., 2013, which

sums up contributions from shells whose center is at the grid position **x**:

$$\mathcal{J}_{\rm LW}(\mathbf{x}, z) = \int_z^{z_{\rm max}} {\rm d}z' \frac{1}{4\pi} \frac{1}{4\pi r_{\rm p}^2} \frac{{\rm d}\varepsilon(\mathbf{x}, z')}{{\rm d}z'}, \tag{6.9}$$

where z' is corresponding to the redshift when the reached photons to the grid was emitted in each shell, and the $r_{\rm p}$ is the proper distance from the shell. The LW specific emissivity per redshift [erg s^{-1} Hz^{-1}] can be written as,

$$\frac{{\rm d}\varepsilon(\mathbf{x}, z')}{{\rm d}z'} = \left(\frac{N_{\rm LW} E_{\rm LW}}{\Delta\nu_{\rm LW}} \right) f_* f_{\rm esc,LW}\, \bar{n}_{\rm b,0} (1 + \bar{\delta}_R) \frac{{\rm d}V}{{\rm d}z'} \frac{{\rm d}f_{\rm coll}}{{\rm d}t}, \tag{6.10}$$

where f_* is the star formation efficiency, $f_{\rm esc,LW}$ is the escape fraction of the LW band photons, $\bar{n}_{\rm b,0}$ is the mean baryon number density at $z = 0$, $\bar{\delta}_R$ is the overdensity averaged over the shell scale R, ${\rm d}V$ is the comoving volume of the shell, and ${\rm d}z$ is redshift width corresponding to the shell width, respectively. The factor $(N_{\rm LW} E_{\rm LW} / \Delta\nu_{\rm LW})$ means the energy of LW photons per stellar baryon per frequency. We adopt values used in Mebane, Mirocha, and Furlanetto, 2018. The escape fraction of dissociation photons, $f_{\rm esc,LW}$, has similar dependences of halo mass, stellar mass, and redshift to that of ionizing photons (Kitayama et al., 2004). Therefore, we use our escape fraction model of ionizing photons, which is described in Section 6.2.4, for the LW escape fraction for simplicity. In terms of $z_{\rm max}$, we assume all LW band photons redshift by 4% before absorbed by any Lyman lines (Visbal et al., 2014):

$$\frac{1 + z_{\rm max}}{1 + z} = 1.04. \tag{6.11}$$

Using equation (6.9) and (6.10), we get (c.f. Equation (25) of Mesinger, Furlanetto, and Cen 2011):

$$\mathcal{J}_{\rm LW}(\mathbf{x}, z) = \frac{f_* \bar{n}_{\rm b,0} c}{4\pi} \frac{N_{\rm LW} E_{\rm LW}}{\Delta\nu_{\rm LW}} \int_z^{z_{\rm max}} {\rm d}z' (1 + z')^3 (1 + \bar{\delta}_R) \frac{{\rm d}f_{\rm coll}}{{\rm d}z'}, \tag{6.12}$$

where, c is the speed of light.

6.2.4 Ionization field

We estimate the effect of UV photo-heating on the cosmological 21-cm signal using ionization field and $\gamma_{\rm h/i}$ as described in Section 6.2.2. In the original 21cmFAST code, the criteria judging whether a grid is ionized or not is:

$$\zeta_{\rm ion} f_{\rm coll} > 1 + \bar{n}_{\rm rec}, \tag{6.13}$$

where $\zeta_{\rm ion} = N_{\rm UV} f_{\rm esc} f_*$ with $N_{\rm UV}$ being the number of ionizing photons per stellar baryon, and $\bar{n}_{\rm rec}$ being the number of recombination per baryon. When taking into

account the time-evolving LW feedback, two problems occur.

One problem is that the collapse fraction has redshift dependence induced by $M_{\rm cool}(J_{\rm LW}(z))$. Therefore, equation (6.13) cannot judge the ionization status appropriately. For example, when the LW intensity rise rapidly, the critical halo mass for star formation, $M_{\rm cool}$, also rises rapidly, then the collapse fraction, which is the fraction of matter collapsed in more massive haloes than $M_{\rm cool}$, possibly decreases in time. In such a case, the part of ionizing photons emitted in the past is not counted to judge the ionization status.

The other problem is about the escape fraction of ionizing photons. Sicne the escape fraction depends on halo mass, the value of the escape fraction should be obtained by taking average weighted by the halo mass function (MHF). The $M_{\rm cool}$ gives the minimum value of halo mass in the integration, meaning that the escape fraction depends on the $J_{\rm LW}(z)$. This dependence of $f_{\rm esc}$ would have large impact on the ionization history of the Universe: At $z = 20$, the averaged escape fraction over the stellar lifetime with halo mass of $M_{\rm h} = 3 \times 10^5$ / $2 \times 10^6 M_\odot$, hosting a signal PopIII star with mass of $M_{\rm s} = 200 M_\odot$, are $f_{\rm esc} \sim 0.6$ / 0.0, respectively. The minimum mass becomes $M_{\rm cool} \sim 2 \times 10^6 M_\odot$ when $J_{\rm LW} = 0.05$, which means the escape fraction becomes nearly zero before the LW feedback saturates. The massive halos whose escape fraction is zero do not contribute the reionization anymore.

In order to solve the two difficulties explained above and calculate ionization field appropriately with the time-evolving escape fraction, we develop new methodologies: (1) we modify the ionization criterion and (2) develop sub-grid model of the escape fraction using high-resolution N-body simulations and the detailed RHD simulations. Our method is only valid at high redshift when Pop III stars are the dominant sources of ionizing photons. In following part of this section, we describe the method.

Ionization calculation including recombination

We introduce a new criterion below to account for the redshift dependencies of the escape fraction and the collapse fraction induced by time-evolving $M_{\rm cool}$:

$$\bar{N}^R_{\rm ion} > 1 + \bar{N}^R_{\rm rec}. \tag{6.14}$$

where $\bar{N}^R_{\rm ion}$ and $\bar{N}^R_{\rm rec}$ are the numbers of ionizing photons and recombination per baryon spatially averaged at scale R, based on values at each grid, $N_{\rm ion}(\mathbf{x})$ and $N_{\rm rec}(\mathbf{x})$:

$$N_{\rm ion} = \int_z^{z_{\rm init}} {\rm d}z\, \zeta_{\rm ion}(z) \frac{{\rm d}f_{\rm coll}(z)}{{\rm d}z}. \tag{6.15}$$

$$N_{\rm rec} = \int_z^{z_{\rm init}} {\rm d}z\, \alpha_{\rm B} n_{\rm H} (N_{\rm ion,prev} - N_{\rm rec,prev}) \frac{{\rm d}t}{{\rm d}z} \tag{6.16}$$

where, α_B is the case-B recombination coefficient, n_H is the number density of hydrogen, $N_{ion,prev}$ and $N_{rec,prev}$ are the values at the previous time step. Note that N_{rec} is different from n_{rec} introduced by Sobacchi (2014): The n_{rec} is the recombination number in a fully ionized cell to keep the grid ionized, which means they do not take into account recombination before the cell is fully ionized. On the other hand, our N_{rec} additionally includes the recombination when the cell is partially ionized. Indeed Visbal, Haiman, and Bryan, 2018 found that the recombination can be ignored due to the rapid growth of the star formation rate density. However, in our simulations, the escape fraction would drop to nearly zero so that the emissivity of ionizing photons can decrease. Therefore, the recombination is needed to be taken into account.

With the criterion, equation (6.14), simulation cells are judged weather they are fully ionized or not from the largest scale to the cell scale. We take 30 Mpc as the largest scale which is large enough in the high redshift we are interested in. If the cells are not judged as fully ionized even at the cell scale, the ionization fraction is calculated by $x_e = \min\{N_{ion} - N_{rec}, 1\}$. This is because $N_{ion} - N_{rec}$ does not mean ionization fraction but means the number of surrounding cells the cell can ionize with photons produced in the cell. Thus, $N_{ion} - N_{rec}$ can exceed unity.

Both 21cmFAST and our simulation code assume that hydrogen and single ionized helium have the same ionization fraction x_e. Ignoring helium recombination in equation (6.16) is indeed a good approximation given that photons produced by helium recombination have enough energy to ionize hydrogen.

We have checked this algorithm by solving the Strömgren sphere problem. Although this method to calculate the non-equilibrium ionization is relatively simple comparing the radiative transfer simulations, the error of the Strömgren radius is less than $\sim 10\%$.

Escape fraction of ionizing photons

Because the minimum mass of star forming haloes affects the escape fraction as we explained in the first part of this section, we here describe how to incorporate the M_{cool} dependence on the escape fraction $f_{esc}(z)$. The strategy is straightforward: since the escape fraction of an individual halo hosting Pop III stars, $f_{esc,ind}(M_h, M_s)$, is dependent on the halo mass, we take average of the individual escape fraction over all haloes whose mass is above the minimum halo mass M_{cool}, weighted by the halo mass function (HMF), $\frac{dn}{dM_h}$:

$$f_{esc} = \frac{\int_{M_{cool}}^{\infty} dM_h \frac{dn}{dM_h} f_{esc,ind}(M_h, M_s)}{\int_{M_{cool}}^{\infty} dM_h \frac{dn}{dM_h}}. \tag{6.17}$$

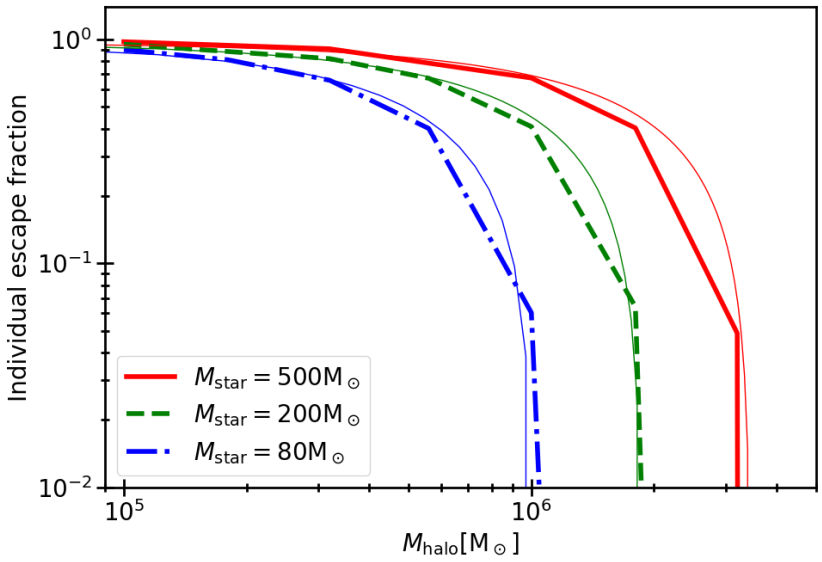

FIGURE 6.3: The individual escape fraction $f_{\rm esc,ind}$ at redshift 20 as a function of halo mass. The red solid line, the green dashed line, and blue dashed-dotted line are the cases of stellar mass of $M_{\rm s} = 500M_\odot$, $200M_\odot$, and $80M_\odot$, respectively. The thin lines are the fitted curves (equation 6.19).

For simplicity, we assume the single mass initial mass function of Pop III stars, that is, all stars have the same mass. Indeed the individual escape fraction depends on redshift, but the dependence is so small compared to dependences of stellar mass and halo mass that we ignore the redshift dependence in this work.

In order to obtain the HMF, we use the high-resolution N-body simulations (Ishiyama et al., 2016) in $(16{\rm Mpc}/h)^3$ box with 4096^3 dark matter particles. The gravitational softening length is 60 pc/h, the initial redshift is 127. We define haloes with the Friends-of-Friends (FoF) algorithm developed by Davis et al. 1985 with a linking parameter of $b = 0.2$. The minimum FoF halo mass is set to be $1.6 \times 10^5 {\rm M}_\odot/h$ being resolved by 32 particles.

We conduct series of RHD simulations which is described in Section 6.2.2 to obtain $f_{\rm esc,ind}$. Since the RHD simulation directly solves dynamics of the dense gas in a halo, we can trace the time-evolving gas density profile, which allows us to calculate the optical depth τ_ν at any stellar age of $t_{\rm age}$. Using the optical depth, the escape fraction at $t_{\rm age}$ can be written as,

$$\tilde{f}_{\rm esc,ind} = \frac{\int_{\nu_L}^{\infty} {\rm d}\nu \frac{L_\nu}{h\nu} \exp(-\tau_\nu(r_{\rm vir}))}{\int_{\nu_L}^{\infty} {\rm d}\nu \frac{L_\nu}{h\nu}} \tag{6.18}$$

where L_ν is specific luminosity of Pop III stars, $\nu_{\rm L}$ is the Lyman limit frequency, $r_{\rm vir}$ is the virial radius of the halo. We approximate the stellar spectrum as the black-body

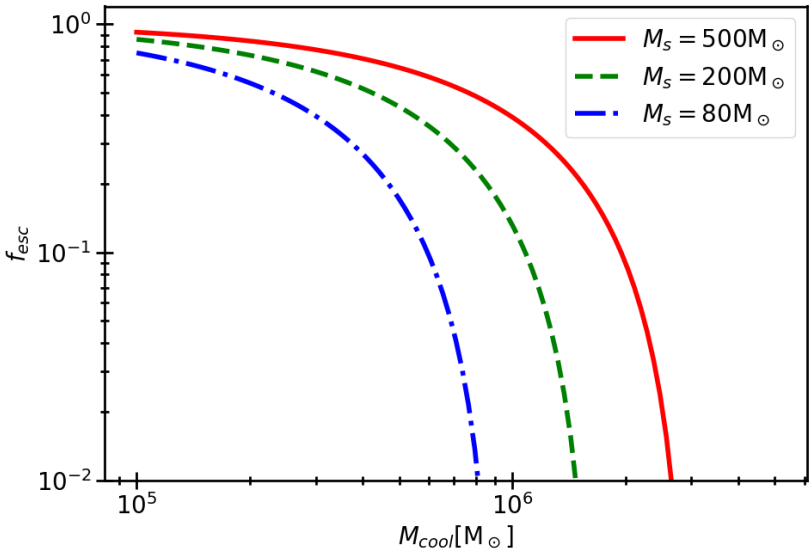

FIGURE 6.4: The escape fraction as a function of the minimum halo mass for star formation, $M_{\rm cool}$. The red solid line, the orange dashed line, and the blue dashed-dotted line are the cases of stellar mass of $M_{\rm s} = 500\mathrm{M}_\odot$, $200\mathrm{M}_\odot$, and $80\mathrm{M}_\odot$, respectively.

spectrum of the effective temperature of Pop III stars (Schaerer, 2002). Then, averaging $\tilde{f}_{\rm esc,ind}$ over the lifetime of the star, $t_{\rm life}$, gives $f_{\rm esc,ind} = \int_0^{t_{\rm life}} \tilde{f}_{\rm esc,ind} {\rm d}t_{\rm age}/t_{\rm life}$.

In Tanaka et al., 2018, the behavior of $f_{\rm esc,ind}$ is described in detail. Thus, we here show the halo mass dependence of the individual escape fraction in Figure 6.3. In the case of less massive haloes, the ionized bubble easily expands beyond the virial radius due to less amount of gas inside. Thus, soon after the Pop III star was born, the $f_{\rm esc,ind}$ becomes almost unity, resulting in a large $f_{\rm esc,ind}$. As the halo mass increases, more amount of gas prevents the ionized bubble from expanding, which keeps $f_{\rm esc,ind}$ small. Thus, in the cases of massive MHs ($M_{\rm h} \gtrsim$ a few $\times 10^6 \mathrm{M}_\odot$), the $f_{\rm esc,ind}$ remains nearly zero even at the end of the lifetime. Consequently the individual escape fraction is zero. By simulating in a wide range of parameter space, we develop useful fitting formula for $f_{\rm esc,ind}$ (Thin curves in Figure 6.3):

$$f_{\rm esc,ind} = {\rm MAX}\left\{-18.14 M_{\rm s}^{-0.67}\left(\frac{M_{\rm h}}{10^6[\mathrm{M}_\odot]}\right) + 0.97,\ 0\right\}. \tag{6.19}$$

The formula is valid with $M_{\rm h} > 10^5 \mathrm{M}_\odot$ and $M_{\rm s} = [40 - 500]\mathrm{M}_\odot$.

Now we see the $M_{\rm cool}$ dependence of the escape fraction $f_{\rm esc}$ in Figure 6.4. As the $M_{\rm cool}$ rises, the escape fraction falls. This is because the individual escape fraction is smaller for more massive haloes. The larger stellar mass of Pop III stars results in larger escape fraction due to the larger luminosity of ionizing photons which enable to ionize whole gas inside the halo within shorter timescale. We use the model of

escape fraction dependent on $M_{\rm cool}$ in our simulations.

6.3 Results1: The impact of our escape fraction model

We have done series of simulations, using our escape fraction model, to take into account the effect that the LW intensity affects minimum halo mass for star formation of Pop III stars. Also we investigate the effect of UV photo-heating on the 21-cm signal. All the results in this chapter are from simulations with boxes size of 512^3 Mpc^3, grid number of 512^3. The initial conditions are calculated with 1536^3 grids at redshift 300. The simulations starts from $z = 60$ when the star formation rate density of Pop III stars was too low to affect the ionization fraction of the Universe on cosmological scales. Since we investigate the impact of UV feedback on the cosmological 21-cm signal in this work, we turn off the X-ray heating so that we can obtain clear insights of UV photo-heating.

The parameters used in our simulations of this section are $N_{\rm UV} = 70000$, $f_* = 0.015$. With $f_* = 0.015$ resulting number of stars in MHs is less than the order of unity at maximum. As for Lyα coupling, we use the Pop III spectral models (Barkana and Loeb, 2005) prepared in the original 21cmFAST to calculate Lyα intensity.

We have conducted simulations with our escape fraction model with stellar mass of $M_{\rm s} = 500{\rm M}_\odot$, $200{\rm M}_\odot$, $80{\rm M}_\odot$, which are named as Run-Ms500, Run-Ms200, and Run-Ms80. In order to compare our model with the conventional constant escape fraction, we have also done simulations with the constant value of $f_{\rm esc} = 0.5$, named as Run-Fesc05.

In this section, we mainly investigate how our escape fraction model affects the 21-cm observable and several physical values such as ionization history and evolution of the SFRD, comparing with the conventional constant $f_{\rm esc}$ model, with same star formation efficiency f_*. While, in the next section, we discuss whether we can estimate the typical stellar mass of Pop III stars from the 21-cm signals.

6.3.1 Ionization history

First of all, we show how our escape fraction model impacts on the ionization history in Figure 6.5. To understand the ionization history, we plot the time evolution of the escape fraction and the LW intensity in Figure 6.6.

In our escape fraction models (Run-Ms500, Run-Ms200, and Run-Ms80), the LW intensity is so low at high redshift ($z \sim 40 - 60$) that the escape fraction is nearly unity. Therefore, the box-averaged ionization degree increases with growing star formation density, and is slightly larger than Run-Fesc05 owing to $f_{\rm esc} > 0.5$. Then, the growth of the LW intensity gradually halts the star formation in less massive haloes. As a result, the escape fraction drops sharply at $z \sim 28 - 35$ depending on

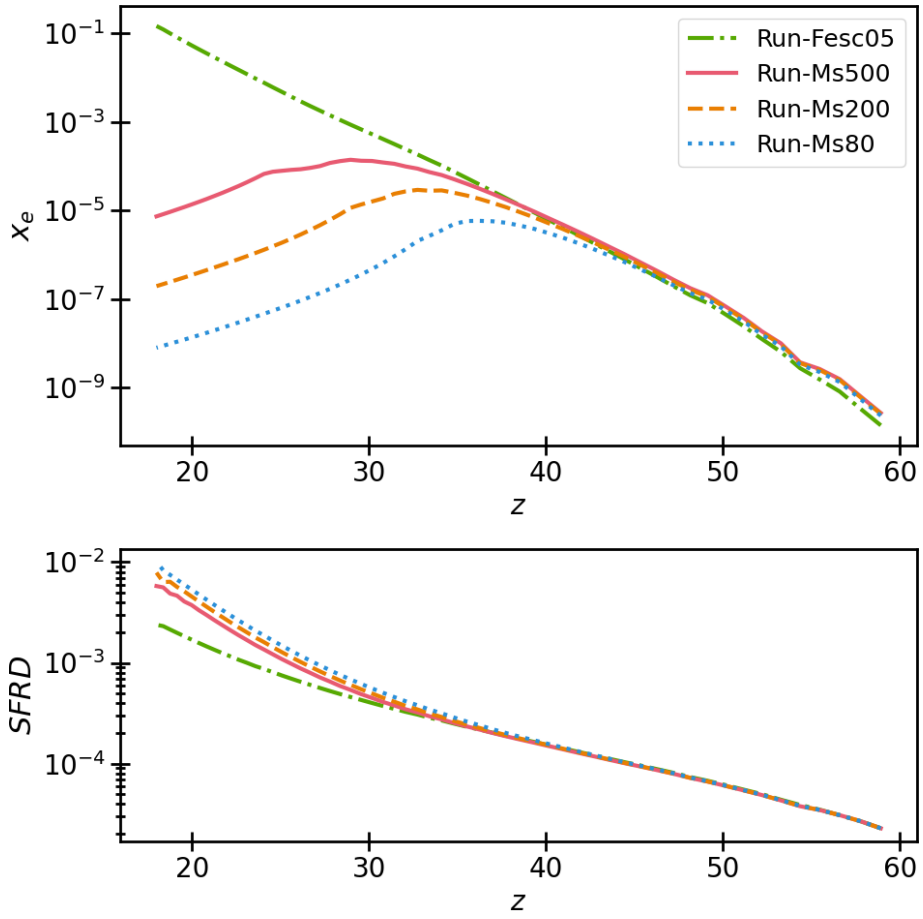

FIGURE 6.5: The box-averaged ionization fraction and SFRD [$M_\odot$/yr/Mpc^3] as a function of redshift. The red solid line, the orange dashed line, the blue dotted line, and the green dashed-dotted line are the cases of Run-Ms500, Run-Ms200, Run-Ms80, and Run-Fesc05, respectively.

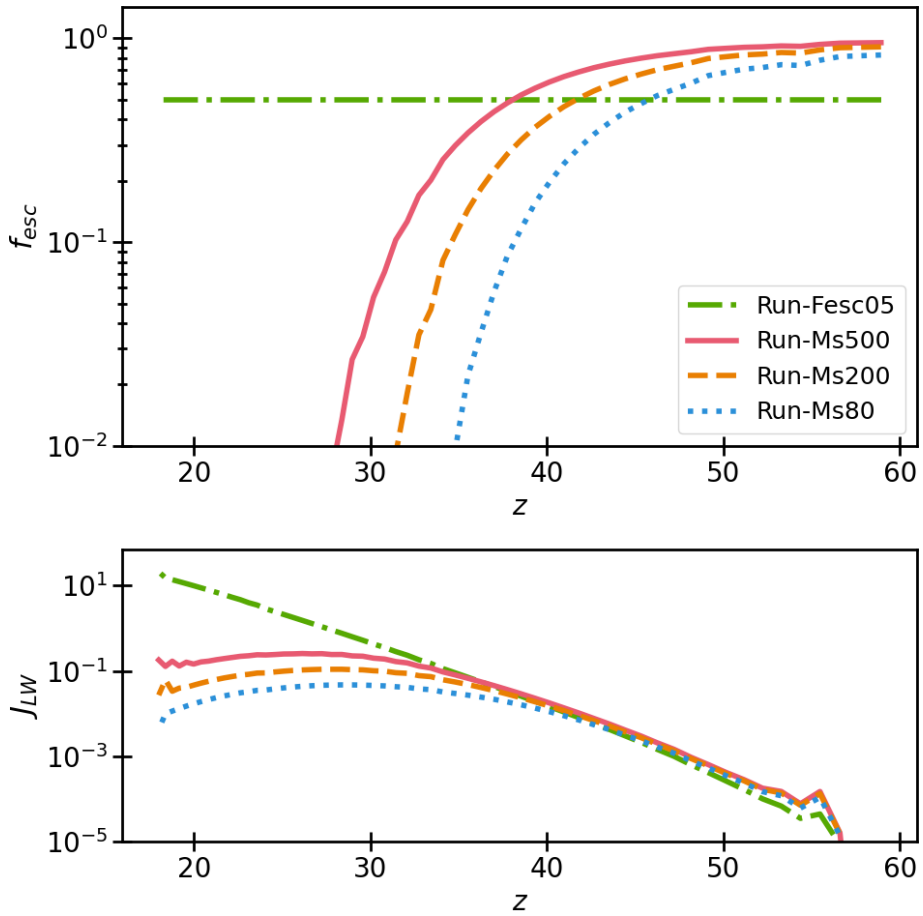

FIGURE 6.6: Top: The escape fraction dependent on the LW intensity as a function of redshift. The meaning of line types is the same as Figure 6.5. Bottom: The normalized LW intensity as a function of redshift.

the stellar mass. After the escape fraction drops, the LW intensity saturates. The saturated value of $J_{\rm LW}$ corresponds to $f_{\rm esc} \sim 0$. Consequently, the IGM is no longer irradiated with the ionizing photons from Pop III stars and the ionization fraction of the Universe turns over. Then, recombination slowly gets the ionization status of the Universe closer to neutral.

In Run-Fesc05, even though the LW intensity grows with time and boosts the $M_{\rm cool}$, more massive haloes than $M_{\rm cool}$ continue contributing to the reionization, resulting in the monotonic increase of ionization fraction, x_e.

The peak of x_e is only $\sim 10^{-4}$ even in the massive Pop III star case (Run-Ms500). The peak value is comparable with the fraction of the relic electrons. Thus, Pop III stars hardly contribute to the cosmic reionization. In other words, using constant escape fraction in time would result in an overestimation of the cosmic ionization fraction.

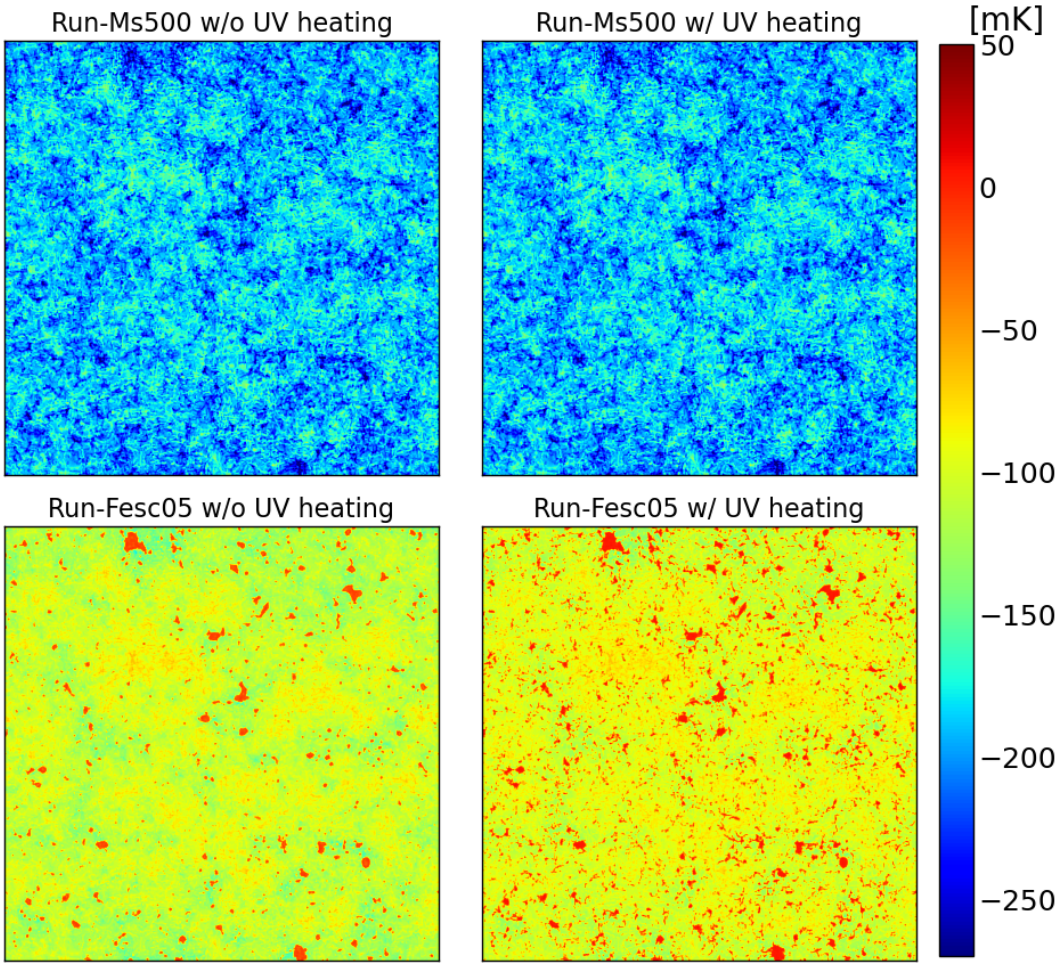

FIGURE 6.7: 2D slices of the 21-cm brightness temperature at redshift 20. The panels of left top and right top are with and without UV photo-heating in the case of Run-Ms500. The panels of left bottom and right bottom are with and without UV photo-heating in the case of Run-Fesc05. Each map is 512 Mpc on a side and the thickness is 1 Mpc. The box-averaged ionization fractions are $x_e \sim 1 \times 10^{-5}$ and $\sim 5 \times 10^{-2}$ in Run-Ms500 and Run-Fesc05.

6.3.2 21-cm brightness temperature

In this section, we show the results of 21-cm brightness temperature and describe how our models of escape fraction and UV photo-heating influence the 21-cm signal. As we see in Section 6.3.1, in our model with all stellar masses, the ionization fractions are low due to the decreasing escape fraction with time. Therefore, the stellar mass difference has only tiny impacts on the 21-cm signals indeed. Thus, in this section, we compare the results from Run-Ms500, which is on behalf of all the stellar mass cases, with that from Run-Fesc05.

In Figure 6.7, we show the 2D slices of the 21-cm brightness temperature field at $z = 20$. Until this redshift, the intensity of Lyman series photons become moderately strong: The box-averaged coupling coefficients are ~ 5.7 and 1.1 for Run-Ms500 and

Run-Fesc05, respectively. Therefore, the spin temperature gets decoupled from the CMB temperature especially at high-density regions, showing absorption or emission signal depending on the gas kinetic temperature. In Run-Ms500 without UV photo-heating, since the ionization fraction is small, we see deep absorption regions which is corresponding to the high-density regions where δ in equation 6.1 and x_α in equation 6.2 are large. The δT_b map of Run-Ms500 with UV photo-heating looks same as that without UV photo-heating, because the small ionization fraction means the small volume fraction of a heated region.

In Run-Fesc05, on the other hand, the ionization fraction is $x_e \sim 5\%$ so that we can see the ionized region as red-colored regions in the left bottom panel of Figure 6.7. Such ionized regions corresponds to again the high-density regions and have brightness temperature closer to zero ~ 0 [mK], because x_HI in equation 6.1 is small. When taking into account UV photo-heating in Run-Fesc05, δT_b is increased by the sub-grid-scale UV-heated regions. The increment depends on the ionization fraction of grids. As a result, the emission regions (Red regions in the right bottom panel of Figure 6.7) appear while the absorption signals are weakened. The reason why the average color of Run-Ms500 and Run-Fesc05 is different is that the strength of Lyα coupling is different.

We show the box-averaged 21-cm brightness temperature as the 21-cm global signal in Figure 6.8. In Run-Ms500, at high redshift ($z \gtrsim 40$), the density of the Universe is so high that the gas particle collisions effectively couple the spin temprature with the gas temperature which is colder than the CMB temperature, and therefore, the signal is absorption. As the Universe becomes diluted due to the Hubble expansion, the collisional coupling becomes weaker. Around $z = 30$, since the Lyman series photons emitted from Pop III stars start to be effectual, the global signal turns over, showing deeper absorption with time.

The differences appear at the deep absorption phase at lower redshift. The strength of Lyα coupling mainly determines the absorption depth because the ionization fraction is still small in all the models. Since the intensity of the dissociation photons is larger in Run-Fesc05, the less massive haloes cannot host stars so that the coupling is weaker than the other models. The differences among Run-Ms500, Run-Ms200, and Run-Ms80 are originated from the differences of SFRD (or J_LW). The less massive case produces deeper absorption signal due to smaller value of the escape fraction.

The effect of UV photo-heating appears when the ionization fraction is roughly more than 1%. In the case of Run-Fesc05, the curve with UV photo-heating starts separated from that without the heating around $z \sim 22$, and the difference becomes larger as the ionization fraction increases. In cases of Run-Ms500, Run-Ms200, and Run-Ms80, however, UV photo-heating does not have significant effect because the ionization fraction remains tiny.

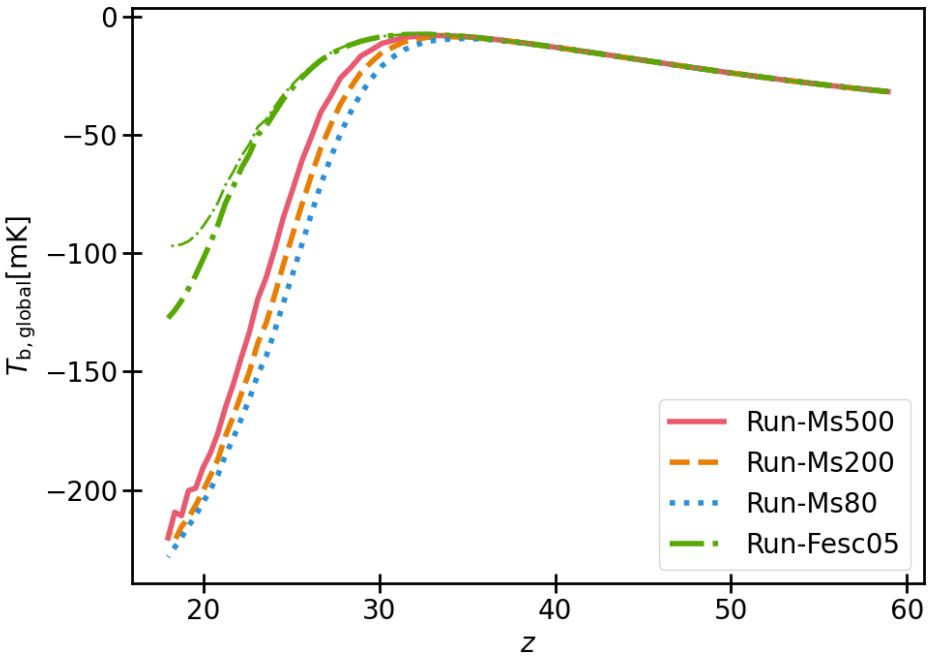

FIGURE 6.8: The box-averaged 21-cm brightness temperature as a function of redshift. The red solid line, the orange dashed line, the blue dotted line, and the green dashed-dotted line are the cases of Run-Ms500, Run-Ms200, Run-Ms80, and Run-Fesc05 without UV photo-heating, respectively. The thin green and thin red curves are the case of Run-Fesc05 and Run-Ms500 with UV photo-heating. Note that red thin and thick curves overlap each other.

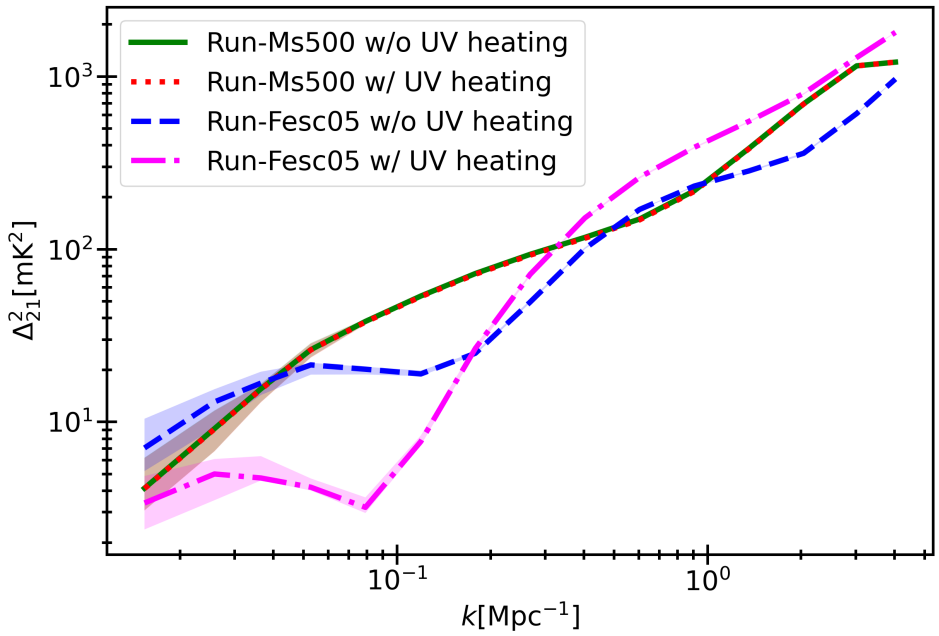

FIGURE 6.9: The power spectra of the 21-cm brightness temperature at redshift 20. The green solid and red dotted curves respectively indicate the results of Run-Ms500 without and with UV photo-heating. The blue dashed and magenta dashed-dotted curves are these of Run-Fesc05. The shaded regions correspond to the 10 - 90 percentiles obtained from 10 realizations each.

In Figure 6.9, we show the power spectra of 21-cm brightness temperature, $\Delta^2_{21}(k,z) \equiv \overline{\delta T_{\rm b}}^2(z)\,\langle|\delta_{21}(\mathbf{k},z)|^2\rangle k^3/(2\pi V)$, at $z=20$, where $\delta_{21}(\mathbf{x},z) \equiv [\delta T_{\rm b}(\mathbf{x},z) - \overline{\delta T}_{\rm b}(z)]/\overline{\delta T}_{\rm b}(z)$. The power spectrum of Run-Ms500 has relatively flat shape at the middle scale range ($k \sim 10^{-1} - 1$ [Mpc]$^{-1}$) and indicates the drop at larger scale ($k \lesssim 10^{-1}$ [Mpc]$^{-1}$), which is consistent with the results of Mesinger, Furlanetto, and Cen, 2011 when the Universe is neutral and Lyα coupling turns on. Since the ionization fraction is small, taking into account UV photo-heating does not affect the power spectrum as well as the 21-cm global signal.

The results of the Run-Fesc05 in which the ionization fraction is relatively large, on the other hand, slightly differ from that of Run-Ms500. Moreover, the Run-Fesc05 with UV photo-heating shows larger difference around at $k \sim 0.1$[Mpc^{-1}]. This suggests that if the Universe is slightly ionized, the power is about one order of magnitude smaller than the neutral case at the scale. By intensively analyzing simulation data, we find that when the ionization fraction is $x_e \gtrsim 1\%$, UV photo-heating has non-negligible impact on the 21-cm power spectrum.

6.4 Result2: Can we distinguish typical stellar mass from 21-cm signals?

I showed, in the previous section, how our escape fraction model impacts on the ionization history and 21-cm signals: For given star formation efficiency f_*, SFRD varies with different stellar mass because different escape fraction leads to different strength of the LW feedback. Additionally, Pop III stars do not contribute to the cosmic reionization indeed due to decreasing escape fraction as the LW feedback becomes strong. In this section, we discuss whether we can extract typical stellar mass of Pop III stars from 21-cm observations.

6.4.1 Modifying escape fraction model

If Pop III stars do not contribute to the reionization, we cannot distinguish different stellar mass from 21-cm signals. x_α depends on SFRD and not the stellar mass. The gas temperature does not depend typical stellar mass neither. Therefore, the brightness temperature is almost unchanged for different stellar mass of Pop III stars. To be strict, the saturated value of J_{21} depends on $M_{\rm s}$, but the differences on the 21-cm global signal is not large.

Do not Pop III stars really contribute to the reionization? The escape fraction would have larger values than that of our model indeed. We use spherically symmetric 1D RHD simulations, putting a single Pop III star at the center of haloes.

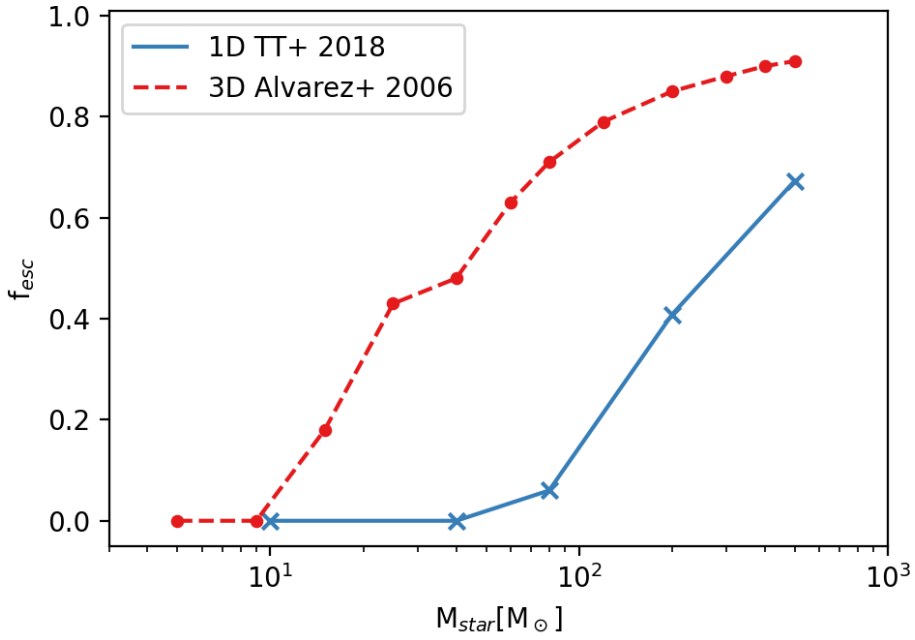

FIGURE 6.10: The individual escape fraction averaged over stellar lifetime depending on stellar mass. The blue solid line is the results with our 1D RHD simulations (Tanaka et al., 2018), the red dashed line is the results with 3D ray tracing simulation (Alvarez, Bromm, and Shapiro, 2006).

However, the 3D simulations taking into account the inhomogeneity of gas distribution show larger escape fraction.

For example, Yajima, Choi, and Nagamine, 2011 have conducted the post-process 3D RT simulations based on gas density distribution from cosmological simulations and derived escape fraction of high-z galaxies. Their results show the variation of the value of escape fraction ranging $f_{\rm esc} \sim [0-1]$. The variation is originated from gas density inhomogeneity in radial direction. Ionizing photons can escape more easily at the low-column-density direction and vice versa. Although they have investigated haloes with mass of $M_{\rm h} \geq 10^9 {\rm M}_\odot$, less massive MHs would have variety of $f_{\rm esc}$ values, and the averaged value would not be zero.

As another example, Alvarez, Bromm, and Shapiro, 2006 have conducted 3D ray-tracing calculation to investigate the evolution of ionization front with 3D gas distribution taken from cosmological simulation as initial condition. The resultant time-averaged escape fraction over stellar lifetime is shown in Figure 6.10, with halo mass of $10^6 {\rm M}_\odot$, at redshift 20. we overplot the results of our 1D simulations in the same figure. We see the 3D simulation tend to give larger values of escape fraction resulted from inhomogeneity of gas distribution.

The 3D calculation needs enormous computational cost, and therefore, modeling the escape fraction in the same manner as ours with 3D simulations is fairly difficult.

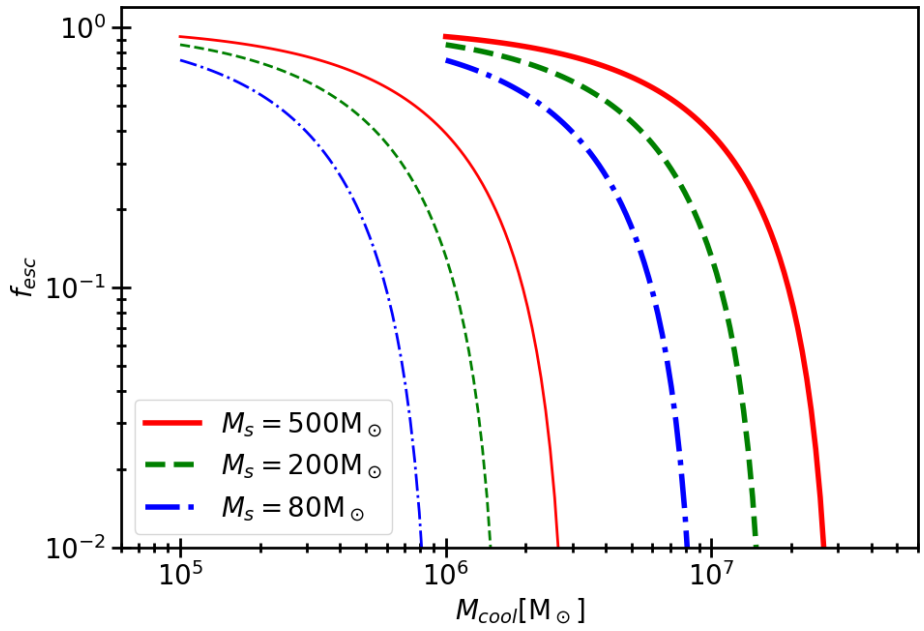

FIGURE 6.11: The thin curves are our escape fraction model developed with 1D RHD simulations, while the thick curves are the modified escape fraction model taking into account the 3D effect just by increasing the critical halo mass, at which the escape fraction drops nearly zero, for simplicity. The red solid, green dashed, and blue dotted-dashed curves means stellar mass of $500M_\odot$, $200M_\odot$, and $80M_\odot$.

Therefore, we take into account the "3D effect" just by increasing the critical halo mass, at which the escape fraction drops to nearly zero, for simplicity. We show our escape fraction model with $M_s = 500M_\odot$ and that with 10 times larger critical halo mass in Figure 6.11. We extrapolate in less massive range of halo mass where there are no data points, setting an upper limit of unity.

We conducted several simulations with the escape fraction model considering the 3D effect. In order to investigate the stellar mass dependence of 21-cm signals, we adjust the star formation efficiency f_* so that SFRDs at $z = 20$ are same in different stellar mass of Pop III stars: $f_* = 0.015$, 0.01328, and 0.01134 for $M_s = 500M_\odot$, $200M_\odot$, and $80M_\odot$. Apart from the escape fraction model and the star formation efficiency, the other parameters are the same as the simulations in the previous section. We name the simulations with stellar mass of $M_s = 500M_\odot$, $200M_\odot$, and $80M_\odot$ as Run-Ms500_Mc10x, Run-Ms200_Mc10x, and Run-Ms80_Mc10x.

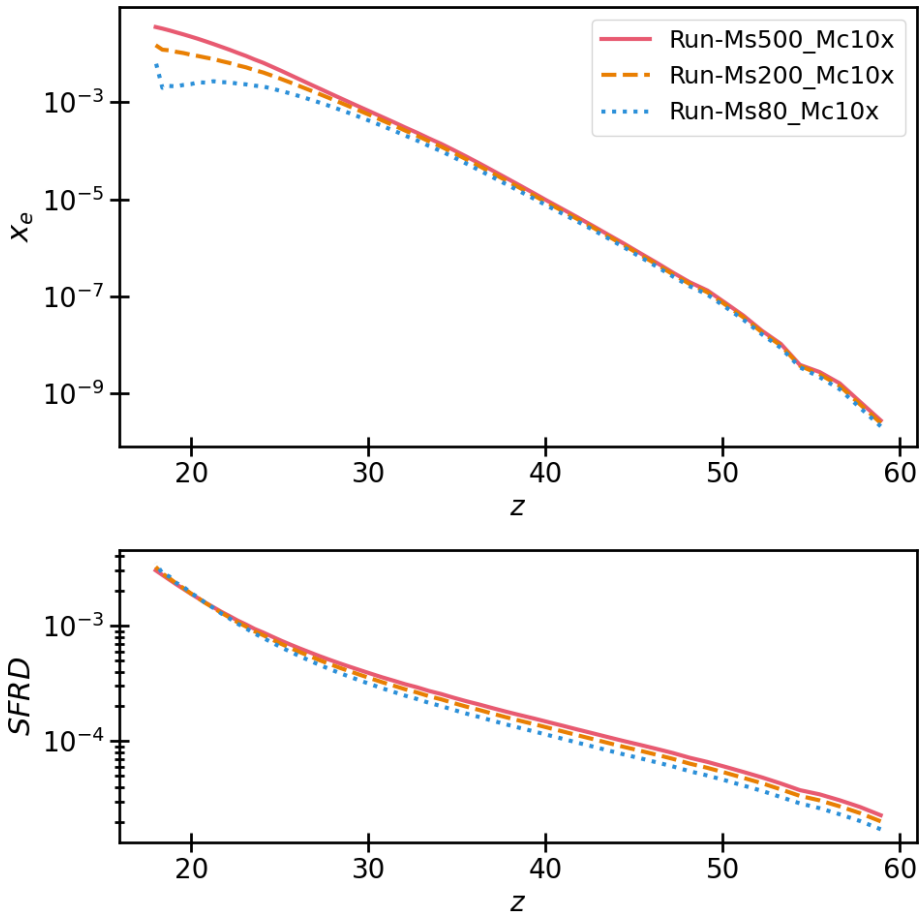

FIGURE 6.12: The box-averaged ionization fraction (top panel) and star formation rate density (bottom) as a function of redshift. The red solid, the orange dashed, and the blue dotted curves are the cases of Run-Ms500_Mc10x, Run-Ms200_Mc10x, and Run-Ms80_Mc10x5, respectively.

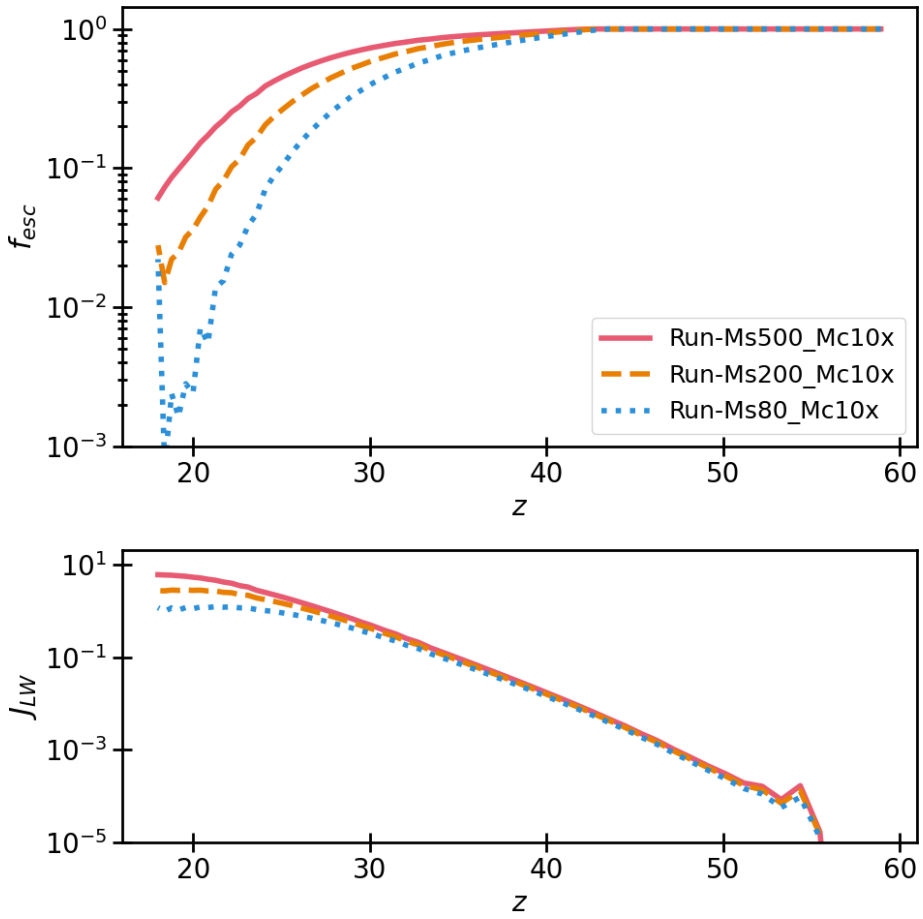

FIGURE 6.13: Top: The escape fraction dependent on the LW intensity as a function of redshift. Bottom: The normalized LW intensity as a function of The meaning of line types is the same as Figure 6.12.

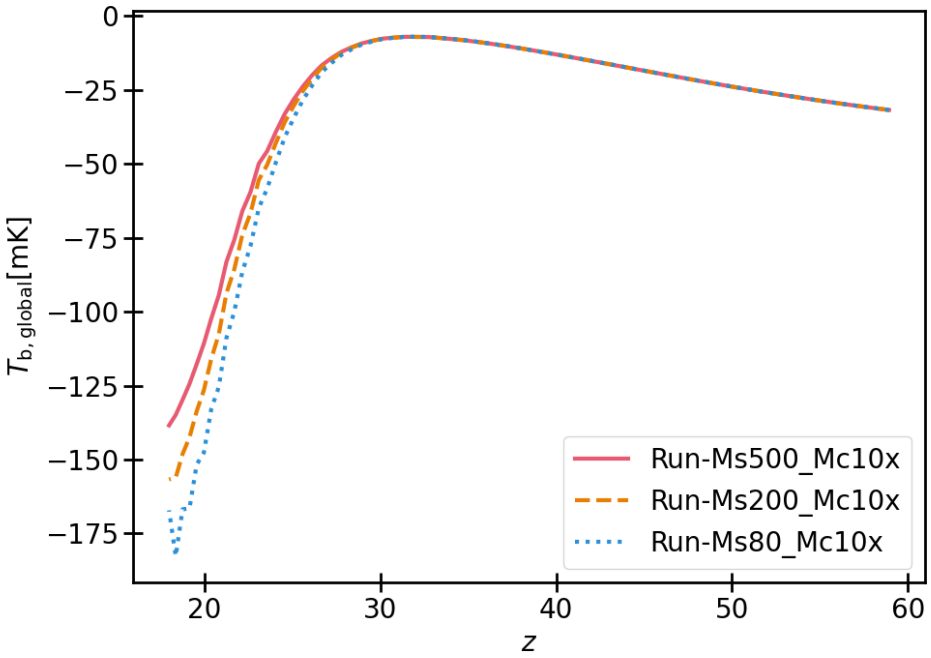

FIGURE 6.14: The box-averaged 21-cm brightness temperature considering UV photo-heating as a function of redshift. The red solid, orange dashed, and blue dotted-dashed curves are the results of Run-Ms500_Mc10x, Run-Ms200_Mc10x, and Run-Ms80_Mc10x.

6.4.2 Ionization history and 21-cm global signal including the 3D effect

The ionization history and SFRD are shown in Figure 6.12, and the escape fraction and the LW intensity are exhibited in Figure 6.13. The SFRD at redshift 20 are identical for different stellar mass cases. With the escape fraction model with the 3D effect, Pop III stars contribute to the reionization and ionization degree is different for different stellar mass. Since more massive Pop III stars lead to larger escape fraction, the ionization degree is larger. Resultant x_e at $z = 20$ are 2.3%, 1.0%, and 0.24% for Run-Ms500_Mc10x, Run-Ms200_Mc10x, and Run-Ms80_Mc10x.

The 21-cm global signal is shown in Figure 6.14. Even though the SFRD is identical with each other and the strength of the Lyα coupling is similar, the difference of ionization fraction results in different value of the global signal. Because $\delta T_{\rm b,gl} \propto (1 - x_e)(T_{\rm S} - T_{\rm CMB})/T_{\rm S}$, larger ionization degree in cases of more massive Pop III stars leads to shallower absorption signal. In addition, the larger x_e means more effective UV photo-heating so that the absorption becomes even shallower for massive Pop III cases. Consequently, the difference of the global signal between Run-Ms500_Mc10x and Run-Ms80_Mc10x at $z = 20$ is about 37 mK.

Because of the stellar mass dependence of the 21-cm global signal, if we can

estimate the SFRD with other observations, for example, the cosmic infrared background, we would be able to estimate the typical stellar mass of Pop III stars. However, without knowing the SFRD, the SFRD and Pop III stellar mass are indeed degenerated in the global signal. Thus, we need more information than the global signal to evaluate both the SFRD and the typical stellar mass, which is discussed in the next subsection.

6.4.3 Resolving degeneracy between stellar mass and SFRD

The 21-cm global signal has information on the SFRD and the typical stellar mass of Pop III stars. However, they degenerate: (1) SFRD is high and stellar mass is massive, which means higher ionization degree and more effective UV photo-heating and (2) SFRD is low and stellar mass is less massive. The two cases can have the same value of the 21-cm global signal. The result in Section 5.4 indicates the nature of degeneracy in the global signal as well.

We can indeed resolve the degeneracy utilizing the spatial fluctuation of 21-cm brightness temperature together with the 21-cm global signal. In this section, we simulate the degenerated case with stellar mass of $500\mathrm{M}_\odot$ and $80\mathrm{M}_\odot$ and show how the spatial fluctuation resolves the degeneracy.

We adjust the star formation efficiency $f_* = 0.0058$ for $M_\mathrm{s} = 80\mathrm{M}_\odot$ (namaed as Run-Ms80_Mc10x_2) so that the resultant global signal at redshift 20 becomes the same as Run-Ms500_Mc10x. The simulated ionization history and SFRD are shown in Figure 6.15, and the escape fraction and the intensity of LW radiation are exhibited in Figure 6.16. The resultant global signal is shown in Figure 6.17. We see that the global signal at redshift 20 equals each other, $\delta T_{\mathrm{b,global}} \sim -111$ mK.

The stellar mass dependence indeed appears on the evolution of the global signal. However, the IMF of Pop III stars can be different at different redshift. For example, Hirano et al., 2015 shows the Pop III.2 stars which form under the influence of UV radiation background tend to be more massive than the Pop III.1 stars which form not being affected UV radiation. Since the UV radiation background evolves with time, the IMF of Pop III stars can evolve as well. Therefore, we would like to estimate both the SFRD and the typical stellar mass from the 21-cm signal at a particular redshift.

Now we see the spatial distribution of the 21-cm brightness temperature in Figure 6.18. The right two figures are the 2D map of δT_b with UV photo-heating. The both have the same averaged value of ~ -111 mK, but clearly the contrast is different: in the case of Run-Ms500_Mc10x, the emission signals emerge from the UV heated regions (Red regions in top right panel), on the other hand, the result of Run-Ms80_Mc10x_2 exhibits less area of UV heated regions. Also the Lyα coupling is

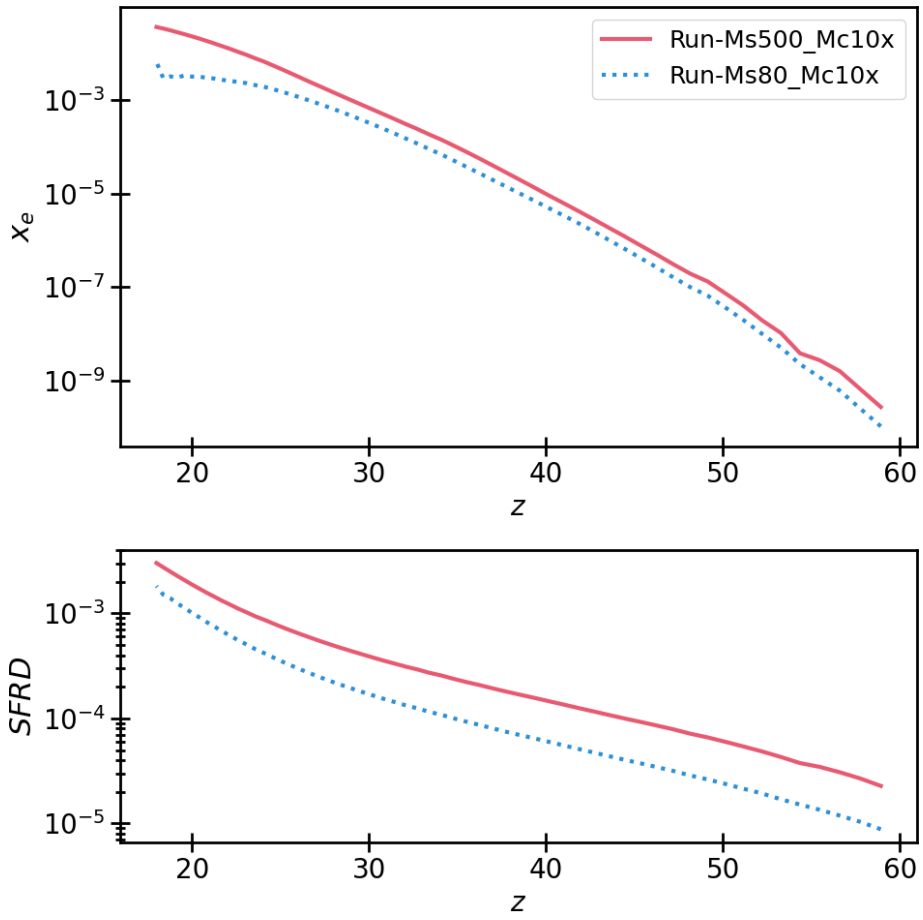

FIGURE 6.15: The box-averaged ionization fraction (top panel) and SFRD [$M_\odot$/yr/Mpc^3] (bottom) as a function of redshift. The red solid and the blue dotted curves are the cases of Run-Ms500_Mc10x, and Run-Ms80_Mc10x_2, respectively.

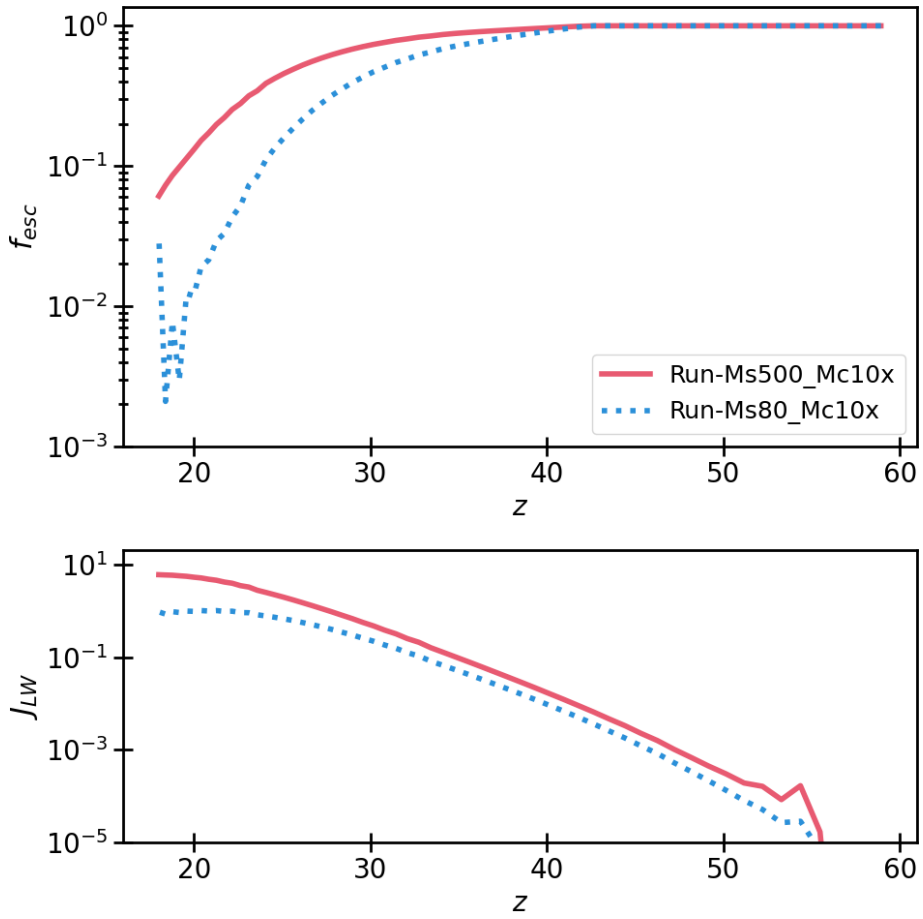

FIGURE 6.16: Top: The escape fraction dependent on the LW intensity as a function of redshift. Bottom: The normalized LW intensity as a function of The meaning of line types is the same as Figure 6.15.

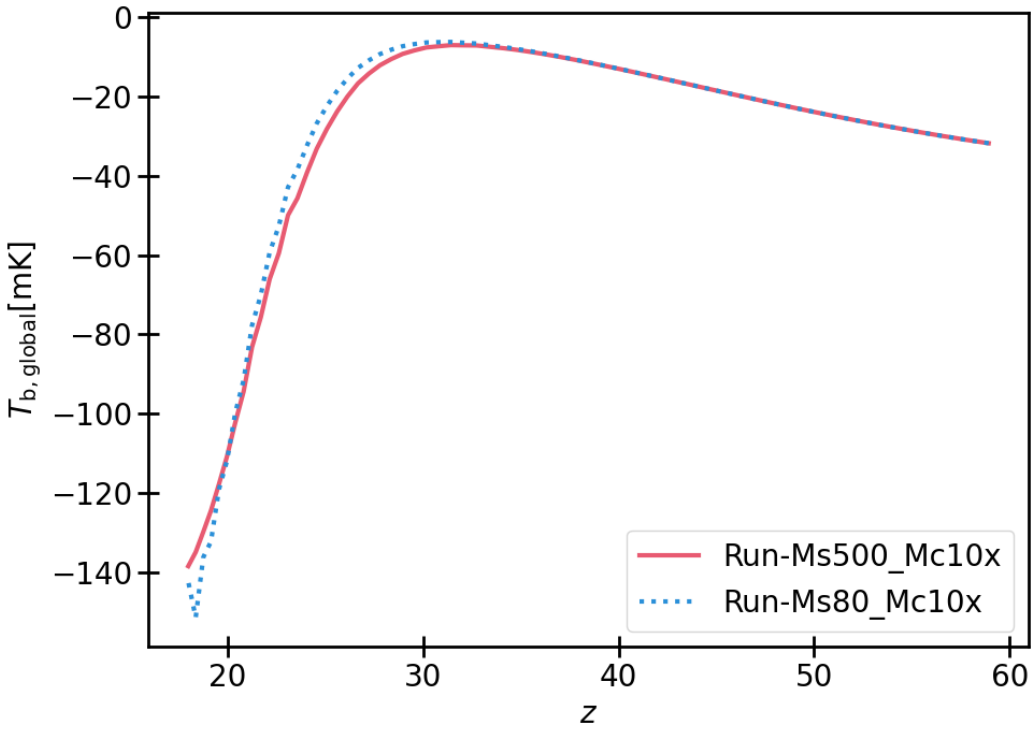

FIGURE 6.17: The box-averaged 21-cm brightness temperature considering UV photo-heating as a function of redshift. The red solid and blue dotted-dashed curves are the results of Run-Ms500_Mc10x and Run-Ms80_Mc10x_2.

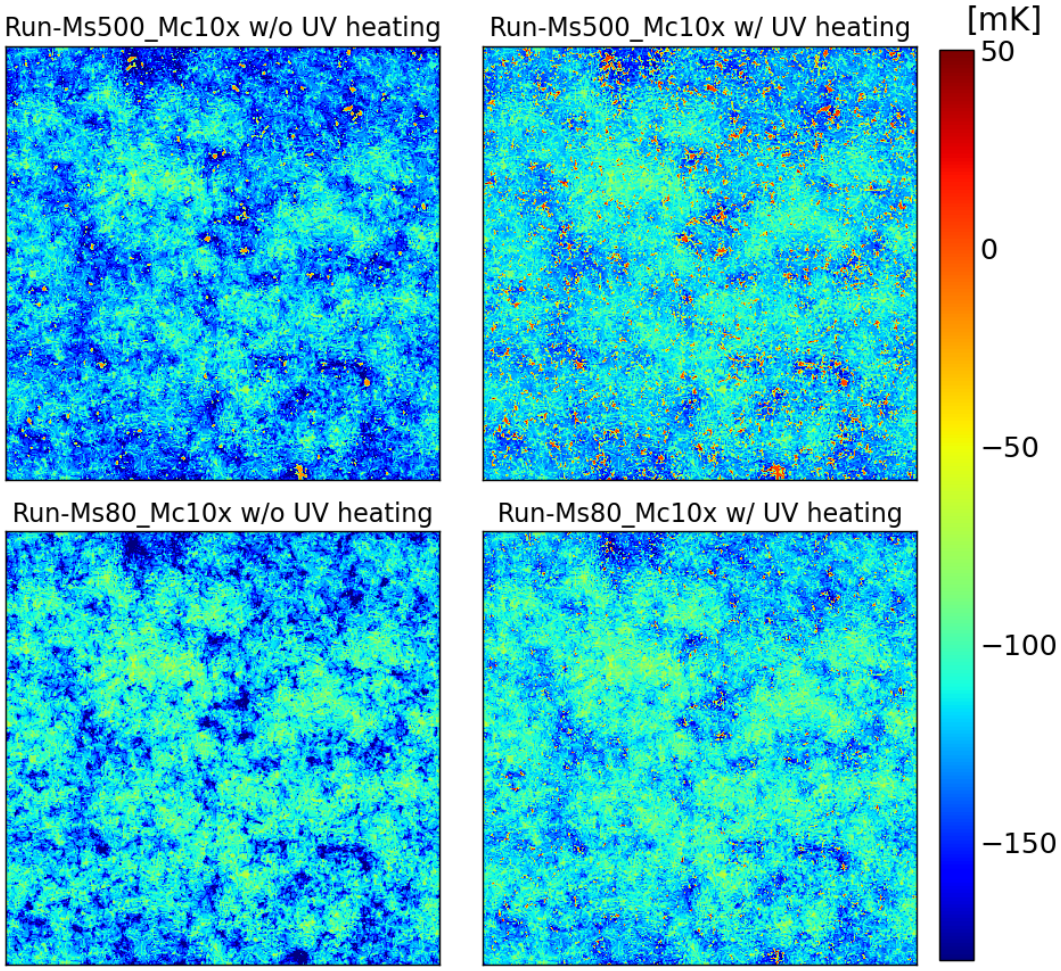

FIGURE 6.18: 2D slices of the 21-cm brightness temperature at redshift 20. The panels of left top and right top are with and without UV photo-heating in the case of Run-Ms500_Mc10x. The panels of left bottom and right bottom are with and without UV photo-heating in the case of Run-Ms80_Mc10x_2. Each map is 512 Mpc on a side and the thickness is 1 Mpc. The box-averaged ionization fractions are $x_e \sim 2.3\%$ and $\sim 0.3\%$ in Run-Ms500_Mc10x and Run-Ms80_Mc10x_2.

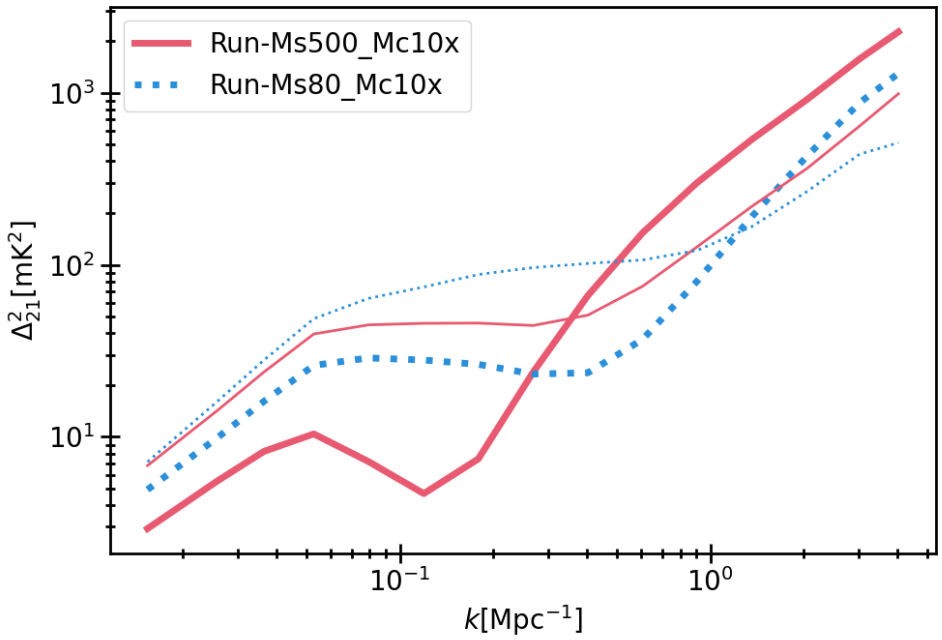

FIGURE 6.19: The power spectra of the 21-cm brightness temperature at redshift 20. The red solid and the blue dotted curves are Run-Ms500_Mc10x and Run-Ms80_Mc10x_2. The thick and thin curves are with and without UV photo-heating.

different, $x_\alpha = 1.45$ and 1.19 for Run-Ms500_Mc10x and Run-Ms80_Mc10x_2. Therefore, the δT_b contrast of Run-Ms500_Mc10x is stronger than that of Run-Ms80_Mc10x_2.

The difference of the contrast appears on the power spectrum shown in Figure 6.19. Without UV photo-heating, the power spectra are relatively similar to each other whose difference is originated mainly from the Lyα radiation and ionization fraction. Once we take into account UV photo-heating, the difference becomes larger especially at the scale of $k \sim 0.1$ Mpc^{-1}. UV photo-heating decreases the power at large scales. Since the ionization fraction of Run-Ms500_Mc10x is larger than that of Run-Ms80_Mc10x_2 so that the influence of UV photo-heating and the resulting drop of power is larger. Therefore, even if SFRD and typical stellar mass degenerate in the 21-cm global signal, we can resolve the degeneracy with spatial distribution of δT_b and its power spectrum.

We note that we need to improve the foreground removal model or other innovative ideas to reduce error of the global signal and the power spectrum in order to estimate SFRD and Pop III stellar mass from the 21-cm observations.

6.4.4 Application for arbitrary IMF

In all the simulations until here, we approximate IMF assuming that all Pop III stars have the same mass (single-mass IMF). But, our model of escape fraction can be

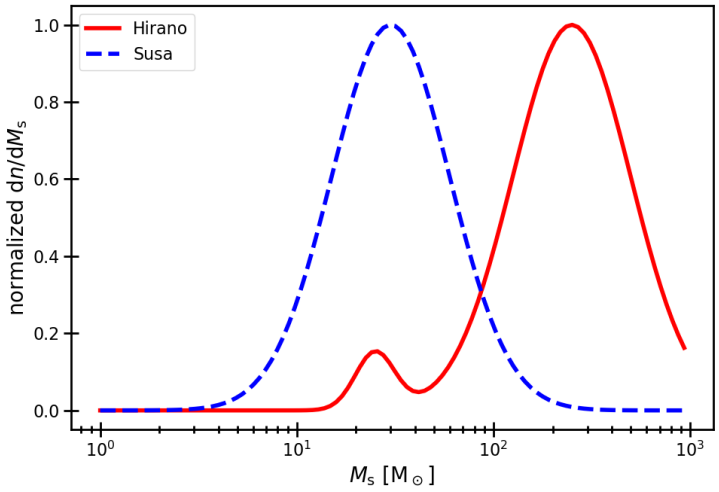

FIGURE 6.20: Normalized IMFs mimicking the IMFs obtained in Hirano et al., 2015 (red solid curve) and Susa, Hasegawa, and Tominaga, 2014 (blue dashed curve).

easily extended to arbitrary IMF as long as the individual escape fraction for the mass range of the IMF is available. In this section, we demonstrate the extension.

We create two IMFs in such a way that the shapes become similar to the IMFs obtained in the simulations of Hirano et al., 2015 and Susa, Hasegawa, and Tominaga, 2014 (See Figure 3.4 and Figure 3.3).

$$\frac{\mathrm{d}n_{\mathrm{Hirano}}}{\mathrm{d}M_{\mathrm{s}}} = \exp\left\{-\frac{(\log M_{\mathrm{s}} - \log 250)^2}{2\times 0.3^2}\right\} + \frac{3}{20}\exp\left\{-\frac{(\log M_{\mathrm{s}} - \log 25)^2}{2\times 0.1^2}\right\}, \quad (6.20)$$

$$\frac{\mathrm{d}n_{\mathrm{Susa}}}{\mathrm{d}M_{\mathrm{s}}} = \exp\left\{-\frac{(\log M_{\mathrm{s}} - \log 30)^2}{2\times 0.3^2}\right\}, \quad (6.21)$$

where the unit of M_{s} is solar mass. The Hirano IMF (equation 6.20) is modeled as the summation of two Gaussian distributions. The first and second peaks are at $250\mathrm{M}_{\odot}$ and $25\mathrm{M}_{\odot}$. On the other hand, the Susa IMF (equation 6.21) is expressed as a single Gaussian whose peak is at $30\mathrm{M}_{\odot}$. Both IMFs are normalized at the position of the first peak. The variances are chosen so that the shapes become similar to the original IMFs obtained with the numerical simulations. The two IMFs are shown in Figure 6.20.

To obtain the escape fraction model with the IMFs (equation 6.20 and 6.21), we replace $f_{\mathrm{esc,ind}}(M_{\mathrm{h}}, M_{\mathrm{s}})$ in equation 6.17 with $f_{\mathrm{esc,IMF}}(M_{\mathrm{h}})$:

$$f_{\mathrm{esc,IMF}}(M_{\mathrm{h}}) = \frac{\int \mathrm{d}M_{\mathrm{s}} \frac{\mathrm{d}n_{\mathrm{IMF}}}{\mathrm{d}M_{\mathrm{s}}} f_{\mathrm{esc,ind}}(M_{\mathrm{h}}, M_{\mathrm{s}})}{\int \mathrm{d}M_{\mathrm{s}} \frac{\mathrm{d}n_{\mathrm{IMF}}}{\mathrm{d}M_{\mathrm{s}}}}, \quad (6.22)$$

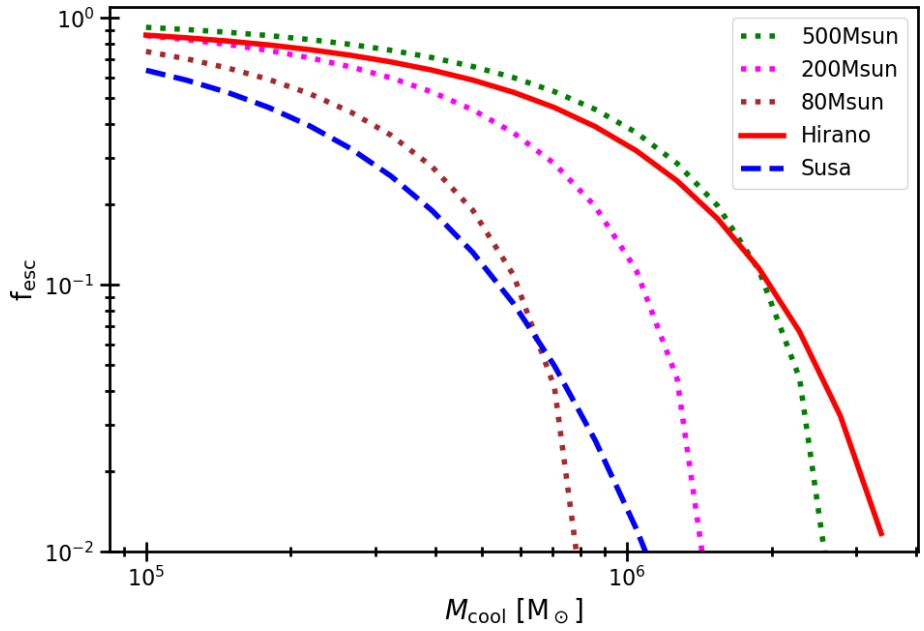

FIGURE 6.21: The escape fraction as a function of the minimum halo mass for star formation, $M_{\rm cool}$. The red solid and the blue dashed curves are Hirano and Susa models. The dotted curves are the single-mass IMF models for $M_{\rm s} = 500{\rm M}_\odot$ (green), $200{\rm M}_\odot$ (magenta) $80{\rm M}_\odot$ (brown), respectively.

where $\frac{{\rm d}n_{\rm IMF}}{{\rm d}M_{\rm s}}$ is $\frac{{\rm d}n_{\rm Hirano}}{{\rm d}M_{\rm s}}$ or $\frac{{\rm d}n_{\rm Susa}}{{\rm d}M_{\rm s}}$. We use the fitting formula (equation 6.19) for the individual escape fraction. We again neglect the redshift dependence because it is much smaller than halo mass and stellar mass dependences in relevant redshift range (Section 6.2.4).

Then, we obtain the escape fraction model, that is, escape fraction depending on the minimum halo mass for star formation, which is shown in Figure 6.21. In the cases of the single-mass IMF, once the $M_{\rm cool}$ goes beyond the critical halo mass, at which the individual escape fraction for the single stellar mass sharply drops, the escape fraction drops sharply as well (the dotted curves in Figure 6.21). In the cases of the Hirano and Susa IMFs, on the other hand, even though the LW feedback increases, massive stars can still provide ionizing photons into IGM. As a result, the shape becomes flatter than the case of single IMF.

With the escape fraction models with the Hirano and the Susa IMFs, we conducted simulations, taking into account the 3D effect. We choose the star formation efficiency so as to fix SFRD at redshift 20: $f_* = 0.015$ and 0.1172 for the Hirano IMF and the Susa IMF, respectively. These runs are named as Run-Hirano_Mc10x and Run-Susa_Mc10x. The other parameters are adapted from the simulations in previous sections.

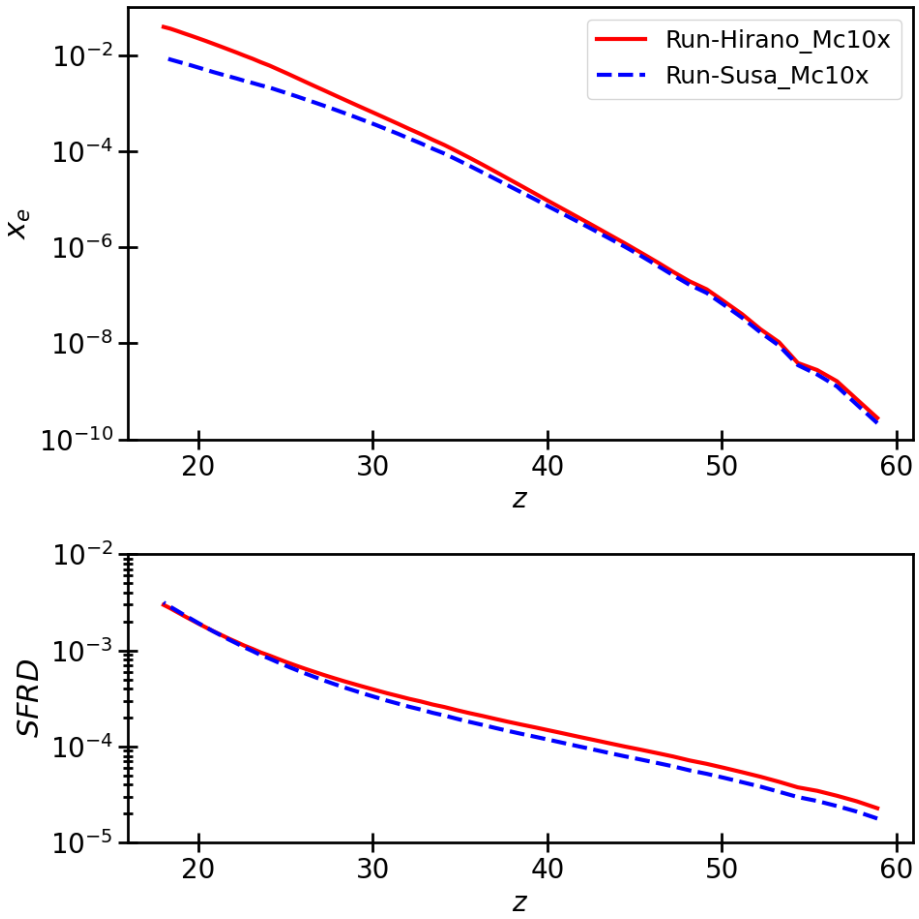

FIGURE 6.22: The box-averaged ionization fraction and SFRD as a function of redshift. The red solid and the blue dashed curves are the cases of Run-Hirano_Mc10x and Run-Susa_Mc10x, respectively.

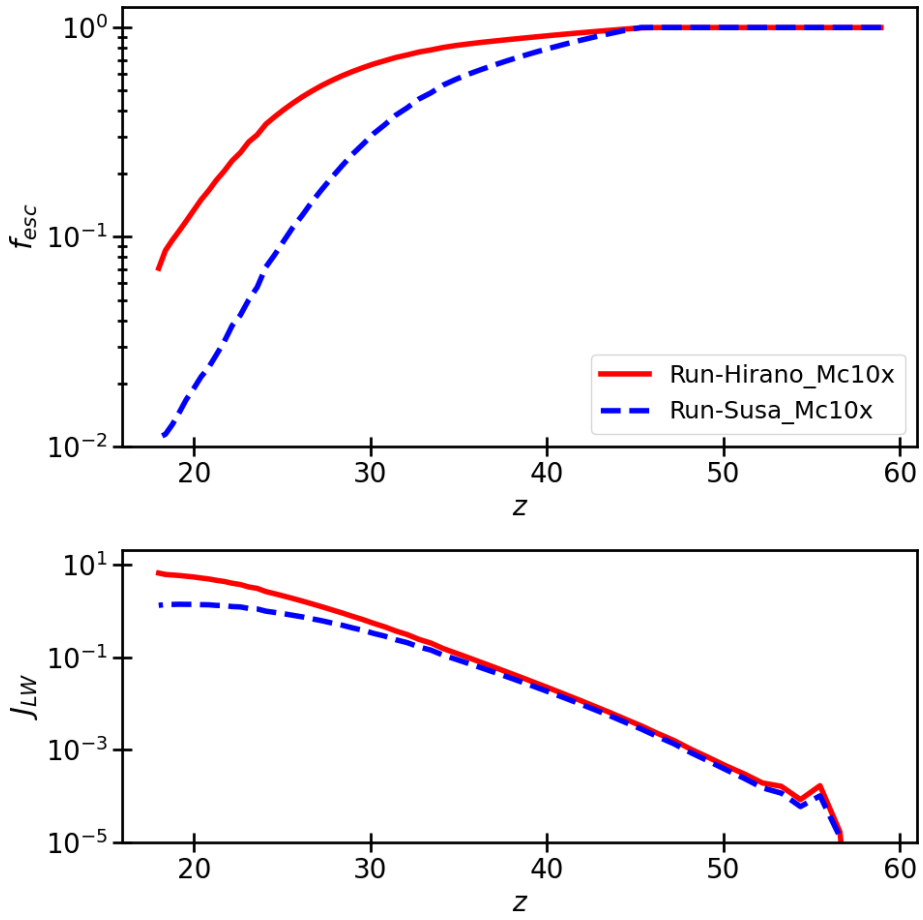

FIGURE 6.23: Top: The escape fraction dependent on the LW intensity as a function of redshift. Bottom: The normalized LW intensity as a function of redshift. The red solid and the blue dashed curves are the cases of Run-Hirano_Mc10x and Run-Susa_Mc10x, respectively.

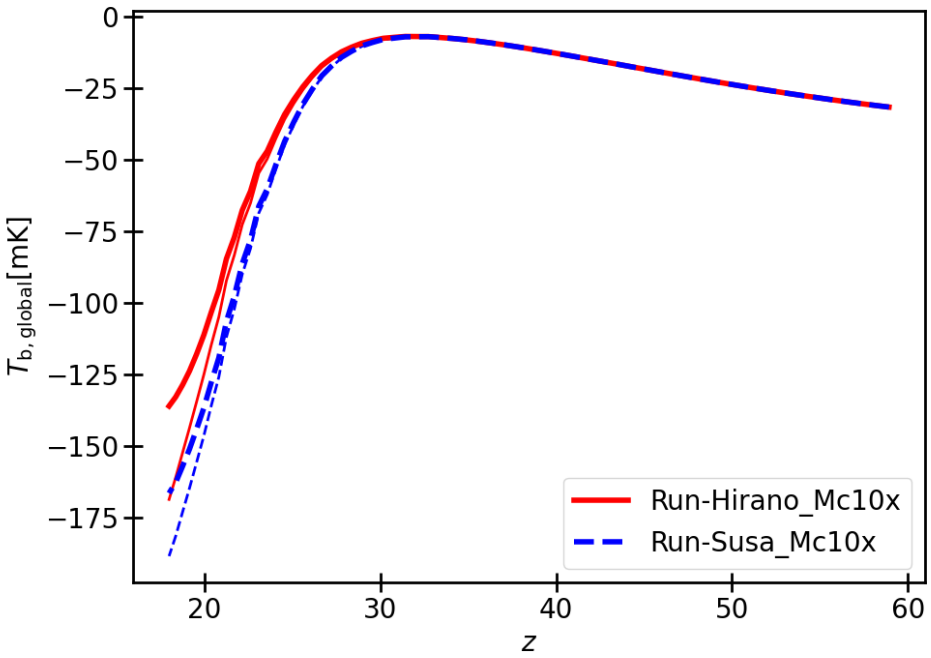

FIGURE 6.24: The box-averaged 21-cm brightness temperature as a function of redshift. The red solid and the blue dashed curves are the cases of Run-Hirano_Mc10x and Run-Susa_Mc10x, respectively. The thick and thin curves are the cases with and without UV photo-heating.

Figure 6.22 shows the time evolution of ionization fraction and SFRD, and Figure 6.23 shows the time evolution of escape fraction and LW intensity. In Run-Hirano_Mc10x, since the typical stellar mass of the Hirano IMF is massive, the escape fraction is larger. As a result, the ionization fraction increases at higher rate compared with the case of Run-Susa_Mc10x. The ionization fraction at $z = 20$ is 2.2% and 0.6% for Run-Hirano_Mc10x and Run-Susa_Mc10x.

The 21-cm global signal is shown in Figure 6.24. Because the ionization fraction is higher in Run-Hirano_Mc10x, the ionization and UV photo-heating make the absorption signal shallow to greater extent than Run-Susa_Mc10x. The 21-cm global signal with UV photo-heating at $z = 20$ is -111 mK and -137 mK for Run-Hirano_Mc10x and Run-Susa_Mc10x. Figure 6.25 shows the 21-cm power spectrum. When considering UV photo-heating, the slope becomes steeper compared to the case without UV photo-heating. The power at $k = 0.12$ Mpc^{-1} is 4.57 and 14.2 for Run-Hirano_Mc10x and Run-Susa_Mc10x.

As we demonstrate in this section, it is easy to model escape fraction with arbitrary shape of IMF and investigate how IMFs impact on the reionization history and the 21-cm signals.

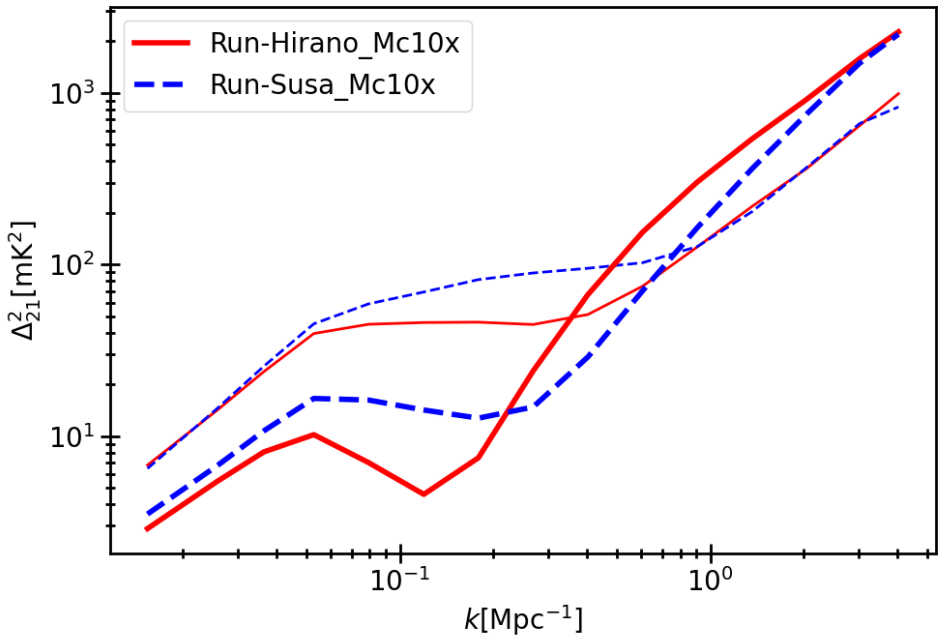

FIGURE 6.25: The power spectra of the 21-cm brightness temperature at redshift 20. The red solid and the blue dashed curves are the cases of Run-Hirano_Mc10x and Run-Susa_Mc10x, respectively. Thick and thin curves mean the result with UV photo-heating and that without UV photo-heating.

6.5 Discussion

In this work, we use the box-averaged LW intensity and single value of escape fraction at each redshift, however, the LW intensity can fluctuate largely (Ahn et al., 2009), which may have not a little impact on the escape fraction and the 21-cm signals. At high density regions, the LW intensity rises earlier than the average and the escape fraction falls toward zero, while, the low density region can remain low-intensity levels in which less massive haloes, whose escape fraction is large, can still form stars and possibly contribute to reionization. Thus, we incorporate the inhomogeneous LW feedback in future study.

In our escape fraction model, we assume that one MH does not host more than one Pop III star. However, recent states-of-arts simulations show the wide variation about the multiplicity of the Pop III star formation. Some simulations (e.g. Greif et al., 2012; Machida and Doi, 2013; Hirano and Bromm, 2017) suggest the multiple star formation. In the accretion disk around the protostar, the fragmentation produces multiple clumps. Such clumps would end up as a group of stars. However, Hosokawa et al., 2016 reported that such clumps eventually merge onto the central protostar, and as a result, single massive star forms at the center. Although these results have not yet converged, it would be worth studying 21-cm signals with models

assuming the multiple star formation in which stellar properties like typical stellar mass, stellar lifetime, and spectral hardness are different.

Although investigating other heating sources with UV photo-heating is beyond the scope of this work, studying the X-ray heating together with UV photo-heating is necessary. Pop III stars would end up as high mass X-ray binaries (HMXBs) which are often presumed to be dominant X-ray source at high redshift (Fragos et al., 2013). Such early X-ray photons can heat (and also ionize) the gas enough to largely affect the 21-cm signals (e.g. Fialkov, Barkana, and Visbal, 2014). Since the mean free path of X-ray is much longer than that of UV, the different fluctuation scale of gas heating would help us distinguish the two types of heating (see Das et al. 2017 as example of different scale of 21-cm fluctuations originated from mean free path difference). Thus, we are planing to investigate the 21-cm power spectrum and its time evolution with both the UV and X-ray heatings in our future work.

6.6 Summary of this chapter

We have conducted the semi-numerical simulations which for the first time account for time-evolving escape fraction reflecting the boosted minimum halo mass for star formation by the LW negative feedback. Additionally, we have developed a new method to take into account UV photo-heating, which has ever been neglected, on the calculation of the cosmological 21-cm signal by utilizing the 1D RHD simulations. With the simulations, we study how the time-evolving escape fraction and UV photo-heating affect on the ionization history and cosmological 21-cm signals at high redshift, and investigate whether we can estimate SFRD and typical stellar mass of Pop III stars, focusing on the epoch when the Pop III star formation dominates the other stellar populations.

The results show that the escape fraction of MHs decreases with time as the LW intensity grows and prevents less massive haloes, from which most ionizing photons escape, from continuing star formation. With the escape fraction model with 1D RHD simulation, the escape fraction fraction drops to nearly zero $z = 28$-35 depending on the stellar mass of Pop III stars, and as a result, the ionization fraction of the Universe stops increasing. This picture is different from that with a constant escape fraction which is conventionally assumed in reionization and 21-cm simulations.

The differences of ionization history modify the deepness of the absorption in the 21-cm global signal. Comparing the result with the constant escape fraction model, the absorption bottom of the global signal becomes deeper in the case of time-evolving escape fraction because high-density regions are observed as deep absorption instead of zero-signal ionized region. When accounting for UV photo-heating,

in all the places where the ionization fraction is not zero, the 21-cm brightness temperature increases. Therefore, the global 21-cm signal is more closer to zero than the case without UV photo-heating. We found that the impact on UV photo-heating on the global signal is comparable to that of the ionization.

We simulate the Universe and calculate 21-cm signals with escape fraction considering the gas density inhomogeneity just by increasing the critical halo mass for simplicity as well. In these simulations, Pop III stars contribute to the cosmic reionization and the 21-cm signals exhibit the stellar mass dependence. Even though the SFRD and the typical mass of Pop III stars degenerate in the 21-cm global signal, the case with more massive stars show stronger contrast of the 21-cm brightness temperature. The difference also appears in the 21-cm power spectrum. Although we need to improve the foreground removal technique to precisely observe the 21-cm signals, we found that the SFRD and the typical stellar mass of Pop III stars can be estimated from high-z 21-cm signals, in principle.

Our results indicate the importance of studying the escape fraction of MHs in more detail with three-dimensional simulations taking into account the gas density inhomogeneity, and investigating whether Pop III stars contribute to the reionization or not. Moreover, UV photo-heating is also needed to be studied in more detail together with the X-ray heating.

Chapter 7

Summary and Conclusion

In this final chapter, I summarize the thesis followed by the general conclusion. The future prospects are also mentioned.

The dynamical evolution of the Universe is well described by the flat lambda model with precisely constrained cosmological parameters by, for example, the CMB observations (Chapter 2). The structure formation in the Universe such as stars and galaxies roots in the initial tiny fluctuations in early Universe which grows due to the gravitational instability. Although Pop III stars, which is made of the pristine metal-free gas, have important roles in the history of the Universe, the results of the theoretical works investigating their properties have not yet converged (Chapter 3). As for observations, the neutral hydrogen 21-cm line emission and absorption have a potential to reveal the nature of Pop III stars because it should reflect the properties, even though the foreground removal is challenging (Chapter 4).

The theoretical models, which connect the 21-cm observables and the properties of Pop III stars, are needed to further proceed our understanding with current and future 21-cm observations. I with collaborators investigate the profile of 21-cm brightness temperature around an individual Pop III star in detail by developing and conducting the radiative hydrodynamics simulations. We find that the gas dynamics plays an essential role: In early phase, the ionized region is well confined in the halo so that the deep absorption region is seen around the central star, and then in late phase, the ionized region goes beyond the halo radius letting the absorption signal weaker. Also we revel the stellar mass, halo mass and redshift dependences of the time evolution of the 21-cm signal profile (Chapter 5).

We study not only the small scale signal around Pop III stars but also the cosmological scale signal. We have developed and conducted the cosmological 21-cm semi-numerical simulation for the first time considering the UV photo-heating and time-evolving escape fractions of ionizing photons and H_2 dissociation photons self-consistently with the LW negative feedback on star formation. We developed two models of the escape fraction: One is modeled with 1D RHD simulation (fesc1D model), and the other simply takes into account the effect of 3D gas distribution (fesc3D model). What we find is that, in the case with fesc1D model, Pop III stars

hardly contribute to the cosmic reionization because the LW feedback halts the star formation in less massive haloes whose escape fraction is large. Consequently, the global signal is about twice stronger than that with the constant escape fraction which is conventionally used. However, if Pop III stars do not contribute to the reionization, the 21-cm signals reflect only SFRD, but do not inform us of the typical stellar mass of Pop III stars. On the other hand, the fesc3D model lets Pop III stars contribute to the reionization in which we can distinguish both the typical mass of Pop III stars and the SFRD from the 21-cm global signal and the power spectrum under the assumption that the formation of Pop III stars dominates that of other populations and X-ray heating can be neglected (Chapter 6).

Through our works, we conclude that the 21-cm signals are significantly important to proceed our understanding of Pop III stars because the observations of the 21-cm global signal and the power spectrum possibly enable us to estimate the SFRD and the typical stellar mass of Pop III stars.

Although we yield new knowledge and perspectives about 21-cm signals originated from Pop III stars, there are still room for improvement such as modeling the escape fraction more accurately with 3D simulations, considering the inhomogeneity of the LW radiation background, and so forth. In addition, installing the X-ray heating together with the UV photo-heating is needed because the effectiveness of the X-ray heating is still highly uncertain.

Improving theoretical works, including our works, step by step together with the current and forthcoming 21-cm observations may clarify the properties of Pop III stars at some future time. The perspectives of the high-redshift Universe is also supposed to contribute to the understanding of the lower-redshift Universe as well as the opposite way. I would like to expect that our efforts summarized in the thesis finally contribute to the ultimate goals of cosmology and astronomy which is to completely grasp the whole history of the Universe.

Acknowledgements

First of all, I would like to express my sincere gratitude to Professor Naoshi Sugiyama for supporting my six years in the Cosmology group, and even beyond the laboratory he gave me a lot of chances to mature thorough variety of experiences in Toryumon. I would like to appreciate my supervisor Kiyotomo Ichiki who always provide with practical advice for proceeding my research and motivate me. I cannot show enough gratitude to Kenji Hasegawa who mainly supervised me and helped me to take every single step to produce the research achievements. Also I have the great honor of collaborating with Hidenobu Yajima who gave professional comments on my research progress every time which drastically proceeded my study.

I would like to appreciate all the other current and former C-lab faculty members: Takahiko Matsubara, Hiroyuki Tashiro, Atushi J. Nishizawa, Shuichiro Yokoyama, Sachiko Kuroyanagi, Hironao Miyatake, Takeshi Kobayashi, Yuko Urakawa, Naoya Kitajima, Atsushi Nishizawa, Jean-Baptiste Durrive, Daisuke Nitta, Daichi Kashino, Tada Yuichiro, Tomomi Sunayama, and Shogo Masaki.

I would like to thank the students of C-lab and other laboratory nearby, especially my current and former C-lab colleagues: Teppei Minoda, Minoguchi Mutsumi, Ryo Iida, Taichi Takeuchi, Takumi Sumida.

I have honor of belonging to the PhD Professional Toryumon, The Program for Leading Graduate Schools led by Ministry of Education, Culture, Sports, Science, and Technology. Through the wide variety of experiences and interaction with people in various fields, I improved skills and accumulated knowledge which will surely be strong advantages in my future. I would like to thank the involved teachers, stuffs, and all the colleagues in the program.

I financially supported as the Research Fellowship for Young Scientists led by Japan Society for the Promotion of Science and by the Toryumon program. The supports enabled me not only to focus on my study but also to present my research achievement and to discuss with other researchers all over the world.

I finally, but most importantly, appreciate my parents for the understanding to study in the PhD course in Nagoya University, the financial support, and all the love they gave me. Also, I thank my brother for spending enjoyable time and sometime giving great advice getting the point. And, I am genuinely grateful toward my wife who always supports me mentally and provide practical advice from the view point of the different field. If even one of these is missing, I would not be able to finish my PhD course. I am so proud of myself living my life with these wonderful and great people.

Bibliography

Abel, T., G. L. Bryan, and M. L. Norman (Jan. 2002). "The Formation of the First Star in the Universe". In: *Science* 295, pp. 93–98. DOI: 10.1126/science.295.5552.93. eprint: astro-ph/0112088.

Ahn, Kyungjin et al. (Apr. 2009). "The Inhomogeneous Background Of H_2-Dissociating Radiation During Cosmic Reionization". In: *The Astrophysical Journal* 695.2, pp. 1430–1445. DOI: 10.1088/0004-637X/695/2/1430. arXiv: 0807.2254 [astro-ph].

Ahn, Kyungjin et al. (Sept. 2012). "Detecting the Rise and Fall of the First Stars by Their Impact on Cosmic Reionization". In: *The Astrophysical Journal Letters* 756.1, L16, p. L16. DOI: 10.1088/2041-8205/756/1/L16. arXiv: 1206.5007 [astro-ph.CO].

Ahn, Kyungjin et al. (Mar. 2015). "Spatially Extended 21 cm Signal from Strongly Clustered Uv and X-Ray Sources in the Early Universe". In: *The Astrophysical Journal* 802.1, 8, p. 8. DOI: 10.1088/0004-637X/802/1/8. arXiv: 1405.2085 [astro-ph.CO].

Alvarez, M. A., V. Bromm, and P. R. Shapiro (Mar. 2006). "The H II Region of the First Star". In: *The Astrophysical Journal* 639, pp. 621–632. DOI: 10.1086/499578. eprint: astro-ph/0507684.

Alvarez, Marcelo A., John H. Wise, and Tom Abel (Aug. 2009). "Accretion onto the First Stellar-Mass Black Holes". In: *The Astrophysical Journal Letters* 701.2, pp. L133–L137. DOI: 10.1088/0004-637X/701/2/L133. arXiv: 0811.0820 [astro-ph].

Bañados, E. et al. (July 2014). "Discovery of Eight z ~ 6 Quasars from Pan-STARRS1". In: *The Astronomical Journal* 148, 14, p. 14. DOI: 10.1088/0004-6256/148/1/14. arXiv: 1405.3986.

Barkana, Rennan (Mar. 2018). "Possible interaction between baryons and dark-matter particles revealed by the first stars". In: *nature* 555.7694, pp. 71–74. DOI: 10.1038/nature25791. arXiv: 1803.06698 [astro-ph.CO].

Barkana, Rennan and Abraham Loeb (June 2005). "Detecting the Earliest Galaxies through Two New Sources of 21 Centimeter Fluctuations". In: *The Astrophysical Journal* 626.1, pp. 1–11. DOI: 10.1086/429954. arXiv: astro-ph/0410129 [astro-ph].

Bowman, J. D. et al. (Mar. 2018). "An absorption profile centred at 78 megahertz in the sky-averaged spectrum". In: *nature* 555, pp. 67–70. DOI: 10.1038/nature25792.

Bromm, V., P. S. Coppi, and R. B. Larson (Jan. 2002). "The Formation of the First Stars. I. The Primordial Star-forming Cloud". In: *The Astrophysical Journal* 564, pp. 23–51. DOI: 10.1086/323947. eprint: astro-ph/0102503.

Bullock, J. S. et al. (Mar. 2001). "Profiles of dark haloes: evolution, scatter and environment". In: *Monthly Notices of the Royal Astronomical Society* 321, pp. 559–575. DOI: 10.1046/j.1365-8711.2001.04068.x. eprint: astro-ph/9908159.

Chen, X. and J. Miralda-Escudé (Feb. 2004). "The Spin-Kinetic Temperature Coupling and the Heating Rate due to Lyα Scattering before Reionization: Predictions for 21 Centimeter Emission and Absorption". In: *Astrophysical Journal* 602, pp. 1–11. DOI: 10.1086/380829. eprint: astro-ph/0303395.

— (Sept. 2008). "The 21 cm Signature of the First Stars". In: *The Astrophysical Journal* 684, 18-33, pp. 18–33. DOI: 10.1086/528941. eprint: astro-ph/0605439.

Clark, Paul C. et al. (Feb. 2011). "The Formation and Fragmentation of Disks Around Primordial Protostars". In: *Science* 331.6020, p. 1040. DOI: 10.1126/science.1198027. arXiv: 1101.5284 [astro-ph.CO].

Das, Arpan et al. (July 2017). "High-mass X-ray binaries and the cosmic 21-cm signal: impact of host galaxy absorption". In: *Monthly Notices of the Royal Astronomical Society* 469.1, pp. 1166–1174. DOI: 10.1093/mnras/stx943. arXiv: 1702.00409 [astro-ph.CO].

Feng, Chang and Gilbert Holder (May 2018). "Enhanced Global Signal of Neutral Hydrogen Due to Excess Radiation at Cosmic Dawn". In: *The Astrophysical Journal* 858.2, L17, p. L17. DOI: 10.3847/2041-8213/aac0fe. arXiv: 1802.07432 [astro-ph.CO].

Fialkov, Anastasia, Rennan Barkana, and Eli Visbal (Feb. 2014). "The observable signature of late heating of the Universe during cosmic reionization". In: *nature* 506.7487, pp. 197–199. DOI: 10.1038/nature12999. arXiv: 1402.0940 [astro-ph.CO].

Fialkov, Anastasia et al. (July 2013). "The 21-cm signature of the first stars during the Lyman-Werner feedback era". In: *Monthly Notices of the Royal Astronomical Society* 432.4, pp. 2909–2916. DOI: 10.1093/mnras/stt650. arXiv: 1212.0513 [astro-ph.CO].

Field, G. B. (Jan. 1958). "Excitation of the Hydrogen 21-CM Line". In: *Proceedings of the IRE* 46, pp. 240–250. DOI: 10.1109/JRPROC.1958.286741.

Fragos, T. et al. (Feb. 2013). "X-Ray Binary Evolution Across Cosmic Time". In: *The Astrophysical Journal* 764.1, 41, p. 41. DOI: 10.1088/0004-637X/764/1/41. arXiv: 1206.2395 [astro-ph.HE].

Fukugita, M. and M. Kawasaki (Aug. 1994). "Reionization during Hierarchical Clustering in a Universe Dominated by Cold Dark Matter". In: *Monthly Notices of the Royal Astronomical Society* 269, p. 563. DOI: 10.1093/mnras/269.3.563. eprint: astro-ph/9309036.

Furlanetto, S. R. (Sept. 2006). "The global 21-centimeter background from high redshifts". In: *Monthly Notices of the Royal Astronomical Society* 371, pp. 867–878. DOI: 10.1111/j.1365-2966.2006.10725.x. eprint: astro-ph/0604040.

Furlanetto, S. R. and A. Loeb (Nov. 2002). "The 21 Centimeter Forest: Radio Absorption Spectra as Probes of Minihalos before Reionization". In: *Astrophysical Journal* 579, pp. 1–9. DOI: 10.1086/342757. eprint: astro-ph/0206308.

Furlanetto, S. R. and S. P. Oh (Dec. 2006). "Redshifted 21 cm Emission from Minihalos before Reionization". In: *The Astrophysical Journal* 652, pp. 849–856. DOI: 10.1086/508448. eprint: astro-ph/0604080.

Furlanetto, S. R., S. P. Oh, and F. H. Briggs (Oct. 2006). "Cosmology at low frequencies: The 21 cm transition and the high-redshift Universe". In: *Physics Reports* 433, pp. 181–301. DOI: 10.1016/j.physrep.2006.08.002. eprint: astro-ph/0608032.

Furlanetto, S. R. and J. R. Pritchard (Nov. 2006). "The scattering of Lyman-series photons in the intergalactic medium". In: *Monthly Notices of the Royal Astronomical Society* 372, pp. 1093–1103. DOI: 10.1111/j.1365-2966.2006.10899.x. eprint: astro-ph/0605680.

Furlanetto, S. R. et al. (2009). "Astrophysics from the Highly-Redshifted 21 cm Line". In: *astro2010: The Astronomy and Astrophysics Decadal Survey*. Vol. 2010. ArXiv Astrophysics e-prints. arXiv: 0902.3011 [astro-ph.CO].

Galli, D. and F. Palla (July 1998). "The chemistry of the early Universe". In: *Astronomy and Astrophysics* 335, pp. 403–420. eprint: astro-ph/9803315.

Gao, L. et al. (June 2007). "The first generation of stars in the Λ cold dark matter cosmology". In: *Monthly Notices of the Royal Astronomical Society* 378, pp. 449–468. DOI: 10.1111/j.1365-2966.2007.11814.x. eprint: astro-ph/0610174.

Greif, Thomas H. et al. (Aug. 2011). "Simulations on a Moving Mesh: The Clustered Formation of Population III Protostars". In: *Astrophysical Journal* 737.2, 75, p. 75. DOI: 10.1088/0004-637X/737/2/75. arXiv: 1101.5491 [astro-ph.CO].

Greif, Thomas H. et al. (July 2012). "Formation and evolution of primordial protostellar systems". In: *Monthly Notices of the Royal Astronomical Society* 424.1, pp. 399–415. DOI: 10.1111/j.1365-2966.2012.21212.x.

Hasegawa, K. and M. Umemura (Oct. 2010). "START: smoothed particle hydrodynamics with tree-based accelerated radiative transfer". In: *Monthly Notices of the Royal Astronomical Society* 407, pp. 2632–2644. DOI: 10.1111/j.1365-2966.2010.17100.x. arXiv: 1005.5312 [astro-ph.IM].

Hasegawa, K., M. Umemura, and T. Kitayama (Aug. 2009). "Formation of globular clusters induced by external ultraviolet radiation". In: *Monthly Notices of the Royal Astronomical Society* 397, pp. 1338–1347. DOI: 10.1111/j.1365-2966.2009.15103.x. arXiv: 0905.2247.

Heger, A. and S. E. Woosley (Mar. 2002). "The Nucleosynthetic Signature of Population III". In: *Astrophysical Journal* 567, pp. 532–543. DOI: 10.1086/338487. eprint: astro-ph/0107037.

Hirano, S. et al. (Mar. 2015). "Primordial star formation under the influence of far ultraviolet radiation: 1540 cosmological haloes and the stellar mass distribution". In: *Monthly Notices of the Royal Astronomical Society* 448, pp. 568–587. DOI: 10.1093/mnras/stv044. arXiv: 1501.01630.

Hirano, Shingo and Volker Bromm (Sept. 2017). "Formation and survival of Population III stellar systems". In: *Monthly Notices of the Royal Astronomical Society* 470.1, pp. 898–914. DOI: 10.1093/mnras/stx1220. arXiv: 1612.06387 [astro-ph.GA].

Hosokawa, Takashi et al. (June 2016). "Formation of Massive Primordial Stars: Intermittent UV Feedback with Episodic Mass Accretion". In: *The Astrophysical Journal* 824.2, 119, p. 119. DOI: 10.3847/0004-637X/824/2/119. arXiv: 1510.01407 [astro-ph.GA].

Huterer, Dragan and Daniel L. Shafer (Jan. 2018). "Dark energy two decades after: observables, probes, consistency tests". In: *Reports on Progress in Physics* 81.1, 016901, p. 016901. DOI: 10.1088/1361-6633/aa997e. arXiv: 1709.01091 [astro-ph.CO].

Ishiyama, Tomoaki et al. (July 2016). "Where are the Low-mass Population III Stars?" In: *The Astrophysical Journal* 826.1, 9, p. 9. DOI: 10.3847/0004-637X/826/1/9. arXiv: 1602.00465 [astro-ph.GA].

Johnson, J. L., T. H. Greif, and V. Bromm (Aug. 2007). "Local Radiative Feedback in the Formation of the First Protogalaxies". In: *The Astrophysical Journal* 665, pp. 85–95. DOI: 10.1086/519212. eprint: astro-ph/0612254.

Karlsson, T., V. Bromm, and J. Bland-Hawthorn (Apr. 2013). "Pregalactic metal enrichment: The chemical signatures of the first stars". In: *Reviews of Modern Physics* 85, pp. 809–848. DOI: 10.1103/RevModPhys.85.809. arXiv: 1101.4024.

Kauffmann, G., S. D. M. White, and B. Guiderdoni (Sept. 1993). "The formation and evolution of galaxies within merging dark matter haloes." In: *Monthly Notices of the Royal Astronomical Society* 264, pp. 201–218. DOI: 10.1093/mnras/264.1.201.

Kitayama, T. and N. Yoshida (Sept. 2005). "Supernova Explosions in the Early Universe: Evolution of Radiative Remnants and the Halo Destruction Efficiency". In: *Astrophysical Journal* 630, pp. 675–688. DOI: 10.1086/432114. eprint: astro-ph/0505368.

Kitayama, T. et al. (June 2000). "Radiation-hydrodynamical collapse of pre-galactic clouds in the ultraviolet background". In: *Monthly Notices of the Royal Astronomical Society* 315, pp. L1–L7. DOI: 10.1046/j.1365-8711.2000.03589.x. eprint: astro-ph/0004060.

Kitayama, T. et al. (Oct. 2001). "Criteria for the formation of Population III objects in the ultraviolet background radiation". In: *Monthly Notices of the Royal Astronomical Society* 326, pp. 1353–1366. DOI: 10.1111/j.1365-2966.2001.04669.x.

Kitayama, T. et al. (Oct. 2004). "The Structure and Evolution of Early Cosmological H II Regions". In: *The Astrophysical Journal* 613, pp. 631–645. DOI: 10.1086/423313. eprint: astro-ph/0406280.

Kuhlen, M., P. Madau, and R. Montgomery (Jan. 2006). "The Spin Temperature and 21 cm Brightness of the Intergalactic Medium in the Pre-Reionization era". In: *Astrophysical Journal* 637, pp. L1–L4. DOI: 10.1086/500548. eprint: astro-ph/0510814.

Li, Y. et al. (Aug. 2007). "Formation of z˜6 Quasars from Hierarchical Galaxy Mergers". In: *Astrophysical Journal* 665, pp. 187–208. DOI: 10.1086/519297. eprint: astro-ph/0608190.

Liszt, H. (June 2001). "CO J = 3-2 mapping of the molecular circumnuclear disk in Centaurus A". In: *Astronomy and Astrophysics* 371, pp. 865–874. DOI: 10.1051/0004-6361:20010443.

Machacek, Marie E., Greg L. Bryan, and Tom Abel (Feb. 2001). "Simulations of Pregalactic Structure Formation with Radiative Feedback". In: *The Astrophysical Journal* 548.2, pp. 509–521. DOI: 10.1086/319014. arXiv: astro-ph/0007198 [astro-ph].

Machida, Masahiro N. and Kentaro Doi (Nov. 2013). "The formation of Population III stars in gas accretion stage: effects of magnetic fields". In: *Monthly Notices of the Royal Astronomical Society* 435.4, pp. 3283–3305. DOI: 10.1093/mnras/stt1524. arXiv: 1308.2754 [astro-ph.GA].

Mebane, Richard H., Jordan Mirocha, and Steven R. Furlanetto (Oct. 2018). "The Persistence of Population III Star Formation". In: *Monthly Notices of the Royal Astronomical Society* 479.4, pp. 4544–4559. DOI: 10.1093/mnras/sty1833. arXiv: 1710.02528 [astro-ph.GA].

Mesinger, A., A. Ferrara, and D. S. Spiegel (May 2013). "Signatures of X-rays in the early Universe". In: *Monthly Notices of the Royal Astronomical Society* 431, pp. 621–637. DOI: 10.1093/mnras/stt198. arXiv: 1210.7319.

Mesinger, Andrei, Steven Furlanetto, and Renyue Cen (Feb. 2011). "21CMFAST: a fast, seminumerical simulation of the high-redshift 21-cm signal". In: *Monthly Notices of the Royal Astronomical Society* 411.2, pp. 955–972. DOI: 10.1111/j.1365-2966.2010.17731.x. arXiv: 1003.3878 [astro-ph.CO].

Moore, Ben et al. (Oct. 1999). "Dark Matter Substructure within Galactic Halos". In: *The Astrophysical Journal* 524.1, pp. L19–L22. DOI: 10.1086/312287. arXiv: astro-ph/9907411 [astro-ph].

Navarro, J. F., C. S. Frenk, and S. D. M. White (July 1995). "The assembly of galaxies in a hierarchically clustering universe". In: *Monthly Notices of the Royal Astronomical Society* 275, pp. 56–66. DOI: 10.1093/mnras/275.1.56. eprint: astro-ph/9408067.

— (May 1996). "The Structure of Cold Dark Matter Halos". In: *Astrophysical Journal* 462, p. 563. DOI: 10.1086/177173. eprint: astro-ph/9508025.

— (Dec. 1997). "A Universal Density Profile from Hierarchical Clustering". In: *Astrophysical Journal* 490, pp. 493–508. DOI: 10.1086/304888. eprint: astro-ph/9611107.

Nishi, R. and H. Susa (Oct. 1999). "Formation and Disruption of Cosmological Low-Mass Objects". In: *The Astrophysical Journal Letters* 523, pp. L103–L107. DOI: 10.1086/312277. eprint: astro-ph/9908225.

Omukai, K. and R. Nishi (Nov. 1998). "Formation of Primordial Protostars". In: *Astrophysical Journal* 508, pp. 141–150. DOI: 10.1086/306395. eprint: astro-ph/9811308.

O'Shea, B. W. and M. L. Norman (Jan. 2007). "Population III Star Formation in a ΛCDM Universe. I. The Effect of Formation Redshift and Environment on Protostellar Accretion Rate". In: *The Astrophysical Journal* 654, pp. 66–92. DOI: 10.1086/509250. eprint: astro-ph/0607013.

O'Shea, Brian W. and Michael L. Norman (Jan. 2008). "Population III Star Formation in a ΛCDM Universe. II. Effects of a Photodissociating Background". In: *The Astrophysical Journal* 673.1, pp. 14–33. DOI: 10.1086/524006. arXiv: 0706.4416 [astro-ph].

Parsons, Aaron et al. (Sept. 2019). "A Roadmap for Astrophysics and Cosmology with High-Redshift 21 cm Intensity Mapping". In: *Bulletin of the American Astronomical Society*. Vol. 51, p. 241. arXiv: 1907.06440 [astro-ph.IM].

Peebles, P. J. E. (1993). *Principles of Physical Cosmology*.

Pelupessy, Federico I., Tiziana Di Matteo, and Benedetta Ciardi (Aug. 2007). "How Rapidly Do Supermassive Black Hole "Seeds" Grow at Early Times?" In: *The Astrophysical Journal* 665.1, pp. 107–119. DOI: 10.1086/519235. arXiv: astro-ph/0703773 [astro-ph].

Planck Collaboration et al. (Sept. 2016). "Planck 2015 results. XIII. Cosmological parameters". In: *Astronomy and Astrophysics* 594, A13, A13. DOI: 10.1051/0004-6361/201525830. arXiv: 1502.01589.

Pritchard, J. R. and S. R. Furlanetto (Apr. 2006). "Descending from on high: Lyman-series cascades and spin-kinetic temperature coupling in the 21-cm line". In: *Monthly Notices of the Royal Astronomical Society* 367, pp. 1057–1066. DOI: 10.1111/j.1365-2966.2006.10028.x. eprint: astro-ph/0508381.

Pritchard, J. R. and A. Loeb (July 2010). "Constraining the unexplored period between the dark ages and reionization with observations of the global 21 cm signal". In: *Physical Review D* 82.2, 023006, p. 023006. DOI: 10.1103/PhysRevD.82.023006. arXiv: 1005.4057.

Qin, Yuxiang et al. (Apr. 2020a). "A tale of two sites - I. Inferring the properties of minihalo-hosted galaxies from current observations". In: *Monthly Notices of the Royal Astronomical Society* 495.1, pp. 123–140. DOI: 10.1093/mnras/staa1131. arXiv: 2003.04442 [astro-ph.CO].

Qin, Yuxiang et al. (Nov. 2020b). "A tale of two sites - II: Inferring the properties of minihalo-hosted galaxies with upcoming 21-cm interferometers". In: *Monthly Notices of the Royal Astronomical Society*. DOI: 10.1093/mnras/staa3408. arXiv: 2009.11493 [astro-ph.CO].

Schaerer, D. (Jan. 2002). "On the properties of massive Population III stars and metal-free stellar populations". In: *Astronomy and Astrophysics* 382, pp. 28–42. DOI: 10.1051/0004-6361:20011619. eprint: astro-ph/0110697.

Shapiro, Paul R. et al. (Sept. 2012). "Simulating cosmic reionization and the radiation backgrounds from the epoch of reionization". In: *American Institute of Physics Conference Series*. Ed. by Masayuki Umemura and Kazuyuki Omukai. Vol. 1480. American Institute of Physics Conference Series, pp. 248–260. DOI: 10.1063/1.4754363. arXiv: 1211.0583 [astro-ph.CO].

Shull, J. M. and M. E. van Steenberg (Nov. 1985). "X-ray secondary heating and ionization in quasar emission-line clouds". In: *Astrophysical Journal* 298, pp. 268–274. DOI: 10.1086/163605.

Silvestri, Alessandra and Mark Trodden (Sept. 2009). "Approaches to understanding cosmic acceleration". In: *Reports on Progress in Physics* 72.9, 096901, p. 096901. DOI: 10.1088/0034-4885/72/9/096901. arXiv: 0904.0024 [astro-ph.CO].

Smith, F. J. (Oct. 1966). "Hydrogen atom spin-change collisions". In: *Planetary Space Science* 14, pp. 929–936. DOI: 10.1016/0032-0633(66)90130-9.

Sobral, David et al. (Aug. 2015). "Evidence for PopIII-like Stellar Populations in the Most Luminous Lyman-α Emitters at the Epoch of Reionization: Spectroscopic Confirmation". In: *Astrophysical Journal* 808.2, 139, p. 139. DOI: 10.1088/0004-637X/808/2/139. arXiv: 1504.01734 [astro-ph.GA].

Susa, H. (Apr. 2006). "Smoothed Particle Hydrodynamics Coupled with Radiation Transfer". In: *Publications of the Astronomical Society of Japan* 58, pp. 445–460. DOI: 10.1093/pasj/58.2.445. eprint: astro-ph/0601642.

Susa, H., K. Hasegawa, and N. Tominaga (Sept. 2014). "The Mass Spectrum of the First Stars". In: *The Astrophysical Journal* 792, 32, p. 32. DOI: 10.1088/0004-637X/792/1/32. arXiv: 1407.1374.

Tanaka, Toshiyuki and Kenji Hasegawa (Nov. 2020). "Modelling Population III stars for semi-numerical simulations". In: *arXiv e-prints*, arXiv:2011.13504, arXiv:2011.13504. arXiv: 2011.13504 [astro-ph.GA].

Tanaka, Toshiyuki et al. (Oct. 2018). "Stellar mass dependence of the 21-cm signal around the first star and its impact on the global signal". In: *Monthly Notices of the Royal Astronomical Society* 480.2, pp. 1925–1937. DOI: 10.1093/mnras/sty1967. arXiv: 1805.07947 [astro-ph.GA].

Tegmark, M. et al. (Jan. 1997). "How Small Were the First Cosmological Objects?" In: *The Astrophysical Journal* 474, p. 1. DOI: 10.1086/303434. eprint: astro-ph/9603007.

Tokutani, M. et al. (May 2009). "The 21-cm signature of early relic HII regions". In: *Monthly Notices of the Royal Astronomical Society* 395, pp. 777–780. DOI: 10.1111/j.1365-2966.2009.14604.x. arXiv: 0902.1018 [astro-ph.CO].

Tominaga, N., H. Umeda, and K. Nomoto (May 2007). "Supernova Nucleosynthesis in Population III 13-50 M_{solar} Stars and Abundance Patterns of Extremely Metal-poor Stars". In: *Astrophysical Journal* 660, pp. 516–540. DOI: 10.1086/513063. eprint: astro-ph/0701381.

Umeda, H. and K. Nomoto (Jan. 2002). "Nucleosynthesis of Zinc and Iron Peak Elements in Population III Type II Supernovae: Comparison with Abundances of Very Metal Poor Halo Stars". In: *Astrophysical Journal* 565, pp. 385–404. DOI: 10.1086/323946. eprint: astro-ph/0103241.

Venemans, B. P. et al. (Dec. 2013). "Discovery of Three z > 6.5 Quasars in the VISTA Kilo-Degree Infrared Galaxy (VIKING) Survey". In: *The Astrophysical Journal* 779, 24, p. 24. DOI: 10.1088/0004-637X/779/1/24. arXiv: 1311.3666.

Visbal, Eli, Greg L. Bryan, and Zoltán Haiman (July 2020). "Self-consistent Semianalytic Modeling of Feedback during Primordial Star Formation and Reionization". In: *The Astrophysical Journal* 897.1, 95, p. 95. DOI: 10.3847/1538-4357/ab994e. arXiv: 2001.11118 [astro-ph.GA].

Visbal, Eli, Zoltán Haiman, and Greg L. Bryan (Apr. 2018). "Self-consistent semi-analytic models of the first stars". In: *Monthly Notices of the Royal Astronomical Society* 475.4, pp. 5246–5256. DOI: 10.1093/mnras/sty142. arXiv: 1705.09005 [astro-ph.GA].

Visbal, Eli et al. (Nov. 2014). "High-redshift star formation in a time-dependent Lyman-Werner background". In: *Monthly Notices of the Royal Astronomical Society* 445.1, pp. 107–114. DOI: 10.1093/mnras/stu1710. arXiv: 1402.0882 [astro-ph.CO].

Wise, J. H. et al. (Jan. 2012). "The Birth of a Galaxy: Primordial Metal Enrichment and Stellar Populations". In: *The Astrophysical Journal* 745, 50, p. 50. DOI: 10.1088/0004-637X/745/1/50. arXiv: 1011.2632.

Wise, John H. and Tom Abel (Dec. 2007). "Suppression of H_2 Cooling in the Ultraviolet Background". In: *The Astrophysical Journal* 671.2, pp. 1559–1567. DOI: 10.1086/522876. arXiv: 0707.2059 [astro-ph].

Wouthuysen, S. A. (1952). "On the excitation mechanism of the 21-cm (radio-frequency) interstellar hydrogen emission line." In: *Astrophysical Journal* 57, pp. 31–32. DOI: 10.1086/106661.

Wu, X.-B. et al. (Feb. 2015). "An ultraluminous quasar with a twelve-billion-solar-mass black hole at redshift 6.30". In: *nature* 518, pp. 512–515. DOI: 10.1038/nature14241. arXiv: 1502.07418.

Yajima, H. and S. Khochfar (Mar. 2015). "Can the 21-cm signal probe Population III and II star formation?" In: *Monthly Notices of the Royal Astronomical Society* 448, pp. 654–665. DOI: 10.1093/mnras/stu2687. arXiv: 1405.7385.

Yajima, H. and Y. Li (Dec. 2014). "Distinctive 21-cm structures of the first stars, galaxies and quasars". In: *Monthly Notices of the Royal Astronomical Society* 445, pp. 3674–3684. DOI: 10.1093/mnras/stu1982. arXiv: 1308.0381.

Yajima, Hidenobu, Jun-Hwan Choi, and Kentaro Nagamine (Mar. 2011). "Escape fraction of ionizing photons from high-redshift galaxies in cosmological SPH simulations". In: *Monthly Notices of the Royal Astronomical Society* 412.1, pp. 411–422. DOI: 10.1111/j.1365-2966.2010.17920.x. arXiv: 1002.3346 [astro-ph.CO].

Yoshida, N., K. Omukai, and L. Hernquist (Aug. 2008). "Protostar Formation in the Early Universe". In: *Science* 321, p. 669. DOI: 10.1126/science.1160259. arXiv: 0807.4928.

Yoshida, N. et al. (Aug. 2003). "Simulations of Early Structure Formation: Primordial Gas Clouds". In: *Astrophysical Journal* 592, pp. 645–663. DOI: 10.1086/375810. eprint: astro-ph/0301645.

Yoshida, N. et al. (Nov. 2006). "Formation of Primordial Stars in a ΛCDM Universe". In: *Astrophysical Journal* 652, pp. 6–25. DOI: 10.1086/507978. eprint: astro-ph/0606106.

Yoshiura, S. et al. (Nov. 2017). "Constraining the contribution of galaxies and active galactic nuclei to cosmic reionization". In: *Monthly Notices of the Royal Astronomical Society* 471, pp. 3713–3726. DOI: 10.1093/mnras/stx1754. arXiv: 1602.04407.

Zel'Dovich, Y. B. (Mar. 1970). "Reprint of 1970A&A.....5...84Z. Gravitational instability: an approximate theory for large density perturbations." In: *Astronomy and Astrophysics* 500, pp. 13–18.